UNIVERSITY OF CALIFORNIA
SANTA CRUZ

PHYSICAL OCEANOGRAPHIC AND ACOUSTIC OBSERVATIONS OF THE BEAUFORT SEA AND ITS SUBSURFACE DUCT SENSITIVITY TO DETERMINISTIC OCEAN FEATURES.

A dissertation submitted in partial satisfaction of the
requirements for the degree of

DOCTOR OF PHILOSOPHY

in

OCEAN SCIENCES

by

Murat Kucukosmanoglu

September 2022

The Dissertation of Murat Kucukosmanoglu is approved:

Dr. Christopher A. Edwards, Chair

Dr. John A. Colosi

Dr. Andrew M. Moore

Dr. Matthew A. Dzieciuch

Peter F. Biehl
Vice Provost and Dean of Graduate Studies

Table of Contents

List of Figures

List of Tables

Abstract

Physical Oceanographic and Acoustic Observations of the Beaufort sea and its subsurface duct sensitivity to deterministic ocean features.

by

Murat Kucukosmanoglu

The Arctic Ocean is rapidly transforming due to climate change, and this thesis analyzes two, year-long ocean-acoustic data sets to quantify variability in the thermohaline, current and ice structure and examine the implications for acoustic propagation in the Beaufort Sea. The two field efforts are the Canada Basin Acoustic Propagation Experiment (CANAPE) and the Coordinated Arctic Acoustic Thermometry Experiment (CAATEX). These results are important since acoustics offers a unique tool for the Arctic under ice communication, navigation, and remote sensing.

A key acoustic feature of the Beaufort Sea is the Beaufort duct created by the Pacific winter water (PWW), which is sandwiched between the shallow Pacific summer water (PSW) and the deeper Atlantic water (AW). This is important because this duct allows for long-range transmission without lossy interactions with sea ice or surface waves. In general, we find this duct can trap from 2-6 acoustic modes in the frequency range between several tens of Hz and several hundreds of Hz. Since fluctuations can alter the number of trapped modes and affect Transmission loss, we have analyzed variability due to spice, internal waves, eddies, and near-inertial waves, and we find spicy thermohaline structure is observed to be the most significant source of variability in the top 100 m, followed by eddies and internal waves.

Acoustic interaction with the ice cover is another critical factor affecting arctic acoustics, so we have analyzed high-frequency acoustic scattering statistics from

the CANAPE. Five important surface scattering epochs were identified over the seasonal cycle: open water, initial ice formation, ice solidification, ice thickening, and ice melting. The most significant changes in statistics are seen during the formation, solidification, and melting. The statistical features are comparable throughout the CANAPE region, implying similar ice properties.

The stability of acoustic propagation in the Beaufort duct is another aspect of this thesis. We analyzed the oceanographic measurements from the CANAPE and CAATEX, and focused on the problem of mode coupling in the Beaufort duct, induced by deterministic ocean features such as eddies and intrusions. Here we find that deterministic variability in the PSW due to spice and stronger halocline eddies can result in enhanced coupling between acoustic modes in and out of the BD. Here we use the mode interaction parameter (MIP), which is a non-dimensional quantity, Γ_{mn} that quantifies the mode coupling strength between mode m (a duct mode) and all the other n modes. Strong/moderate-weak coupling is determined by MIP greater-than/less-than 1. The MIP is a function of acoustic frequency and horizontal structure, which we define as the typical half-width of Gaussian perturbation (Δ) in this thesis. Our result showed that for both large and small Δ, Γ_{mn} goes to zero, and maximal coupling occurs when Δ ranges between 1.5 and 2.2 km.

Acknowledgments

First and foremost, I want to express my sincere thanks to John A. Colosi, my PhD advisor, for his unwavering support and guidance during my experience in his lab and for turning me into the scientist I am today. Thanks also to Christopher A. Edwards, Andrew M. Moore, and Matthew A. Dzieciuch, members of my dissertation reading committee, for taking the time to provide critical critique and suggestions. In particular, I would like to thank Edward L. Richards, who has been an outstanding labmate for the past two years. In addition, I'd like to express my gratitude to the members of the CANAPE and CAATEX experimental groups, whose contributions were critical to the completion of this thesis. Finally, I'd like to express my gratitude to my wife Nihan and my daughter Sibel for their patience and support during this journey, and to the members of my vast family, whom I hope to see in person again as soon as possible.

The text of this dissertation includes reprint of the following previously published material in Chapter 2:

Kucukosmanoglu, M., Colosi, J. A., Worcester, P. F., Dzieciuch, M. A., and Torres, D. J. (2021). Observations of soundspeed fluctuations in the beaufort sea from summer 2016 to summer 2017. The Journal of the Acoustical Society of America, 149(3):1536–1548.

The co-author listed in this publication, John A. Colosi, directed and supervised the research which forms the basis for the dissertation. Peter F. Worcester, Matthew A. Dzieciuch and Daniel Torres are also contributing co-authors, but the analysis and writing of this paper were substantially my own.

The text of this dissertation includes reprint of the following previously published material in Chapter 3:

Kucukosmanoglu, M., Colosi, J. A., Worcester, P. F., Dzieciuch, M. A., Olson,

D. R., Richards, E. L., and Miller, C. W. (2022). Beaufort sea observations of 11 to 12.5 khz surface pulse reflections near 50 degree grazing angle from summer 2016 to summer 2017. The Journal of the Acoustical Society of America, 151(1):106–125.

The co-author listed in this publication, John A. Colosi, directed and supervised the research which forms the basis for the dissertation. Peter F. Worcester, Matthew A. Dzieciuch, Derek R. Olson, Edward L. Richards and Christopher W. Miller are also contributing co-authors, but the analysis and writing of this paper were substantially my own.

Chapter 1

Introduction

The Beaufort Sea is a critical area for naval tactical studies, oil and gas exploration, and physical oceanography considering its historical significance and geographical location. The Beaufort Sea is rapidly transforming due to climate change, which has resulted in significant ice loss thus, allowing late summer/early fall commercial maritime traffic to cross the Arctic Ocean [Stephenson et al., 2018]. The decreasing sea ice not only facilitates trans-Arctic shipping but also provides for commercial exploration of oil and gas deposits. According to the Circum-Arctic Resource Appraisal (CARA), the Arctic Ocean contains at least 10% of the world's oil and gas resources [Bird et al., 2008]. The changing sea ice conditions additionally feedback on the global climate, since ice regulates the exchanges of heat, momentum, and moisture between the atmosphere and the polar oceans [Stroeve and Notz, 2018]. There is also a significant influence on the thermohaline structure [Perovich et al., 2021] and energy budget in the upper layer [Hudson et al., 2013].

Recent Arctic observations also show that there are significant thermohaline changes taking place in the Arctic water column. The relatively cool and fresh Pacific Waters and the warm, salty Atlantic water masses also con-

tribute to changes in the Arctic's thermohaline structure [Worcester et al., 2018, Worcester et al., 2020, Kucukosmanoglu et al., 2021]. The Pacific Waters enter the Arctic Ocean through the Bering Strait and flows along Alaska and Canada's northern coasts. They are modified through air-sea interaction as they cross the shallow Chukchi Sea before entering the deep ocean, resulting in two distinct Pacific water masses in the halocline of the Canada Basin [Timmermans et al., 2014]. The upper halocline of the Canada Basin contains these waters masses: The warm Pacific summer water (PSW) on the top between approximately 70 and 120 m deep, and the cold Pacific winter water (PWW) at the bottom, roughly between 120 and 250 m [Kucukosmanoglu et al., 2021]. Together, they form a highly stratified upper ocean, with strong density gradients that shield the underlying warm Atlantic water (AW) from sea ice [Spall et al., 2018].

In Chapter 2 of this thesis, moored data and ship CTD observations from the Canada Basin Acoustic Propagation Experiment (CANAPE) are used to analyze the thermohaline and current characteristics in the Beaufort Sea. Strong upper halocline eddies have been found in earlier studies in the Western Arctic Ocean [Brannigan et al., 2017], which can weaken the stability of the highly stratified halocline, disturb the thermohaline structure, and produce sound-speed variations [DiMaggio et al., 2018]. One of the major sources of sound speed fluctuations is vertical displacements due to internal waves and eddies. The majority of the energy in the internal wave field resides in the near-inertial frequency band, at frequencies between 1.0 and 1.1 f, where f is Coriolis frequency. The internal wave band spectrum does not follow the conventional Garrett-Munk (GM) spectrum, and the total energy level is just 4% of the GM level. Energy decreases below the inertial frequency. Eddy activity causes the energy to increase again at lower frequencies. Surprisingly, the internal wave band has a moderate peak at twice

the tidal inertial frequency.

Significant sound-speed fluctuations in the Beaufort Sea have also been seen due to temperature/salinity variability along isopycnals (spice) [DiMaggio et al., 2018]. The spice causes sound speed changes of several meters per second in the upper 100 meters, where warm and salty PSW and cold and less saline Arctic surface water interact (ASW). The temperature and salinity structure generates two sound channels, the surface duct and the Beaufort duct (BD), both of which are important for this thesis. The surface duct is formed by the strong halocline, resulting in a minimal sound speed at the surface. The PWW, which is wedged between the warmer PSW and AW in the Western Arctic Ocean, forms the BD. Sound energy trapped in the BD can travel long distances with reduced transmission loss since it does not contact the lossy sea ice. Previous research has found that changing Arctic circumstances are reinforcing this duct because the PSW is thickening and warming, and the depth of the PWW has increased from 150 to 200 meters since 2000 [Worcester et al., 2020, Timmermans et al., 2014].

Chapter 3 investigates high-frequency acoustic scattering statistics off the Arctic sea surface over an annual cycle measured by the navigation systems of seven acoustic sources and/or receiver moorings in the Beaufort Sea from summer 2016 to summer 2017. Sea ice is a critical component that affects acoustic propagation from its rough surface, elastic and acoustic properties, that is acoustically distinct from the open ocean air/sea interaction [Hope et al., 2017]. The Beaufort Sea ice has become much younger and thinner in the last two decades, resulting in significant changes in its various physical properties such as porosity, brine content, roughness, shear modulus [Worcester et al., 2020, Kovacs, 1996] and morphological differences among the various types of ice [Wadhams and Doble, 2008]. Acous-

tic scatter from the sea surface enables us to quantify sea ice scattering statistics such as moments of reflected intensity, its probability density function (PDF), and pulse time spread. Five scattering epochs are identified using these statistics. They are open water, initial ice formation, ice solidification, ice thickening, and ice melting. Here an elastic layer reflection coefficient (ELRC) model is used to qualitatively describe the processes that control reflection coefficient variations.

Lastly, Chapter 4 investigates the strength of coupling between BD modes and other more lossy modes using a non-dimensional mode interaction parameter (MIP) matrix Γ_{mn} [Colosi and Zinicola-Lapin, 2021], which has been used successfully to describe mode coupling in mixed layer ducts in previous studies [Colosi, 2008, Colosi and Zinicola-Lapin, 2021, Yang, 2014]. The MIP is a function of acoustic frequency and a given perturbation field's vertical and horizontal scales. Therefore, we analyze the water masses of PSW, PWW, and AW that comprise the BD [Kucukosmanoglu et al., 2021] using the yearlong time series of moored temperature and salinity observations from the 2016-2017 CANAPE and the 2019-2020 CAATEX to define the perturbation field induced by deterministic ocean features such as eddies and spicy intrusions. These observations show the strongest variability in the PSW, the weakest in the PWW, and moderate in the AW. Notably, there is a frequency dependent resonance condition that leads strong fluctuations in the acoustic intensity if the beat wave number overlaps the horizontal scales of sound speed variability. Maximum variabilities in the first BD mode energy are estimated to occur when Δ ranges between 1.5 and 2.2 km.

Chapter 2

Observations of sound-speed fluctuations in the Beaufort Sea from summer 2016 to summer 2017.

Abstract

Due to seasonal ice cover, acoustics provides a unique means for Arctic undersea communication, navigation, and remote sensing. This study seeks to quantify the annual cycle of thermohaline structure in the Beaufort Sea and characterize acoustically relevant oceanographic processes, such as eddies, internal waves, near-inertial waves (NIWs), and spice. The observations are from a seven-mooring, 150-km radius acoustic transceiver array equipped with oceanographic sensors that collected data in the Beaufort Sea 2016 to 2017. Depth and time variations of sound-speed are analyzed using isopycnal displacements, allowing a separation of baroclinic processes and spice. Compared to lower latitudes, the overall sound-speed variability is small, with a maximum rms of 0.6 m/s. The largest source of variability is spice, followed by eddies and internal waves, and are most significant in the upper 100 m. The displacement spectrum in the internal-wave band is time dependent and different from the Garret-Munk (GM) spectrum. Internal-wave energy varied with time averaging 5% of GM. The spice sound-speed frequency spectrum has a form very different from the displacement spectrum, a result not seen at lower latitudes. Because sound-speed variations are weak, observations of episodic energetic NIWs with horizontal currents up to 20 cm/s have potential acoustical consequences.

2.1 Introduction

The Arctic Ocean is of considerable interest in the context of its changing processes such as currents, thermohaline structure, and sea ice extent. Sea ice in the Arctic Ocean has dramatically declined in recent decades [Stroeve et al., 2012, Maslanik et al., 2007], with more notable decreases in September than in winter text [Stroeve et al., 2014]. Significant variations in temperature [DiMaggio et al., 2018] and freshwater content [Haine et al., 2015] have also been observed. Using observations from the 2016-2017 Canada Basin Acoustic Propagation Experiment (CANAPE), this paper seeks to quantify the effects of these changes and important ocean processes such as eddies, internal waves, internal tides, and temperature/salinity variability along isopycnals (spice) on Arctic sound speed and current structure.

Mesoscale eddies induce large changes in sound speed at lower latitudes [Worcester et al., 1999]. This is the case in the CANAPE observations to the extent that sub-inertial sound speed fluctuations dominate the variability. Beaufort Sea eddies are mostly anticyclonic, and can cover up to one-quarter of the ocean surface area [Carpenter and Timmermans, 2012, Zhao et al., 2014]. Most eddies exist in the upper ocean halocline and are observed to be strong below the mixed layer [Brannigan et al., 2017]. Because eddies are often generated in frontal regions, core and surrounding water masses differ. To the extent there are instabilities, spicy water is formed from the co-mingling of the water masses giving rise to sound speed perturbations [Fine et al., 2018]. This is in addition to the sound speed changes due to the doming of isopycnals caused by the circulation of the eddy. The CANAPE observations are interesting in that the sub-inertial variations in sound speed are dominated by spice rather than displacement effects.

Internal tides can also produce large shallow and deep water sound

speed anomalies important to sound propagation [Colosi et al., 2013, Colosi et al., 2012]. Internal tides are generated by barotropic tidal flows interacting with topography [Munk and Wunsch, 1998, Garrett and Kunze, 2007]. They can be a source for the broadband internal wave field through spectral energy transfer by nonlinear wave-wave interaction [Bell Jr, 1975, Levine et al., 1987]. Internal tides are relatively weak in many regions of the Arctic Ocean compared to other oceans [Lyard, 1997]. In addition, they mainly do not exist at latitudes higher than 75.05^{o}N at the M2 frequency [Levine et al., 1987]. In this work, the moorings were close to the M2 critical latitude making internal tides indistinguishable from near inertial waves. There is a moderate peak in the displacement spectrum at twice the tidal frequency, however this peak might be related to nonlinear internal tide generation processes. The acoustical consequences of this peak are unknown.

The broadband field of stochastic internal waves has been studied for decades in relation to sound propagation [Colosi, 2016, Flatté et al., 1979]. Internal wave energy levels in the Arctic are quite low, although recent studies have found that the internal wave energy level has risen because of increased momentum fluxes from the atmosphere as a consequence of the rapid decline in the sea ice extent in the Canada Basin [Rainville et al., 2011, Dosser and Rainville, 2016]. The CANAPE observations show a weak internal wave field with energies roughly 5% of the Garrett-Munk reference energy [Munk, 1981]. Additionally, previous studies have found the Arctic internal wave energy level and spectral shape to be quite variable in time [Levine et al., 1987]. The CANAPE observations reinforce this notion of a non-stationary internal wave spectrum in which the spectral energy varies by a factor of 3 and the spectral shape changes markedly from slopes of -1.1 to -0.5.

A relatively new topic to sound propagation in the ocean is that of sound speed anomalies along isopycnals generated by compensating temperature and salinity structure or spice [Dzieciuch et al., 2004, Colosi et al., 2013, DiMaggio et al., 2018]. The Arctic Ocean differs from ice-free oceans because the temperature near the freezing point has a minor effect on the density [Timmermans and Jayne, 2016]. Therefore, a small salinity anomaly requires a large temperature anomaly to be density compensated, thereby giving rise to a large sound speed anomaly. In the CANAPE observations, spice generally is observed between the Arctic Surface Water (ASW) and the Pacific Summer Water (PSW), where there is mixing between the warm and salty PSW and cold and less saline ASW. Changes in T and S between these water masses results in sound speed variations up to several m/s in the upper 100 m. Additionally, like the internal wave spectrum, the spice sound speed spectrum (energy and spectral shape) is found to be quite variable in time.

Near-inertial waves (NIWs) induce fluctuations in horizontal current by driving water parcels mostly in horizontal circles with relatively weaker vertical motion [Colosi, 2016]. NIWs can originate from sea ice motion and winds at the surface in the Arctic Ocean [D'Asaro, 1985, Rigby, 1976, Dosser and Rainville, 2016] and typically generate currents of order tens of cm per second. These waves are of interest to Arctic acoustics because sound speed fluctuations due to eddies and internal wave displacements are also of order several tens of cm per second. Previous studies have found the energy of NIWs to be one to two orders of magnitude weaker under the ice cover than other oceans [Levine et al., 1987, Morison et al., 1985, Halle and Pinkel, 2003]. NIW energy in the Arctic is significantly higher in summer when the sea ice is absent [Dosser et al., 2014, McPhee, 2008, Rainville and Woodgate, 2009] despite weaker

winds than in winter [Overland, 2009]. A possible explanation is that thicker ice in winter, particularly for concentrations above 90%, may lead to a significant decrease in momentum transfer from the wind to the water column [Martini et al., 2014]. The CANAPE observations generally support these views, but episodic NIW events were observed under the ice that are larger than most of the open water NIWs.

The organization of the paper is as follows. Section II discusses the CANAPE observations of Temperature (T), Salinity (S), and current and the methods of analysis. Frequency spectra of isopycnal displacements and spicy sound speed anomalies are described in Section III, together with the varying energy level as a function of depth. In Section IV, NIWs were analyzed to describe the spatial and temporal variability throughout the annual cycle. The paper ends with the final summary and conclusions.

2.2 Experiment

The CANAPE experiment aims to assess the present ocean acoustic conditions in the Beaufort Sea with a focus on physical oceanographic processes that impact sound propagation on varying space and time scales up to the annual cycle. This effort was carried out between 26 August 2016 and 02 October 2017 utilizing six acoustic transceiver moorings and one Distributed Vertical Line Array (DVLA) receiver mooring, each equipped with various oceanographic sensors such as Temperature, Conductivity, Depth (CTD), Temperature alone, Acoustic Doppler Current Profilers (ADCP), and Ice Profiling Sonars (IPS). In this work, the time-coordinate is identified in yeardays beginning with 01 January 2016, 1200 UTC as yearday 1.5. Fig. 2.1 shows the overall experimental geometry and bathymetry, and it should be noted that array straddles the latitude where the

Coriolis frequency matches the M2 tidal frequency and important consideration with regards to inertial waves and internal tides. Table I gives the locations and water depths for all 7 moorings.

Table 2.1: CANAPE Mooring locations and water depths

Mooring	Latitude (N)	Longitude (W)	Water Depth (m)	Range to DVLA (km)
T1	75.3633 °	145.0522 °	3780	176.335
T2	73.7870 °	144.8043 °	3711	207.299
T3	73.1807 °	149.9738 °	3771	176.338
T4	74.3018 °	153.9499 °	3860	108.980
T5	75.7177 °	151.1767 °	3842	108.977
T6	74.5027 °	149.0122 °	3816	57.299
DVLA	74.7476 °	150.6729°	3845	0

2.2.1 CANAPE Observations

Here the oceanographic instrumentation on the seven CANAPE moorings used in this study are described. The DVLA was the main source of data quantifying the variable thermohaline structure because it was equipped with a dense array of CTD instruments. Full water depth shipboard CTDs were also taken at each mooring during the deployment and recovery cruises. The DVLA CTD sensors provided the detailed salinity and temperature data required for separating internal waves and spice [Colosi et al., 2013, Colosi et al., 2012]. This included 28 Seabird MicroCats (SBE 37-SMP/SM) sampling every 5 minutes and spanning 50-425 m depths with typical separation of 13.5 m. The DVLA also had an upward-looking 75 kHz Teledyne RDI ADCP at 613-m depth with a sample interval of 3 hours and a range of approximately 300-400 m, and a downward-looking 150-kHz Teledyne RDI ADCP at 625-m depth with a sample interval of 30 min. and with a range of approximately 100-200 m.

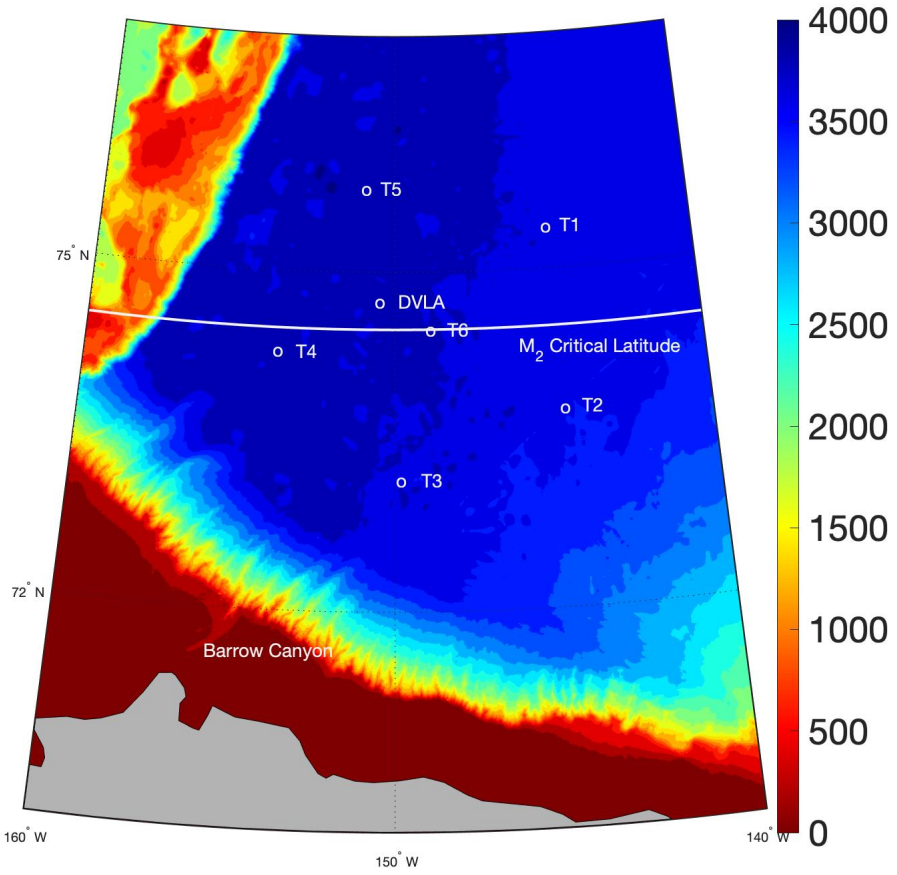

Figure 2.1: Mooring geometry for CANAPE 2016, consisting of six acoustic transceivers (T1, T2, ... T6) and a DVLA receiver located at the intersection of the T1-T4 and T3-T5 paths. Topography is from Sandwell/Smith [Smith and Sandwell, 1997, Becker et al., 2009, Smith and Sandwell, 2019].

Both ADCPs had an 8-m bin size. The DVLA oceanographic instrumentation is listed in Table II. The DVLA and T1-T6 hydrophone modules (HMs) recorded temperature, respectively at 20-minute and 12-minute intervals, and there were ten temperature sensors on each of the T-moorings that recorded at 10-second (SBE 56) and 5-second (RBRsolo T) intervals. These temperature data were not used in the present analysis because there was no accompanying salinity data. Table III shows the oceanographic instrumentation on a "typical" T mooring. Additionally, on the subsurface floats of the T1-T6 moorings, there were upward-looking 600 kHz Teledyne RDI ADCPs used to quantify NIW variability and 420 kHz IPS to give ice thickness. All the moorings were moving with the currents [Colosi et al., 2018], but were acoustically navigated by a long baseline system with 3 to 4 bottom transponders. This navigation is required to use the observed acoustic travel times for tomography and ocean model data assimilation. The navigation data reveals that the DVLA watch circle radius, primarily driven by tides and NIWs was typically 50 to 100 m with vertical excursions of a few tens of meters. More dramatic mooring motion is seen when an eddy is present. These events lead to horizontal deflections of several hundreds of meters and vertical displacements ranging from roughly 50 to 100 meters.

Table 2.2: CANAPE DVLA mooring oceanographic instrumentation placement with average depth. The Hydrophone Module depths are not shown.

depth (m)	Instrument	Time Duration	depth (m)	Instrument	Time Duration
51.4	SBE 37-SMP[1]	11 Sep-1 Oct	254.4	SBE 37-SMP	11 Sep-8 Jul
64.9	SBE 37-SMP	11 Sep-1 Oct	267.1	SBE 37-SMP	11 Sep-11Jul
78.4	SBE 37-SMP	11 Sep-1 Oct	280.8	SBE 37-SMP	11 Sep-1 Oct
92.0	SBE 37-SMP	11 Sep-1 Oct	294.4	SBE 37-SMP	11 Sep-1 Oct
105.5	SBE 37-SMP	11 Sep-1 Oct	308.1	SBE 37-SMP	11 Sep-1 Oct
118.6	SBE 37-SMP	11 Sep-1 Oct	329.8	SBE 37-SMP	11 Sep-1 Oct
132.1	SBE 37-SMP	11 Sep-1 Oct	343.4	SBE 37-SMP	11 Sep-1 Oct
145.5	SBE 37-SMP	11 Sep-1 Oct	357.0	SBE 37-SMP	11 Sep-1 Oct
159.5	SBE 37-SMP	11 Sep-22 June	370.4	SBE 37-SMP	11 Sep-1 Oct
172.6	SBE 37-SMP	11 Sep-25 May	384.2	SBE 37-SMP	11 Sep-1 Oct
186.1	SBE 37-SMP	11 Sep-13 Jun	399.2	SBE 37-SMP	11 Sep-1 Oct
199.4	SBE 37-SMP	11 Sep-10 Jul	410.2	SBE 37-SM[1]	11 Sep-1 Oct
212.9	SBE 37-SMP	11 Sep-17 Aug	423.7	SBE 37-SM	11 Sep-1 Oct
226.4	SBE 37-SMP	11 Sep-14 Jun	613.0	75 kHz ADCP [2]	9 Oct-1 Oct
240.0	SBE 37-SMP	11 Sep-1 Oct	625.0	150 kHz ADCP [2]	11 Sep-1 Oct

Table 2.3: CANAPE T mooring oceanographic instrumentation placement with average depth.

depth (m)	Instrument	depth (m)	Instrument
40	IPS-5/600 kHz ADCP[1]	158	HM
44	SBE 37-SMP	167	HM
50	HM	176	HM
59	HM	180	T-Sensor[2]
68	HM	200	T-Sensor
77	HM	225	T-Sensor
86	HM	250	T-Sensor
95	HM	280	T-Sensor
104	HM	325	T-Sensor
113	HM	375	T-Sensor
122	HM	430	T-Sensor
131	HM	490	T-Sensor
140	HM	570	T-Sensor
149	HM	3763	BPR[3]

2.2.2 Thermohaline Observations

Mean profiles of temperature, salinity, sound speed, buoyancy frequency, potential density, and potential sound speed gradient obtained from shipboard and the DVLA moored CTD data between 16 September 2016 and 13 June 2017 are displayed in Fig. 2.2. Four distinct water masses can be identified. Starting from the top of the water column, ASW is cold and fresh, PSW is warmer and saltier than ASW, Pacific Winter Water (PWW) is colder and saltier than PSW, and lastly Atlantic Water (AW) is warm and salty. In Fig. 2.2, the ASW from the CTD show high temperatures near the surface due to summer solar heating.

The two temperature maxima at 86 m and 495 m are associated with PSW and AW, respectively, and the temperature minimum at 215 m depth is associated with PWW.

Two haloclines are present, a strong one in the ASW and a weaker one between the PWW and the AW. The ASW halocline gives rise to strong density stratification leading to buoyancy frequencies up to 10 cycles per hour (cph). The effect of the deeper halocline is also seen with an increase in buoyancy frequency.

To illustrate the CTD observations, depth-time series of temperature, salinity and sound speed anomalies are displayed in Fig. 2.3 (left), showing the variability observed in the upper 200 m during the passage of an eddy. The eddy is characterized by cold-fresh waters roughly between yearday 285 and 300, and warm-salty waters roughly between yearday 300 and 315. Sound speed change abruptly across this transition, but the isopycnals deviate only slightly. There is also a great deal of sound speed structure in the upper 100 m that is attributable to spice. Anomalies below 200 m did not change significantly over the year, showing that the dominant sound speed variability is in the upper 100 m. The yearlong CANAPE thermohaline structure and variability are nicely summarized in a T-S

diagram (Fig. 2.3 right) computed using the DVLA moored CTD data between 16 September 2016 and 13 June 2017. The isopycnal contours are nearly vertical because near the freezing point, density is strongly driven by salinity rather than temperature. The four different water masses previously discussed are indicated on the T/S diagram. Because of its low salinity, ASW shows up on the left hand side of the diagram. The subsurface temperature maximum identifies PSW, while the subsurface temperature minimum identifies PWW. AW is seen to be warm and salty. But, most intriguing in the T/S diagram are the changes in variability from layer to layer. AW is the least variable with the points forming a thin line. ASW and PSW are the most variable with clouds of points occupying large regions of θ-S space. Points scattered along a density contour represent spice, that is temperature and salinity variations but constant density [Dzieciuch et al., 2004]. These spicy variations are acoustically significant since compensating temperature and salinity anomalies (hot and salty/cold and fresh) reinforce in sound speed [Colosi, 2016].

Most importantly for this acoustical work is that the thermohaline structure gives rise to two sound channels called the surface duct and the Beaufort Duct. The surface duct is formed mostly from the strong halocline leading to a sound speed minimum at the surface in winter, but in Fig. 2.2 the effect of the warm summer surface layer is evident. The Beaufort Duct is formed by the cold PWW between the warmer PSW and AW. Additionally, the Beaufort Duct potential sound speed gradient is close to zero, implying that sound speed fluctuations induced by vertical displacements (such as internal waves) will be small. Unlike the surface duct, the Beaufort Duct trapped sound is of sufficiently high frequency and is expected to have low losses since it is shielded from lossy surface interactions. This sound channel can be crudely characterized as having a minimum (or axial)

sound speed c_a at depth z_a and a maximum sound speed, c_m, above and below the axis at depths z^+ and z^-. The modal cutoff f_c frequency (Hz) for this general duct is approximately

$$f_c = \left(\frac{c_a^3}{\delta c}\right)^{1/2} \frac{1}{\delta z} \frac{3}{4\sqrt{2}}(n - 1/2), \tag{2.1}$$

where $\delta c = c_m - c_a$, $\delta z = |z^+ - z^-|$, and n is mode number (see the Appendix for details). Some of the parameters of this equation are plotted in Fig. 2.4. For the mean and standard deviations of the Beaufort Duct parameters derived from Fig. 2.4, it is found that δz is 144 ± 10 m, δc is 2.2 ± 0.4 m/s, and c_a is 1442 ± 0.1 m/s . Axial sound speed is found to be quite stable in time except for roughly 1 m/s change around yearday 270. Another noteworthy point of this display is that the upper and lower boundaries of the Beaufort Duct varied significantly between yearday 285 and 315, when the eddy with changing temperature and salinity is observed in Fig. 2.3. This eddy leads to significant changes in modal cutoff frequencies by a factor of 2.

The Beaufort Duct cutoff frequencies for modes 1 to 4 are 69 ± 12 , 208 ± 36 , 346 ± 60, and 484 ± 83 Hz respectively. Mode 1 shows trapping at 100 Hz and higher frequencies, but at 50 Hz the mode has spread out significantly (Fig. 2.5). Similar cases apply to other modes below their f_c. Importantly for this experiment with acoustic frequencies between 200 and 300 Hz, it is expected that modes 1 and 2 to be strongly trapped, mode 3 is marginally trapped, and modes 4 and above are not trapped.

2.2.3 Currents

The DVLA and T-mooring ADCP observations reveal energetic but isolated eddies and episodic strong NIWs (Fig. 2.6).

At the DVLA, a strong deep eddy is seen between 2016 yeardays 620 and 640, while the lower edges of shallower eddies are seen between yeardays 590 and 620. These eddies are not seen simultaneously on the T6 ADCP because it is 57 km away, and typical eddy radii in this region are 4-16 km [Zhao et al., 2014]. Also on the DVLA, downward propagation of NIWs packets is seen between yeardays 600 and 620. For the T-6 mooring, energetic upper ocean NIWs exist between yeardays 580 and 640. They are seen to be more energetic after yearday 635. It will be shown that episodic NIWs have horizontal currents comparable to internal wave sound speed variations and therefore could be an important scatterer of acoustic energy. This issue will be taken up in later work.

2.2.4 Displacement and Spice

Sound speed fluctuations in the ocean can be driven by vertical displacements, which advect the strong vertical gradients, accordingly there is

$$\delta c(r,t) = \left(\frac{dc(z)}{dz}\right)_p \zeta(r,t), \tag{2.2}$$

where the important factor is $\left(\frac{dc(z)}{dz}\right)_p$, the potential sound-speed gradient, i.e., the total gradient minus the adiabatic gradient [Colosi, 2016]. To quantify the space/time scales of displacements, the DVLA moored CTD observations were used, and standard isopycnal tracking techniques were applied [Colosi et al., 2013, Colosi, 2016, Duda et al., 2012, DiMaggio et al., 2018]. Potential density, $\sigma_0[z(t),t]$, [Talley, 2011], referenced to the surface (0 dbar), was computed as a function of instrument depth $z(t)$ and time t. Next, the depths of 33 isopycnals were computed at approximately 10-m depth intervals using depth-linear interpolation. Fig. 2.7 shows the entire record for 33 tracked isopycnals as

well as an expanded region over 20 days. Many space and time scales are evident, as well as intermittency.

Eddies are evident between yeardays 285 and 315, and perhaps some eddy filaments or submesoscale structures are seen after yearday 500. Short time scale fluctuations (less than the inertial period) are evident in the records and are clearly variable in time (more later).

The isopycnal tracking method allows us to quantify temperature and salinity variations along isopycnals, refered to as spice (Fig. 2.8). For an isopycnal between the ASW and the PSW, the T and S variations are large, leading to sound speed variations of several m/s (Fig. 2.8 upper). For a deeper isopycnal between the PWW and AW, T, S, and sound speed variations are small. Fig. 2.9 shows the time/depth structure of the spice. It is also seen that spice is strong in the upper 100 m and drops significantly in the Beaufort Duct and the AW. This result is consistent with the T/S diagram.

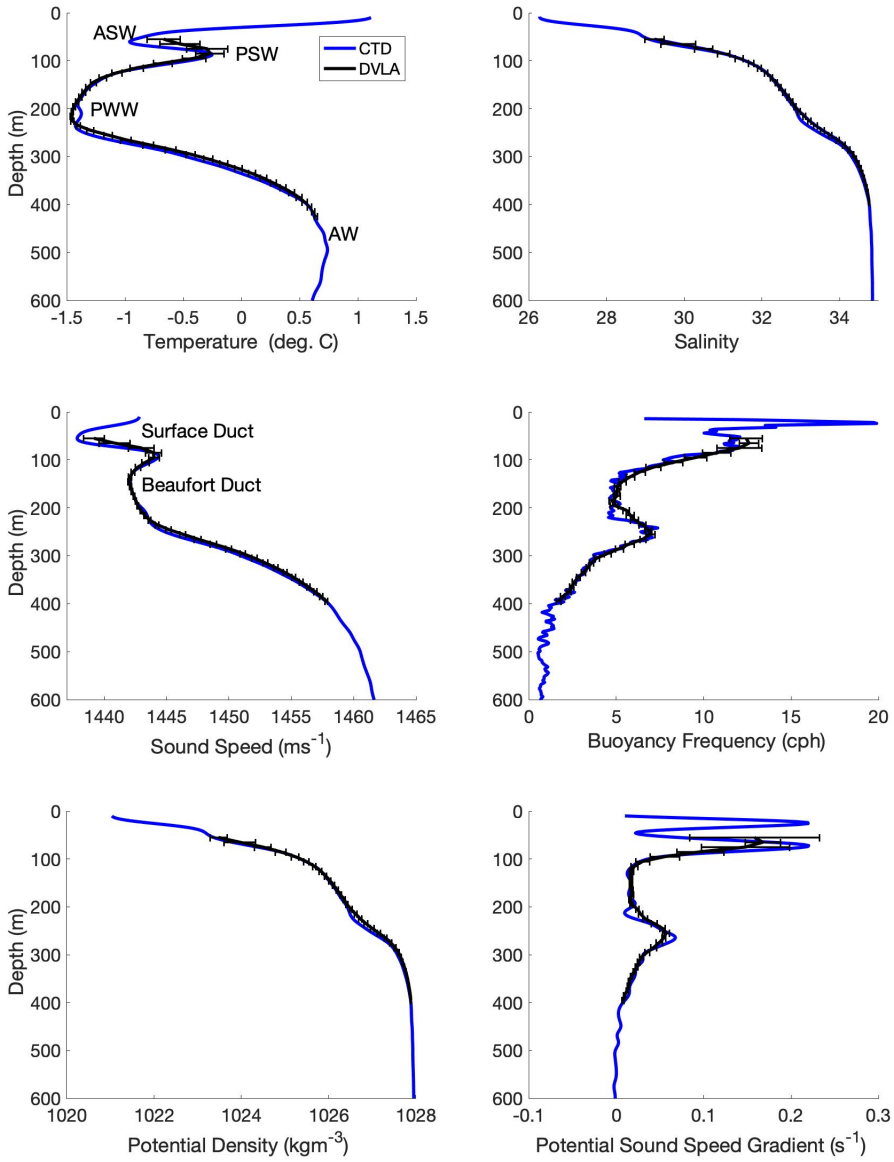

Figure 2.2: Mean profiles of temperature, salinity, sound speed, buoyancy frequency, potential density, and potential sound-speed gradient in the upper 600 m. Root Mean Square (RMS) statistics derived from the DVLA are shown with black lines. Average profiles derived from CTD casts made near the DVLA during the deployment and recovery cruises are shown with blue lines.

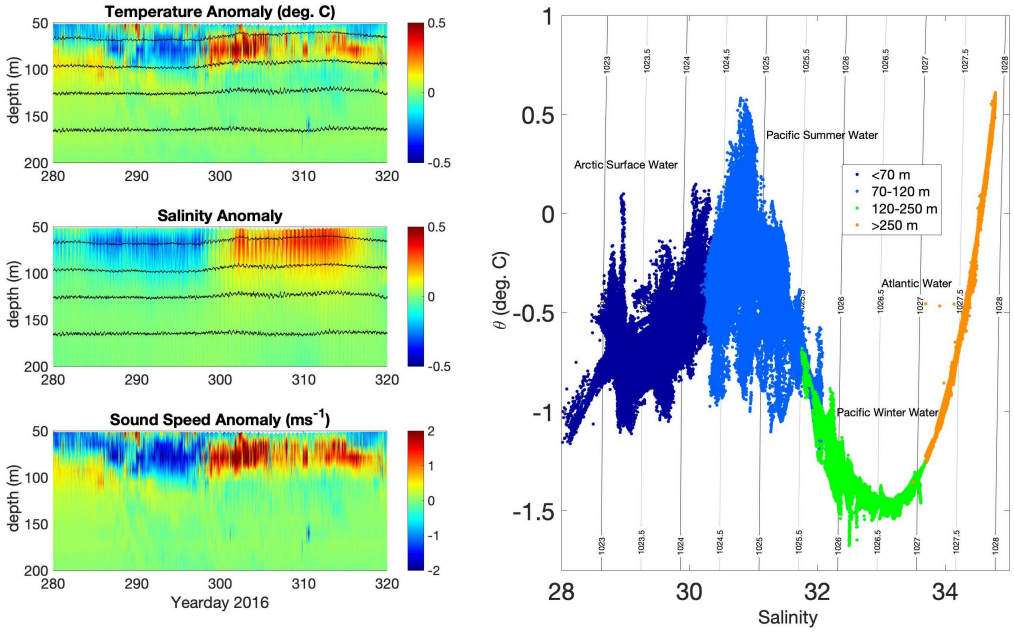

Figure 2.3: Left panels shows the depth-time series of temperature (top), salinity (middle) and sound speed anomalies (bottom) in the upper 200 m at the DVLA mooring between 6 October (yearday 280) and 15 November 2016 (yearday 320). A few isopycnals 1024, 1025.2, 1025.8, 1026.2 kg m^{-3} are overlaid in black. Right panel shows the potential temperature as a function of salinity illustrating the water mass properties at the DVLA mooring between 16 September 2016 and 13 June 2017. Black lines are the contours of potential density. Colors represent depth regions (see legend), as well as the labeled water masses.

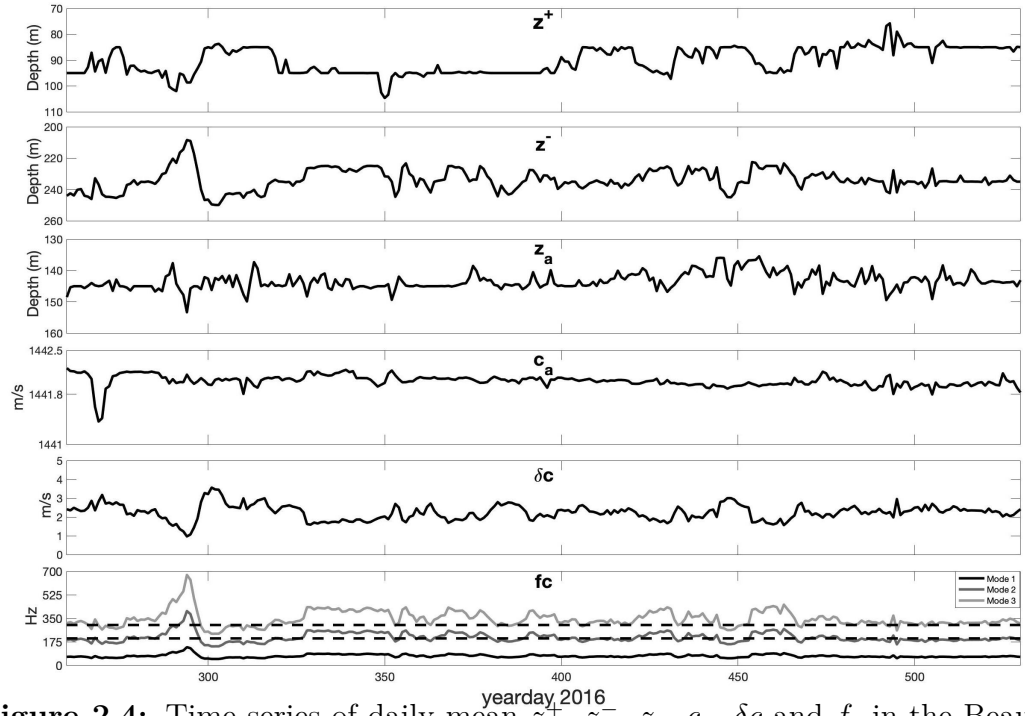

Figure 2.4: Time series of daily mean z^+, z^-, z_a, c_a, δc and f_c in the Beaufort Duct at the DVLA mooring between 16 September 2016 (yearday 260) and 13 June 2017 (yearday 530). The cutoff frequency, f_c, is computed using Eq. 1 for modes 1 to 3 in the bottom panel (black, dark grey, grey). The CANAPE low frequency band extending from approximately 200 to 300 Hz is indicated with dashed horizontal lines.

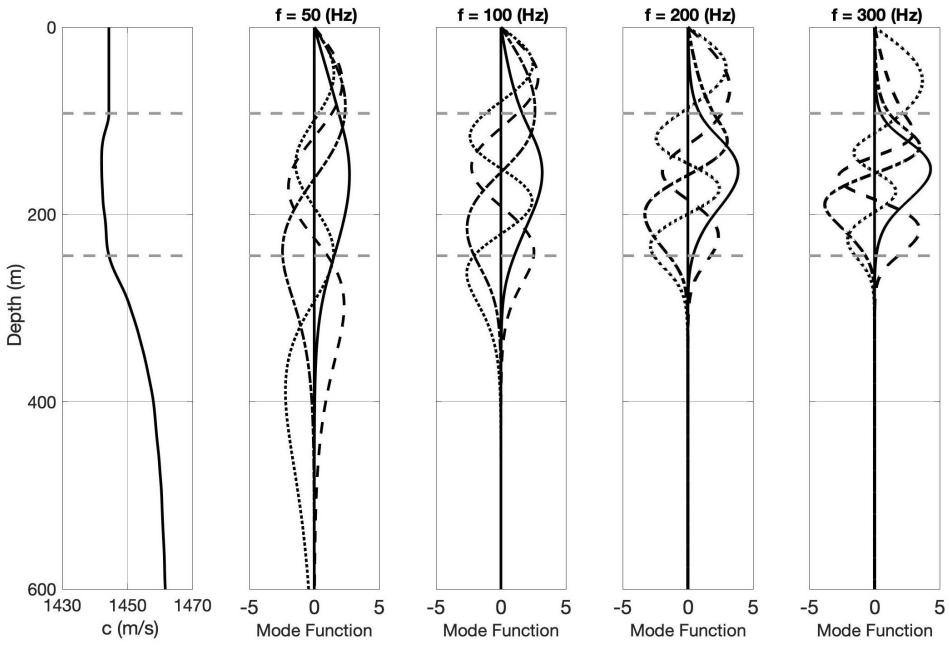

Figure 2.5: Beaufort Duct mode functions at 50, 100, 200 and 300 Hz are displayed for the mean sound speed profile in Fig. 2.2 after modification to remove the surface duct (solid line, Mode 1; dashed-dotted line, Mode 2; dashed line, Mode 3; dotted line, Mode 4). The surface duct is removed to focus on the Beaufort Duct trapping behavior. Gray dashed lines indicate the upper and lower boundaries of the duct.

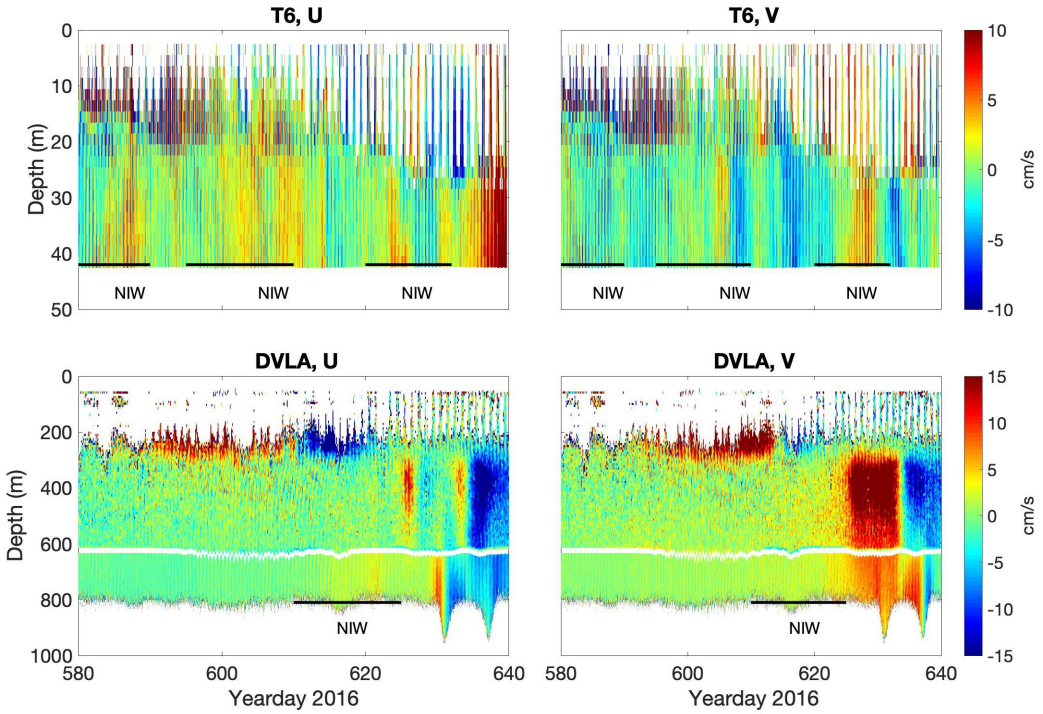

Figure 2.6: Horizontal velocities as a function of depth and time, measured between 2 August (yearday 580) and 30 September 2017 (yearday 640). Upper graphs show depth-time series of u and v velocities at the T-6 mooring, and lower graphs show depth-time series of u and v velocities at the DVLA mooring. The convention is u positive East and v positive North. Horizontal black lines indicate the approximate periods of the relatively strong NIWs

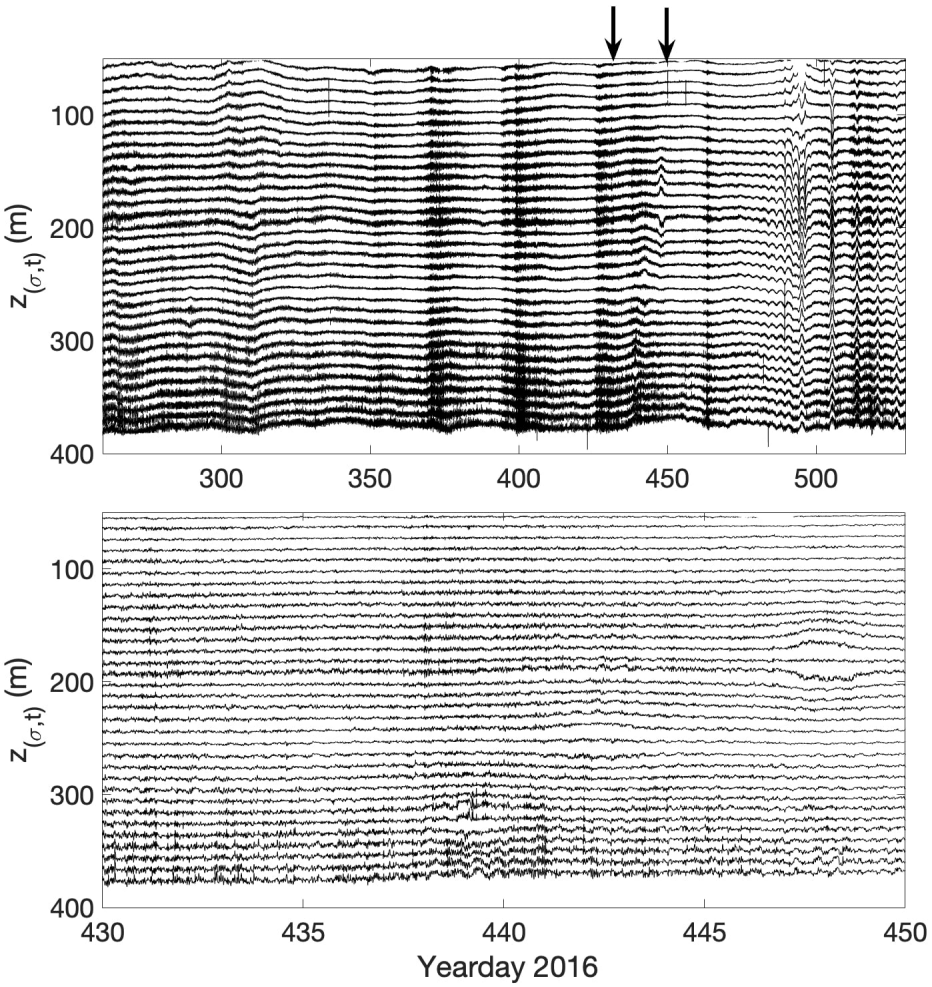

Figure 2.7: Thirty-three tracked isopycnals as a function of depth and time at the DVLA mooring between 16 September 2016 (yearday 260) and 13 June 2017 (yearday 530) (upper) and between 5 March (yearday 430) and 25 March 2017 (yearday 450) (lower). After 13 June 2017, several of the SBE37's below 150-m failed. Isopycnals are roughly separated by 10 m on average.

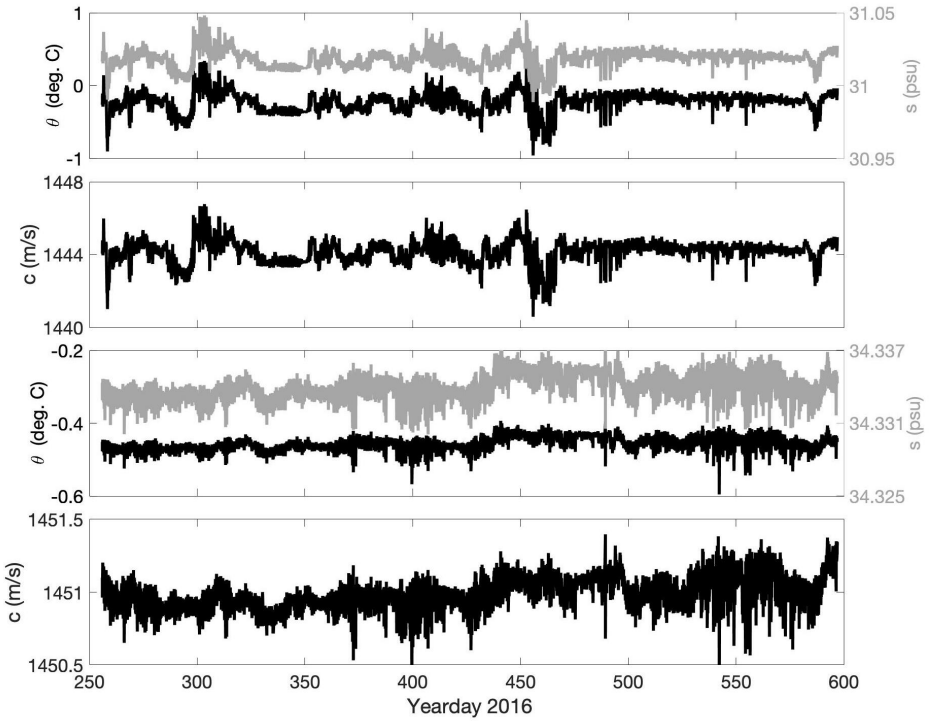

Figure 2.8: Temporal fluctuations of sound speed, potential temperature and salinity along the isopycnal 1024.9 kg m^{-3} at 84.5-m depth (upper panels) and 1027.6 kg m^{-3} at 295.15-m depth (lower panels) between 16 September 2016 (yearday 260) and 19 August 2017 (yearday 597).

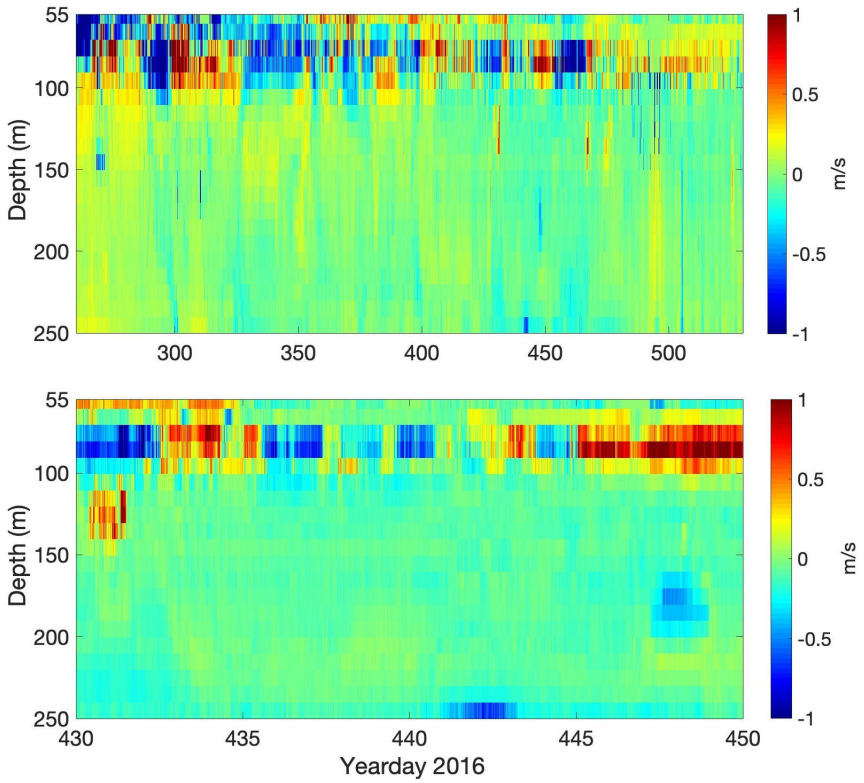

Figure 2.9: Depth-time series of spicy sound-speed anomalies measured at the DVLA mooring between 16 September 2016 (yearday 260) and 13 June 2017 (yearday 530) (upper) and between 5 March (yearday 430) and 25 March 2017 (yearday 450) (lower).

2.3 SPECTRA

In this section the frequency spectra of isopycnal displacements related to eddies, internal waves and internal tides are quantified as well as the spectra of spicy sound speed anomalies generated by T and S anomalies along isopycnals. The RMS variability of these quantities as a function of depth is also presented.

2.3.1 Internal Waves, Internal Tides and Eddies

Fig. 2.10 shows the frequency spectra of vertical displacements for two periods, 16 September 2016 to 28 February 2017 (upper) and 1 March to 13 June 2017 (lower). During both periods, most of the energy in the internal wave band occurs in the near-inertial frequency region, from f–$1.1f$, where f is Coriolis frequency. Energy decreases just below the inertial frequency, and then it rises again at lower frequency due to eddy activity. Interestingly, in the internal wave band, there is a moderate peak at twice the tidal/inertial frequency. The spectra show that a more energetic eddy field exists during the later part of the year.

The RMS variation of vertical displacements with depth is shown in Fig. 2.11. In the internal wave band, the observations are compared to WKB scaling, and the agreement is excellent for a reference internal wave displacement of 1.5 m. This can be compared to the GM reference value of 7.3 m, which yields an average observed internal wave energy level that is roughly 5% of the GM value. The sub-inertial RMS displacements are seen to be roughly twice those in the internal-wave band, and this means that the sub-inertial variance accounts for 80% of the total.

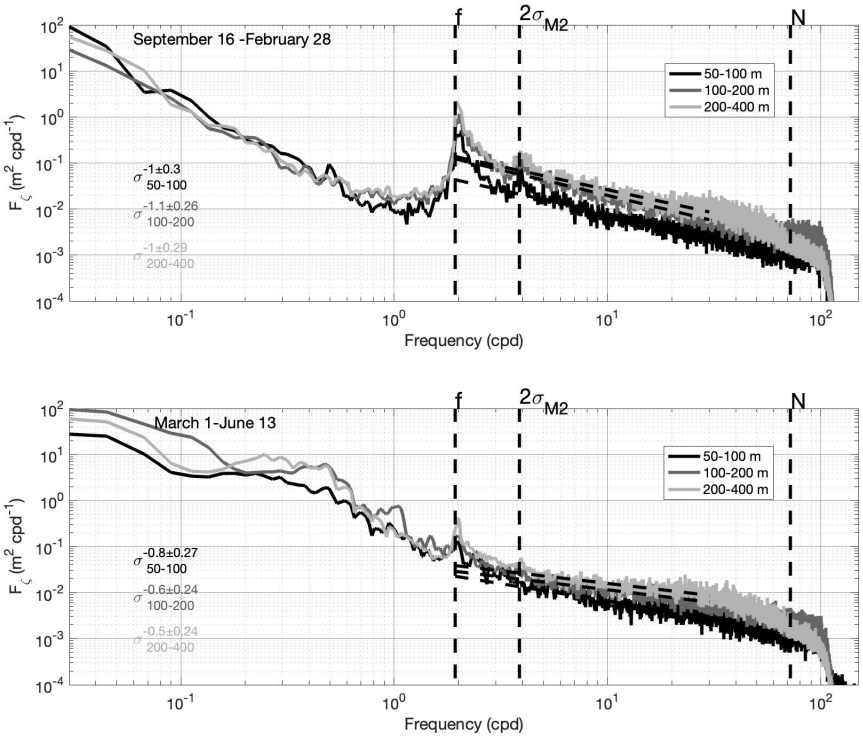

Figure 2.10: Frequency spectra of isopyncal displacements for different depth bands (black, dark grey, grey) and different time periods (upper/lower). The Coriolis frequency, f, typical buoyancy frequency, N, and twice tidal frequency are indicated with dashed vertical lines. Power-law fits (dashed lines) to the spectra between 2 and 30 cycle per day (cpd) are shown along with their power law exponents.

2.3.2 Spice

Frequency spectra of spicy sound speed fluctuations were computed for the same three-depth bands and time periods as the isopycnal displacement spectra (Fig. 2.12). These spectra show a slight peak near the inertial frequency in the depth band 200-400 m but not in the depth bands 100-200 m and 50-100 m. The spice spectra are quite different from the displacement spectra and show less time dependence.

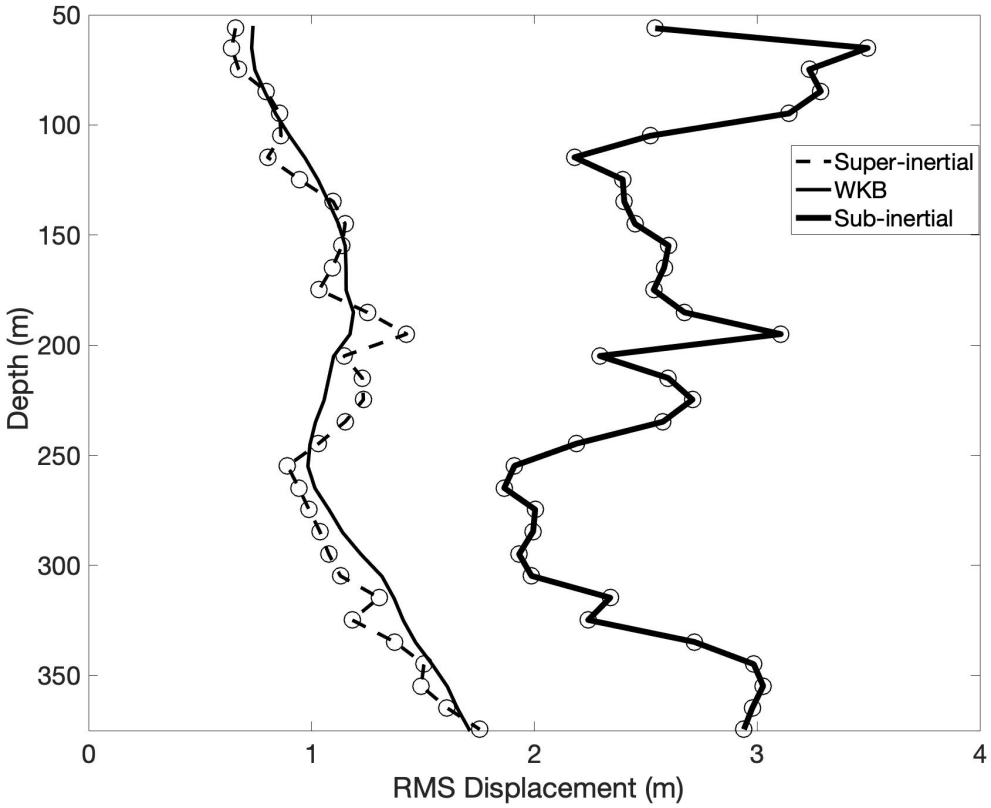

Figure 2.11: RMS displacement versus depth in the super-inertial (dash) and sub-inertial bands (bold solid). The WKB equation, $\langle \zeta^2 \rangle = \zeta_0 \sqrt{N_0/N(z)}$, using a reference internal wave displacement $\zeta_0 = 1.5$ m is plotted as a thinner solid line.

The RMS sound speed perturbations from spice and displacement are shown in Fig. 2.13 with contributions from the internal wave band shown separately from the sub-inertial contributions. RMS displacement is converted to RMS sound speed using Eq. 2. Here we see that spice dominates the upper ocean, while displacements and spice have more comparable contributions deeper down. The deep perturbations are weak indeed.

For the internal wave band, the spice is the more significant contributor to the sound speed variability in the upper 100 m. From 100 to 200 m, spice and

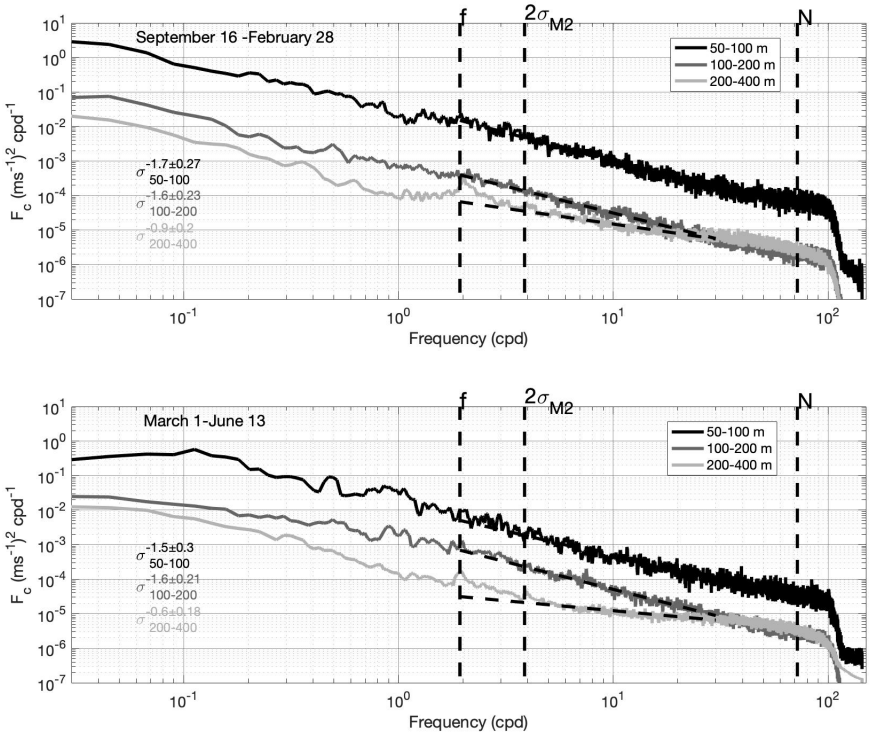

Figure 2.12: Same as Fig. 2.10, except for spicy sound speed fluctuations.

displacement contribution are comparable, except for the axis of the Beaufort Duct. However, the fluctuations due to vertical displacements induced by internal waves start to dominate below 200 m. For the sub-inertial band, spice is the larger contributor from the surface to 100-m depth.

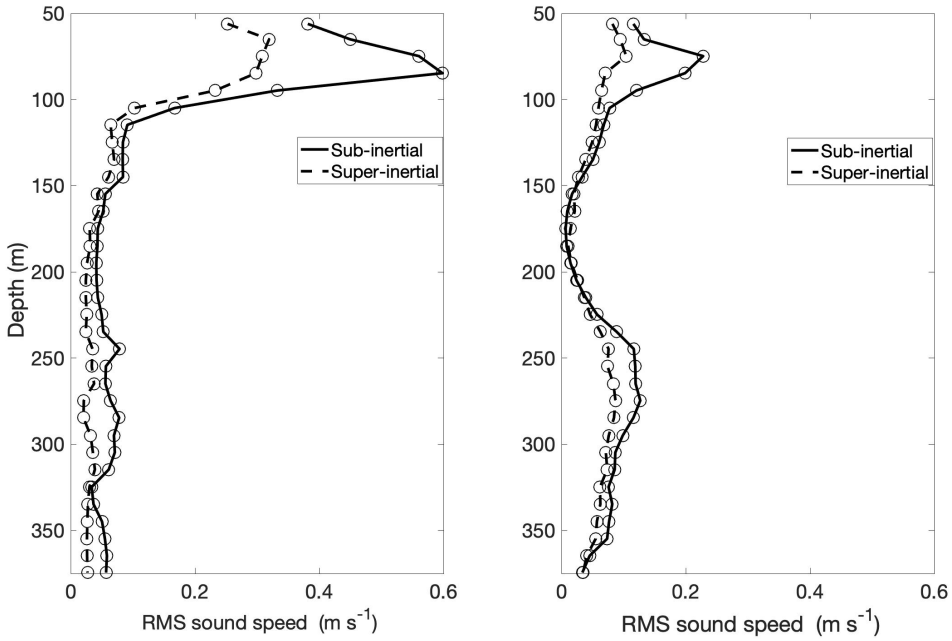

Figure 2.13: RMS sound speed for spice (left) and displacement (right) versus depth in the super-inertial (dash) and sub-inertial bands (solid).

2.4 NEAR INERTIAL WAVES

As seen in the previous section, the sound speed perturbations in the Canada Basin due to internal waves and spice are generally small compared to those in other oceans. This implies that acoustic variability from these processes will be less significant than in other oceans. However, ADCP observations from this experiment suggest another source of acoustic variability, namely upper ocean episodic, energetic near inertial wave (NIW) horizontal currents. Generally, small-scale inertial wave horizontal currents are neglected in fluctuation studies because sound speed fluctuations dominate (i.e., $\delta c >> u$) but NIW events where this condition breaks down were observed. There is a well developed literature on acoustics in moving media, particularly in the atmospheric acoustics setting [Ostashev and Wilson, 2015]. Here a sufficient view under the assumptions of low Mach number and small angle forward scattering is that an opposing/reinforcing current acts like a low/high sound speed zone.

The ADCP observations in this study are not ideal for quantifying NIW space and time scales. The 75 and 150 kHz ADCPs sample the depth region of approximately 300-800 m where NIWs are weak. This is because NIWs are generated at the surface by wind action. They propagate slowly down the water column, weaken as they propagate into lower stratification, and experience some loss [D'Asaro, 1985, Hebert and Moum, 1994]. The upper ocean 600 kHz ADCPs are in a good water column location with strong stratification, but they have a limited depth sampling range (approximately 10-30 m) and are subject to large mooring motion effects. Be that as it may, the 600 kHz ADCPs on moorings T1-T6 provide a peek into the space-time scales of NIWs. The NIW analysis goes as follows. First, the observed hourly horizontal velocities (u, v) were corrected for the mooring motion. The T-moorings and DVLA were navigated using three

to four bottom transponders that allow solution for the (x,y,z) position of the hydrophone elements using acoustic travel times. A position was computed every hour, thus allowing estimation of the horizontal mooring velocity at adequate temporal resolution for NIW motions. The mooring-motion-corrected velocities were then high-pass filtered with a cutoff frequency of 1/4 cpd giving the data used in the analysis, (u_c, v_c) (Fig. 2.14). The NIWs are modeled as vertically propagating, anticyclonic (clockwise), circularly polarized currents that can be written in the form

$$u_m(z,t) = A(z)\sin(mz - ft) \tag{2.3}$$

$$v_m(z,t) = -A(z)\cos(mz - ft), \tag{2.4}$$

where $A(z)$ is a depth dependent current amplitude, m is a constant vertical wave number (no refraction), and $f = 2\Omega\sin(\text{latitude})$ is the inertial frequency with Ω the earth's angular velocity. Here, $z = z(t)$ because of the mooring motion pull down. Solution for $A(z)$ is a simple exercise in least square analysis, but not so for m. Therefore, multiple fits for a range of m values (-0.5 $< m <$ 0.5 cpm) were generated, and m that gives the least residual were chosen. Here positive m means upward phase and downward energy propagation. A 48-hour time and 20-m depth window were chosen for doing the fits, thus giving time dependent estimates of the current amplitude and vertical wave number. Noise and tilting of the moorings results in some errors in vertical wave number calculations, particularly for deep NIW currents at the DVLA, where some values of m are negative. Table IV lists some statistics of the amplitude and vertical wave number fits for the six T moorings. Figures 2.14 and 2.15 show example fits for two energetic NIW packets.

Fig. 2.15 shows one of the most energetic NIW events observed, which lasted

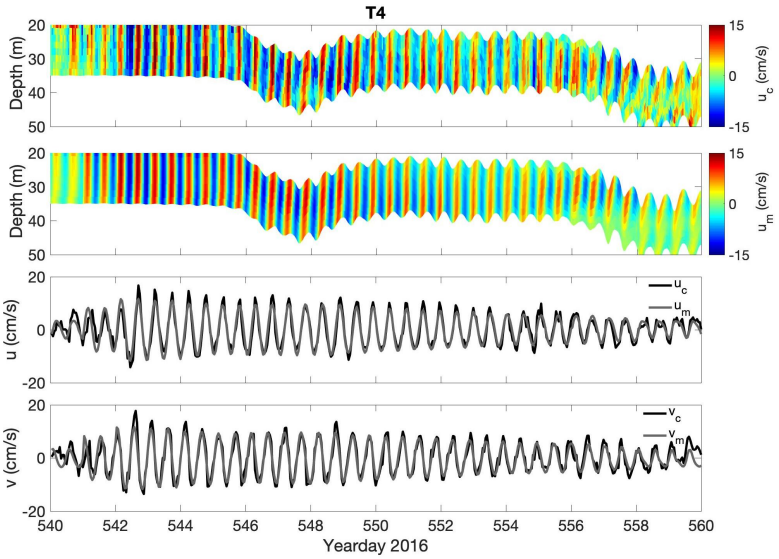

Figure 2.14: Mooring T4 NIWs currents showing u_c and u_m (upper panels) for the period 23 June (yearday 540) to 13 July 2017 (yearday 560). Depth-averaged currents u_c, v_c (black) and u_m, v_m (gray) (lower panels). The convention is u positive East and v positive North.

Table 2.4: Statistics of the fits for the T moorings

	T1	T2	T3	T4	T5	T6
Date	2-5 Oct	4-8 Oct	1-7 Jan	23 Jun-12 Jul	21-25 Oct	23-29 Jun
Mean Amplitude (cm/s) [1]	8.38	10.29	14.01	7.49	12.24	7.22
RMS Amplitude (cm/s)	2.61	2.21	4.71	3.12	5.33	2.11
Vertical Wave number (cpm)	0.041	0.003	0.092	0.013	0.059	0.05
RMS Vertical Wave number (cpm)	0.018	0.001	0.054	0.009	0.037	0.028

5-10 days during mid-winter ice conditions. The currents reach a peak of 20 cm/s and are relatively uniform in depth. The rotary spectra confirm the anticyclonic circulation of the waves. The geographic and temporal variability of the NIWs are shown in Fig. 2.16 including NIW estimates from the deep observations from the DVLA. As previously mentioned, the deep NIW currents observed on the DVLA are quite weak in comparison to the upper ocean currents [Worcester et al., 2018].

Fig. 2.16 shows that in general NIW energy is larger when there is no ice cover, but there are some significant events in the presence of ice, including the

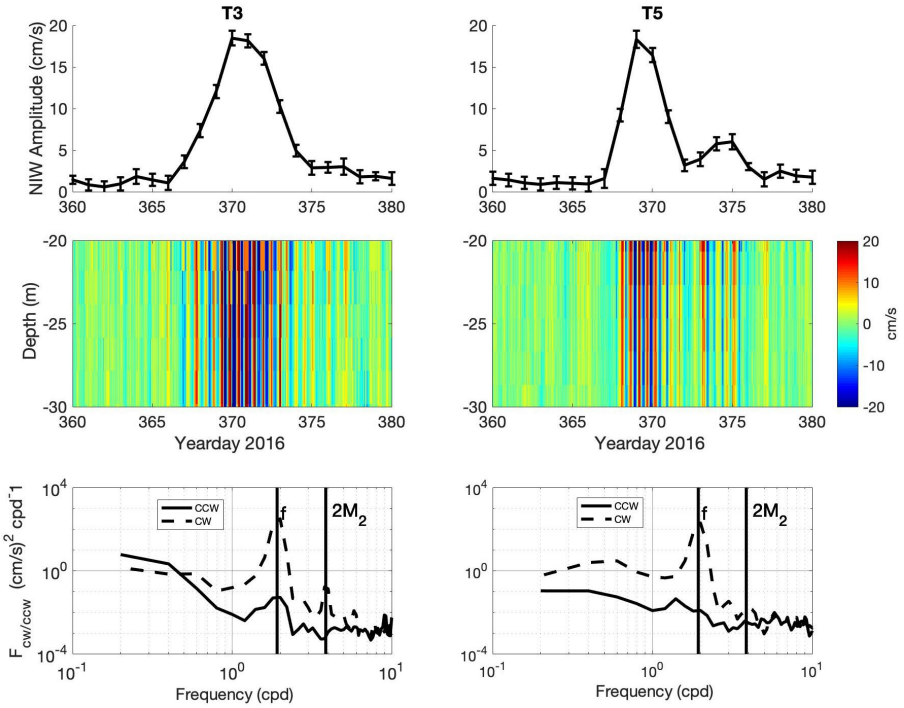

Figure 2.15: Depth-averaged NIW amplitude with error bars (upper), observed near-inertial wave packets (middle) and rotary spectra (lower). Clockwise (CW) rotation is plotted as a dashed line, and counterclockwise (CCW) rotation is plotted as a solid line. Mooring T3 is on the left and T5 on the right, and the time interval is between 25 December 2016 (yearday 360) and 14 January 2017 (yearday 380).

largest events in the record around yearday 370 at the T-moorings. They are not observed at DVLA as the measurements were made deeper in the water column. There is not much coherence between the NIW signals across the array except for the aforementioned large event.

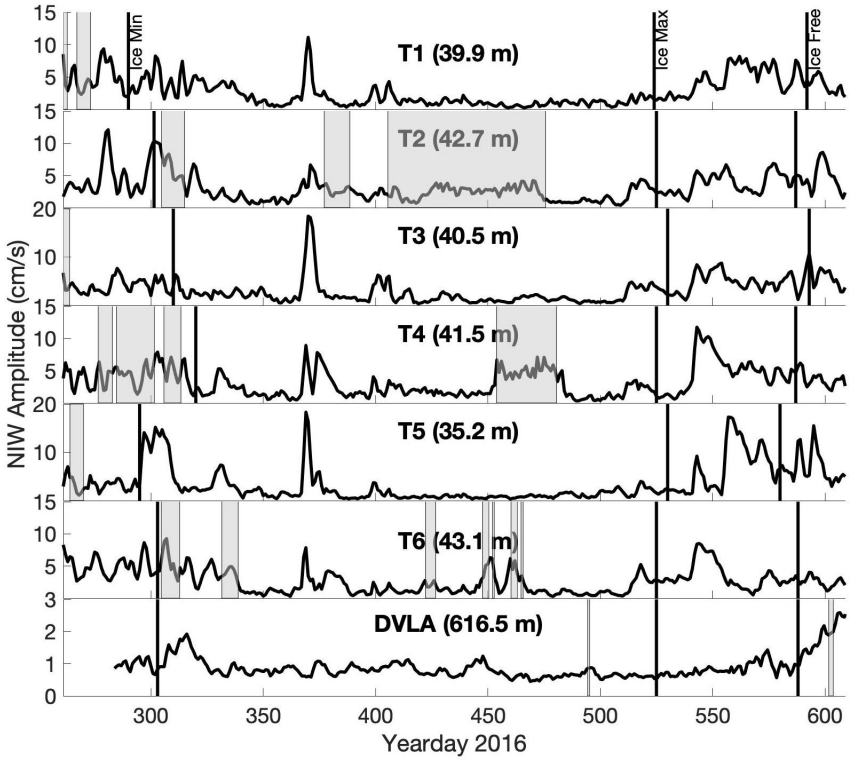

Figure 2.16: Depth-averaged NIW amplitude at the T-moorings and DVLA between 16 September 2016 (yearday 260) and 31 August 2017 (yearday 609). Gray regions indicate the mooring pull-down events bigger than 30 m. Vertical lines show the ice minimum, ice maximum, and ice-free periods, estimated from 11 to 12 kHz acoustic scattering measurements off the ocean surface. Each title is labelled with approximate depth of ADCP.

2.5 SUMMARY AND CONCLUSIONS

In this work, the thermohaline and current structure of the Beaufort Sea are studied from the yearlong moored CANAPE data and ship CTD observations (e.g. Fig. 2.2). Water masses of ASW, PSW, PWW and AW were characterized by temperature and salinity properties, and two haloclines were observed. This environment creates two well-known sound channels, a strong surface duct extending to 75.8-104.7 m depth and a weaker Beaufort Duct below the surface duct extending to 208.4-255.2 m depth. Sound speed variability was quantified in the deeper section of the surface duct and through and below the Beaufort Duct. In this upper ocean region internal wave vertical displacements are seen to be small (Fig. 2.11) and the resulting sound speed perturbations are correspondingly small especially through the axis of the Beaufort Duct where the sound speed gradient is small (Fig. 2.13). The largest observed sound speed variability is in the 50-100 m depth range and is due to spice (Fig. 2.13). It is expected that this strong variability would extend all the way to the sea surface. This variability implies that surface duct acoustic propagation will experience scattering not only from the sea surface but also the water column. In addition, the upper ocean variability determines the upper bound on the Beaufort Duct modifying mode trapping (Fig. 2.5). Specific acoustic effects occurring here will be the focus of future work analyzing the long range transmission data. While the observations have quantified the depth and time scales of sound speed variability, an important open question concerns the horizontal scales and possible inhomogeneity and anisotropy.

In summary, significant fluctuations were observed from eddies, and smaller changes were seen within the super-inertial or internal wave band. Displacement spectra were used to quantify this variability, and the shapes and energy levels of the spectra are seen to vary with depth and season (Fig. 2.10). For example,

an enhanced eddy field was observed during spring and summer. In addition, the super-inertial spectra vary significantly over season and depth and do not agree with the GM spectral shape. On the other hand, a strong peak at tidal/inertial frequency and a moderate peak at twice tidal frequency existed in all depths and seasons. In the upper 100 m, the frequency spectra of displacement had a rather flat spectral slope in the frequency range of 2 to 30 cpd with values of –0.8 to –1 (Fig. 2.10). In comparison the spicy sound speed spectra shows power law slopes of of –1.5 to –1.7 (Fig. 2.12). Regarding the RMS displacement in the super-inertial band, it is found to be consistent with the WKB approximation using a reference level $\zeta_0 = 1.5$ m, which is approximately 20% of GM level (Fig. 2.11). The sub-inertial RMS displacements were responsible for nearly 80% of the total variance indicating the dominance of eddies.

Finally, the current amplitudes and vertical wave numbers were fit by a NIW model. Larger amplitudes appeared mainly under the ice-free surface, and the majority of them were downward propagating waves with anticyclonic circulation. A striking feature of NIW amplitude is that a big wave packet was observed at nearly all the moorings roughly between yearday 360 and 380 under the surface of thin ice. These wave packets caused significant variations in horizontal current in the upper ocean but did not seem to penetrate into the deeper ocean ($\sim$ 500-m) where there were other ADCP observations at the DVLA. It remains to be demonstrated that these strong inertial currents (up to 20 cm/s) are acoustically significant though spectra of observed travel times show an inertial peak [Worcester et al., 2018].

In this work sound speed and current variability from eddies, internal waves, spice and NIWs have been quantified with the aim to use this information in the interpretation and modeling of the long range low frequency transmissions made

across the CANAPE array. Specifically, the impacts of these structure on normal mode propagation in the surface duct and Beaufort Duct will be investigated and analyses will be carried out to study the variability of ray-like time front arrivals.

Acknowledgments

This research was supported by the Office of Naval Research (ONR) and the author, Murat Kucukosmanoglu was supported by an ONR Ocean Acoustics Graduate Student Fellowship under Award Number N00014-19-1-2203. The 600 kHz ADCP and IPS ice draft data were supported by the ONR Arctic and Global Prediction Program (ONR 322AG) under Award Number N00014-15-1-2782. This material is based on work supported by the ONR under Award Number N00014-15-2068. Any opinions, findings, and conclusions or recommendations expressed in this publication are those of the authors and do not necessarily reflect the views of the ONR.

APPENDIX: Derivation of the trapping rule for a two turning point duct

Assume there is a symmetric bi-linear duct with sound speed gradient γ. The duct has axial sound speed c_a and a vertical extent δz between two turning points z^- and z^+. The sound speed at the turning points is $c_m = c_a + \gamma\delta z/2$. The two turning point quantization condition [Colosi, 2016] for a symmetric profile is used to get the cutoff or minimum frequency, ω_{min}, and is given by

$$2\omega_{min}\int_{z_a}^{z^-}\sqrt{\frac{1}{c^2(z)}-\frac{1}{{c_m}^2}}\,dz = \pi(n-1/2). \tag{2.5}$$

Using $c(z) = c_a + \gamma(z - z_a)$, the definition of c_m, and the fact that the gradient is weak Eq. 1 can be approximated by

$$\frac{2\omega_{min}}{c_m}\int_{z_a}^{z^-}\sqrt{\frac{\gamma\delta z}{c_a}-\frac{2\gamma(z-z_a)}{c_a}}\,dz = \pi(n-1/2). \tag{2.6}$$

The integral can be solved yielding

$$\omega_{min} = \left(\frac{c_a^3}{2\gamma}\right)^{1/2}\left(\frac{2}{\delta z}\right)^{3/2}\frac{3\pi}{4}(n-1/2), \tag{2.7}$$

where $c_m \simeq c_a$ are used. Writing $\gamma = 2\delta c/\delta z$ it can further be written as

$$\omega_{min} = \left(\frac{c_a^3}{\delta c}\right)^{1/2}\frac{1}{\delta z}\frac{3\pi}{2\sqrt{2}}(n-1/2), \tag{2.8}$$

with $f_{min}(\mathrm{Hz}) = \omega_{min}/2\pi$.

Chapter 3

Beaufort Sea Observations of 11 to 12.5 kHz surface pulse reflections near 50 degree grazing angle from summer 2016 to summer 2017

Abstract

Sea-surface acoustic scattering is investigated using observations from the 2016-2017 Canada Basin Acoustic Propagation Experiment (CANAPE). Motions of the low-frequency acoustic source and/or receiver moorings were measured using long-baseline acoustic navigation systems where signals transmitted once per hour by the mooring instruments triggered high-frequency replies from bottom-mounted transponders. The moorings recorded these replies giving direct path and single-bounce surface-reflected arrivals having grazing angles near 50°. The reflected signals are used here to quantify surface scattering statistics in an opportunistic effort to infer changing ice characteristics as a function of time and space. Five scattering epochs are identified: 1) open water, 2) initial ice formation, 3) ice solidification, 4) ice thickening, and finally 5) ice melting. Significant changes in ice scattering observables are seen using arrival angle, moment of reflected intensity and its PDF, and pulse time spread. The largest changes occurred during formation, solidification and melting. Statistical characteristics across the experimental region are similar suggesting consistent ice properties. To place the results in some physical context, they are interpreted qualitatively using notions of partial and fully saturated wave fields, a Kirchhoff-like approximation for the rough surface, and a thin elastic layer reflection coefficient model.

3.1 INTRODUCTION

The state of sea ice in the Arctic Ocean has been of great concern in the last two decades because it has become much younger and thinner with a dramatic decline in multi-year ice [Serreze and Meier, 2019, Maslanik et al., 2011, Wadhams, 2012, Frey et al., 2015, Krishfield et al., 2014, Worcester et al., 2020, Mikhalevsky et al., 2015, Kwok, 2018, Stroeve and Notz, 2018]. These changes are expected to lead to significant changes in acoustic scattering from ice through changes in sea ice acoustic properties, height and roughness spectrum [Gavrilov and Mikhalevsky, 2006a] and morphological differences between the various types of ice [Wadhams and Doble, 2008]. Therefore as a remote sensing tool, acoustic ice scattering statistics offer some potential for monitoring ice evolution [Bassett et al., 2020]. This paper is a step in this direction by examining a yearlong record of direct-path ice reflection data from the long-baseline (LBL) navigation systems of seven acoustic source and/or receiver moorings deployed in the Beaufort Sea from summer 2016 to summer 2017. These observations were part of the Canada Basin Acoustic Propagation Experiment (CANAPE) [Worcester et al., 2018, Worcester et al., 2020, Kucukosmanoglu et al., 2021] and represent a novel view into the space and time scales of single bounce ice scattering statistics in the 11-12.5 kHz frequency range with incident grazing angles near 50°. In particular, the data are interpreted in terms of identified temporal epochs defined as 1) open water, 2) initial ice formation lasting several weeks, 3) ice solidification also lasting several weeks, 4) ice thickening lasting roughly 6 months, and lastly 5) ice melting lasting roughly 1.5 to 2 months. Observables analyzed here are arrival angle, moments of reflected intensity, its PDF, and pulse time spread. The most variable epochs are observed to be during the transitions, that is the epoch of ice formation, ice solidification, and ice melting.

The statistics of acoustic scattering from ice as a function of frequency and grazing angle [Duckworth et al., 2001, LePage and Schmidt, 1996] are mainly governed by ice thickness, elastic and acoustic properties [Kuperman and Schmidt, 1986], underside and topside roughness [Hope et al., 2017], internal structure such as salt channels, dendritic and frazil ice structures, and keels [Jezek et al., 1990], all of which are spatially and temporally highly variable. In previous modeling studies, variation in ice layer acoustic properties have been shown to cause significant changes in the reflected energy [Alexander et al., 2012, McCammon and McDaniel, 1985]. In experiments, on the other hand, it has been shown that the acoustic energy loss can be attributed to compressional and shear wave attenuation [Jin et al., 1994] and bubbles within the ice [Bassett et al., 2020]. In another experimental study, the loss was ascribed to variations in temperature, salinity, porosity, and density, utilizing the sea ice model of [Laible and Rajan, 1996]. In addition, some experiments have found important differences in high frequency reflection properties due to slushy ice with its skeletal layer giving low reflection and consolidated thick ice giving higher reflection [Jezek et al., 1990, Garrison et al., 1991, Stanton et al., 1986, Williams et al., 1992, Wen et al., 1991]. Ice keels are yet another consideration, creating large-scale surface roughness, which can have a significant impact on acoustic scattering from the ice [Bishop, 1989, LePage and Schmidt, 1994]. Moreover, effects from the rough sea ice surface and ice keels (which may be up to 25 m deep) [Strub-Klein and Sudom, 2012], can lead to lossy out-of plane scattering and high angle scattering where less energy is scattered in the specular direction toward the receiver [Ballard, 2019, Simon et al., 2018]. This study is novel in looking at several acoustic observables over a year duration to try to piece together the relative effects of these aforementioned processes during the

various ice epochs.

A few general comments can be made about how the geometry and environment set the scattering behavior of the measured data. We consider two dimensionless parameters that characterize scattering from point sources, namely Φ and Λ. Φ is defined as root-mean-square (RMS) phase fluctuation experienced by a ray with grazing angle θ impinging on a rough surface with rms height $\langle h^2 \rangle^{1/2}$. Because the acoustic wavelengths are small (12 to 14 cm) compared to $\langle h^2 \rangle^{1/2}$ (which can be as large as 2-m), this means that $\Phi >> 1$. As a result the mean pressure field will be very close to zero since the complex pressure phasor can be pointing in nearly any direction. Consequentially the observed reflected intensity is entirely the incoherent component [Thorsos, 1984a]. Next, consider Λ, which characterizes the role of diffraction in the scattering process. It is defined as the ratio of Fresnel zone radius, R_f, to the horizontal characteristic length of the rough surface, L_h. R_f is defined as the surface region around the specular point in which paths reflecting off this area have phase differences of less than π compared to the specular ray. Paths within a Fresnel zone are considered to be smoothed by diffraction. For $\Lambda << 1$ the scattering is very geometric, that is the sound field can sense all the structure of the roughness. However if $\Lambda >> 1$, then a lot of the roughness structure is smoothed over by diffraction. For the CANAPE geometry R_f is of order several meters while L_h is estimated to be tens of meters [Gavrilov and Mikhalevsky, 2006a], thus $\Lambda < 1$. As a consequence with also having $\Phi >> 1$ interference from different scattering points on the ice are expected to be significant, and therefore the acoustic field statistics should show properties of the partial and fully saturated wave propagation regimes [Colosi, 2016]. In this experimental configuration, the Kirchhoff approximation is expected to be accurate [Thorsos, 1990b, Thorsos, 1988], and there are expressions for the reflected

intensity and the SI which could be evaluated under certain additional conditions [Jackson and Richardson, 2007a, Yang and McDaniel, 1991], but this is not done here, since the focus of this paper is the observations.

The paper's organization is as follows. Section II explains the CANAPE ice reflection observations and describes the methods of analysis. Observed surface scattering statistics such as root mean square (rms) arrival angle, mean reflected intensity, SI, reflected intensity PDF, and pulse time spread are presented in section III. In section IV a review of some scattering theory is presented, and a discussion and synthesis of the results are given. Here the focus is to identify key acoustic scattering processes associated with the seasonal epochs and point the way to future research and modeling. The paper concludes in Section V with a summary of the most important results.

3.2 EXPERIMENTAL DESCRIPTION

The CANAPE experiment was carried out to assess the impact of surface and water column processes on low-frequency sound propagation on varying space and time scales over the annual cycle in the Beaufort Sea [Worcester et al., 2018, Worcester et al., 2020]. The fieldwork occurred between 10 September 2016 and 31 August 2017 utilizing six transceiver moorings (T-moorings with 200-300 Hz sources) and one wide aperture distributed vertical line array (DVLA) receiver mooring [Kucukosmanoglu et al., 2021]. The overall experimental geometry/bathymetry and the locations for all seven moorings arranged in a pentagon pattern are shown in [Kucukosmanoglu et al., 2021]. In this section, the mooring acoustic LBL navigation systems used to obtain the ice reflection data are described, and important beampattern and response characteristics for the hydrophones, which were designed with lower frequencies in mind, are illustrated. Auxiliary information is also discussed, for example, mooring motion behavior and high-frequency ice profiling sonars that provide second by second estimates of ice thickness.

3.2.1 CANAPE Observations: Navigation Ping Receptions

The mooring LBL navigation systems consist of a 9 kHz pinger that is located near the receiving array which interrogates the near omnidirectional Benthos XT-6001-13 expendable transponders (North Falmouth, MA), that are attached to a tether 2 m above the seafloor. The transponders then respond broadcasting at frequencies between 11 and 12.5 kHz with a transmit pulse width of 10 ms ($\pm$1 ms) which are then recorded on the receiving arrays. For the DVLA the responses

are recorded on 60 Scripps hydrophone modules (HM's) (San Diego, CA) between 50 and 590 m depth with nominal 9-m depth separation, while for the T-moorings there are only 15 HM's located between 50 and 180-m depth again with 9-m separation. The DVLA had four transponders (frequencies of 11, 11.5, 12, and 12.5 kHz), and the T-moorings were similarly navigated but only using three transponders (frequencies of 11, 11.5, and 12 kHz). Matched filter processing was used to extract the broadband signals at each frequency with subsequent complex demodulation to obtain the signal envelope. In this study the signal intensity is analyzed but not the phase. Figure 3.1 shows an example geometry. The direct path is used for mooring navigation, usually down to sub meter accuracy, but importantly, a surface bounce is also recorded several hundreds of ms after the direct arrival (Fig. 3.2). Since the goal of this system is hydrophone navigation, the transponders were situated to give roughly 45° arrival angles at the HMs, though the actual range of angles was 50° to 55°. This means that the surface grazing angles are also in this range (assuming straight line propagation).

The HMs for this experiment were designed for the low-frequency signals (communication with Matthew Dzieciuch of Scripps-UCSD) and they have idiosyncrasies at the higher frequencies used by the LBL navigation system. Fig. 3.1 shows a picture of the HM's where the hydrophone part of the module is oriented towards the sea surface (blue section) and the electronics portion is below it (silver section with clamps). The HM is about 61-cm tall and the barrel has a diameter of roughly 6.4 cm. At low frequencies and for long range propagation, the sound comes in mostly horizontally or broadside to the HM, but because the wavelength is much larger than the HM it acts as a point receiver. However, for the navigation pings the sound is coming in at steeper angles and the wavelength is comparable to the HM size. For the direct path coming from the seafloor, the

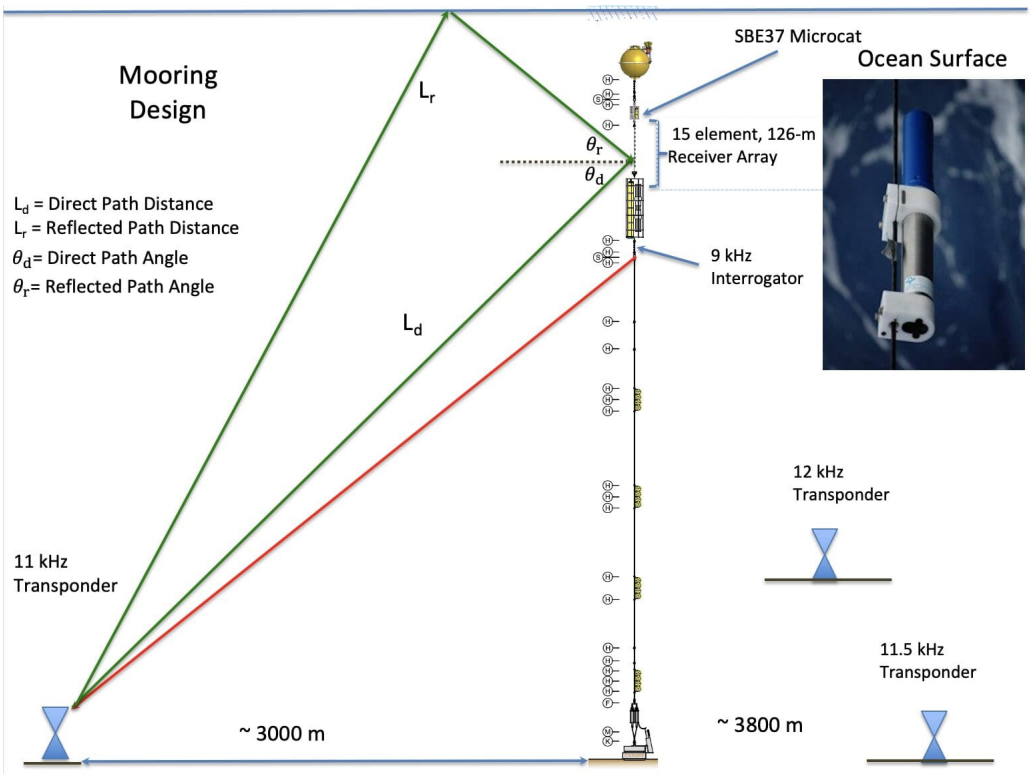

Figure 3.1: Example mooring geometry and propagation paths for the CANAPE T-moorings. In the upper right corner is a picture of one of the hydrophone modules (HMs). The blue section is the transducer, and the silver section with clamps is the electronics housing. The HMs are situated on the mooring in a vertical position with the transducer facing the ocean surface. The SBE37 MicroCATs' principal function is to give precise pressure (depth) measurements.

electronics portion of the HM partially blocks the signal and so a weaker arrival is recorded (Fig. 3.2). On the other hand, the surface-reflected arrival comes down onto the hydrophone section of the HM and therefore is somewhat less affected by the HM shape. To understand this beam pattern effect and to quantify the variability between different HMs a test was performed at the Transducer Evaluation Center (TRANSDEC) in San Diego. Four HMs were evaluated at the transponder frequencies. Fig. 3.3 shows the results for the 11 kHz case which was very similar for the other frequencies. Here the blocking of the direct path by the electronics

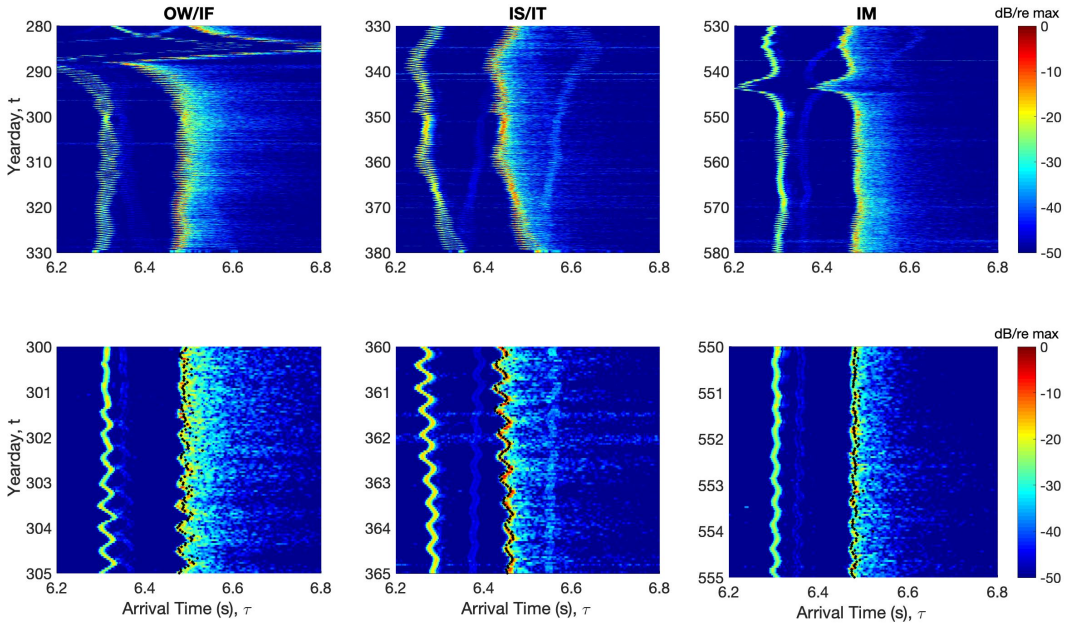

Figure 3.2: Examples of 11 kHz demodulates for a hydrophone located at a depth of 156.4 meters are plotted at the T1 mooring during three different epochs. The upper panels show a 50 day record at hourly intervals (1 ping/hr) and the lower panels show an expanded view over 5 days. Black dots on the lower panels represent the arrival time of the peaks of surface-reflected paths. Measured intensity is normalized by the maximum intensity throughout the year. The abbreviations OW, IF, IS, IT, and IM stand for open water, ice formation, ice solidification, ice thickening, and ice melting, respectively.

package is evident and there is a flatter response for the surface-reflected path. This means that with mooring motion (Fig. 3.4) the direct path will vary more than the surface paths as the angle changes: this makes the direct path intensity much less reliable. For this reason while the direct arrival is used in a few places for this analysis, the focus is primarily on the variability of the surface-reflected arrival. Bottom reflections might possibly interfere with both the direct and reflected paths as an irreducible noise' source, explaining at least part of the variation in direct and reflected path intensities. However, in comparison to the electronics package blocking the direct path, its impact is believed to be minor. Fig. 3.3 also shows some significant variability phone to phone, likely due to the

small wavelength of the transponder pings. This means that the analysis will be restricted to statistics that are only derived from a single phone. That is, vertical correlations of the signals will not be examined.

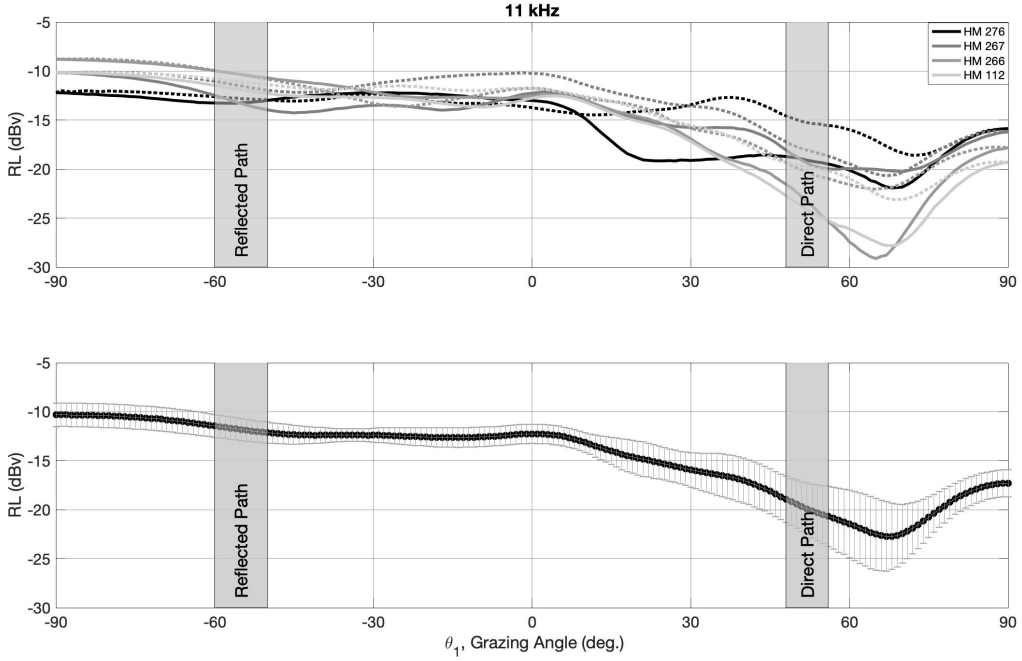

Figure 3.3: Received voltage levels for HMs 276, 267, 266 and 112 (upper panel) and mean voltage levels with error bars (lower panel). Error bars are one standard deviation. HMs were rotated 360 degrees in the tank. Since it is unknown which side of the hydrophone receives the signal, the left (solid) and right (dash) sides are plotted across the identical 180-degree arrival angles. Angles between -90 and 0 are used to represent the angles coming from the sea surface, while angles between 0 and 90 are used to describe the angles coming from the sea floor (Fig. 3.1). Angle -90 denotes the top of the hydrophone, whereas angle 90 denotes the bottom. The vertical gray shaded regions describe the arrival angles of direct and reflected paths.

Returning to Figure 3.2, a time series of the arrival patterns for a given hydrophone and a given bottom transponder from the T1 mooring are displayed. The direct and reflected arrivals are evident, and variability in the time of arrival due to the mooring motion and a large pulldown from an eddy is clear (Fig. 3.4). Also differences in the signal's intensity during the ice epochs is visible. Figure

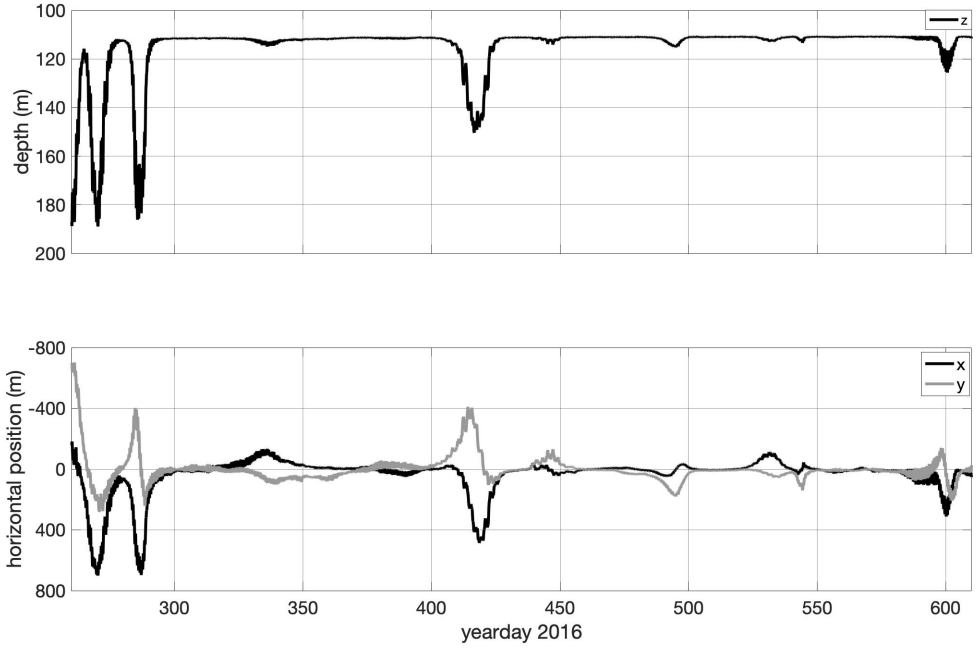

Figure 3.4: Example mooring motion data showing time series of the reference hydrophone's depth (upper panel), x (Easting) and y (Northing) distance from mooring location (lower panel) at the T1 between 16 September 2016 (yearday 260) and 26 August 2017 (yearday 604). The reference hydrophone is in the middle of the array at a depth of 111.5 m.

3.5 shows an example of a 11 kHz time front observed on the DVLA. Open water, thickening ice, and ice melting conditions, are shown and again differences in the received signals are apparent for the different ice epochs.

Given the different slices that can be made through the data set, some notation is required. At a given mooring the received intensity can be written as $I(n, m, \tau, t, \vec{r}_m(t))$ where $n = 1, 2, 3, 4$ is the transponder number, m is the hydrophone number, τ is time in the arrival pattern, t is geophysical time of each transmission, and $\vec{r}_m(t)$ is hydrophone location which changes due to mooring motion. From this data, the intensity (proportional to magnitude squared of complex pressure) and arrival time are determined for the direct and surface-reflected paths, which are labelled as $I_d(n, m, t, \vec{r}_m(t))$ and $I_r(n, m, t, \vec{r}_m(t))$, and

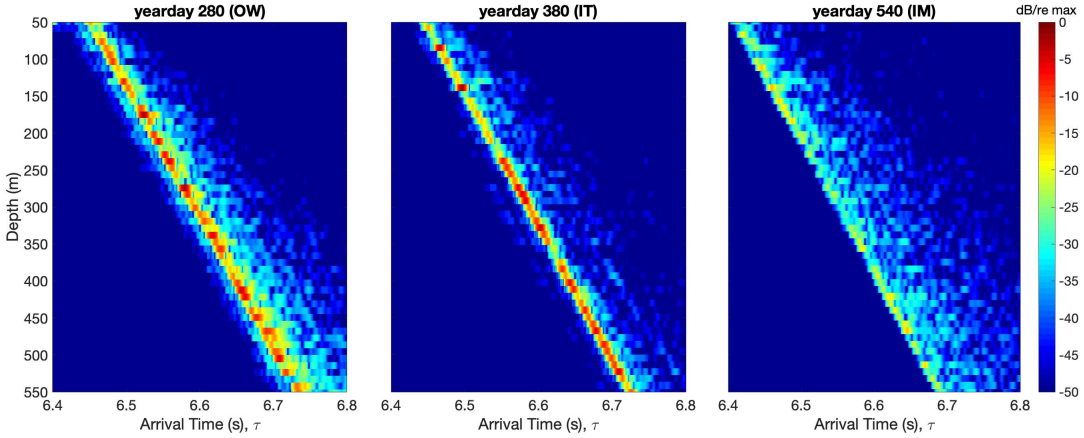

Figure 3.5: Examples of reflected intensity variability taken at the DVLA mooring on yeardays 280 open water (OW), 380 ice thickening (IT) and 540 ice melting (IM). Measured intensity is normalized by the maximum intensity throughout the year.

$\tau_d(n, m, t, \vec{r}_m(t))$ and $\tau_r(n, m, t, \vec{r}_m(t))$. The direct path intensity is easily identified as the peak of the early arrival, which doesn't have any interactions with the surface boundaries. Since the path length is short, it does not experience much scattering by the water column (Fig. 3.2). For the surface-reflected path, the arrival pattern is more complex, and so the maximum intensity is chosen in the pattern. Other intensity metrics such as integrated energy and mean energy were experimented with giving essentially the same results, so it was decided to use the simple approach of using peaks.

The direct path travel times from all the transponders, $\tau_d(n, m, t, \vec{r}_m(t))$, are important because they are used to determine the hydrophone positions $\vec{r}_m(t)$, and in turn correct the long-range transmission travel times for mooring motion leaving only ocean sound-speed effects. The hydrophone navigation is obtained using standard methods [Gaillard et al., 2006]. The hydrophone positions are used in this analysis to compute the direct and reflected path lengths written $L_d(n, m, t, \vec{r}_m(t))$ and $L_r(n, m, t, \vec{r}_m(t))$, where straight-line propagation is assumed (which is an excellent approximation). This allows a spherical spreading corrected intensity to

be written as follows,

$$I_{dc}(n,m,t) = I_d(n,m,t,\vec{r}_m(t))L_d^2(n,m,t,\vec{r}_m(t)) \tag{3.1}$$

$$I_{rc}(n,m,t) = I_r(n,m,t,\vec{r}_m(t))L_r^2(n,m,t,\vec{r}_m(t)). \tag{3.2}$$

The original intention of the work was to form an intensity reflection coefficient using the direct and reflected intensities $R(n,m,t) = I_{rc}(n,m,t)/I_{dc}(n,m,t)$. However, while time series of $I_{dc}(n,m,t)$ were expected to be very stable, they show considerable variability that can be attributed to two factors: 1) a strong variation in the hydrophone response as arrival angle changes (Figs. 3.3 and 3.8) and 2) a weak out of band interference from the different transponders (Fig. 3.2). Phone to phone differences in direct intensity is found to be roughly 15 dB. Therefore, the direct path was deemed unusable for the present analysis, so the focus is exclusively on the reflected path. The weak out of band interference also applies to the reflected arrival and must be considered an irreducible noise. The key factor contributing to the reflected arrival intensity's high quality is the weak variation of the hydrophone response to small changes in arrival angle (Fig. 3.8).

The signal-to-noise ratios (SNR) for the reflected arrivals have been analyzed. Noise intensity is computed within a time window before the direct ray arrives as a function of depth and yearday. Peak intensities at each hydrophone are divided by noise intensities to calculate the SNR with the following equation,

$$\mathrm{SNR}(n,m) = \left\langle 10\log_{10}\left(\frac{I_r(n,m,t)}{\langle I(n,m,\tau,t)\rangle_\tau}\right)\right\rangle_t \tag{3.3}$$

where $\langle\rangle_t$, and $\langle\rangle_\tau$ are averages over t and τ, and $\langle I(n,m,\tau,t)\rangle_\tau$ is the mean noise intensity in the time window away from the signal. The SNR statistics for the DVLA show no significant depth dependence with a mean of roughly 50 dB and

an rms of 12 dB. The other T-moorings show similarly high SNR results.

3.2.2 Ice Analysis

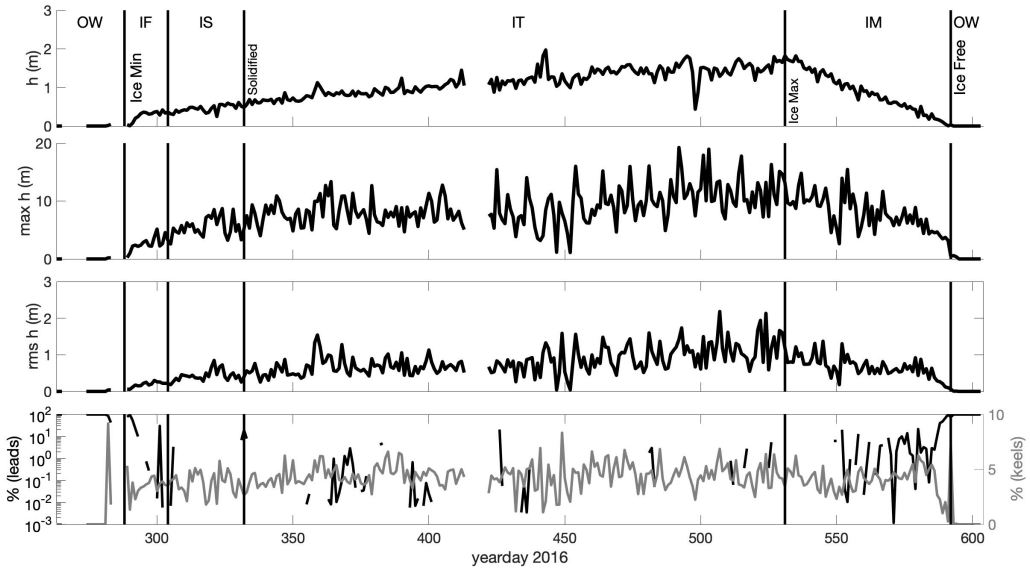

Figure 3.6: Daily mean ice thickness (top), max h (second from top), rms h (third from top), percentage of leads (bottom panel/black color) and percentage of ice keels (bottom panel/gray color) at the T1 mooring between 16 September 2016 (yearday 260) and 26 August 2017 (yearday 604). Vertical lines show the ice minimum, separation of ice formation and ice solidification, solidified ice, ice maximum, and ice-free periods for the T1. The gaps in the lead record correspond to days when there were very few or no leads. The abbreviations are the same as in Fig. 3.2.

All the T-moorings were equipped with 420-kHz ASL Environmental Sciences IPS-5 pencil beam ice profiling sonars that provided ice draft estimates, $h(t)$ every second . Due to the limited acoustic range of these devices mooring pulldowns from eddies resulted in data gaps. For mooring T1, Fig. 3.6 shows the daily mean ice thickness, the daily max ice thickness, the roughness (i.e., rms thickness), and lastly percentage of leads (percentage of time with $h \simeq 0$) and percentage of ice keels (percentage of time with $h > \overline{h} + 2\sigma$). The percentage of ice keels

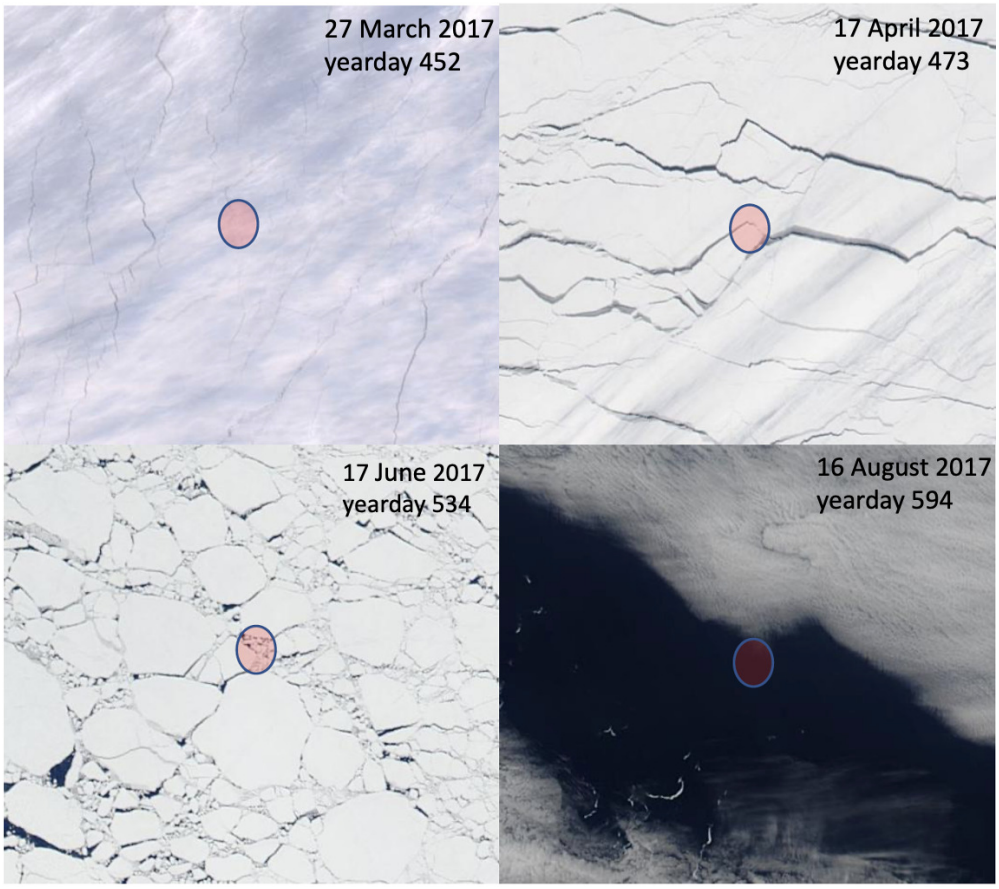

Figure 3.7: Satellite Images illustrating the changes of ice cover at the T1 mooring. Red circles show the exact location of the T1 mooring. Y-axis runs south to north and the x-axis runs west to east. Adapted from https://worldview.earthdata.nasa.gov.

is an estimate subject to our chosen threshold. For example, $\overline{h}$ and σ are 0.98 and 0.59 meters between yeardays 404 and 405, and the keel threshold is found to be equal to 2.16 meters. This approach was applied to all observations in a one-day window when $h(t) > 0$ because ice keels range from less than 1 to roughly 25 m deep [Strub-Klein and Sudom, 2012], and a new keel threshold is computed each day. The T1 mooring is shown here because it had relatively suffered few pull downs. The other mooring records are similar in character but with more gaps. The measurements show that the surface layer is ice-free at the

beginning of the experiment. A steady rise in ice thickness is observed from mid-October to mid-June, along with a slower increase in roughness. The maximum ice thickness exceeds 5 meters after it solidifies, and reaches up to 18 meters during the thickening epoch. The percentage of ice keels is observed to be to less than 5% of the overall ice layer during most of the year, and did not significantly change during the IT epoch. More leads are observed during the epochs of ice formation and ice melting, suggesting the highly variable surface layer structure from water to slush ice or vice versa. A linear regression coefficient (Rsq) is found to be 0.7 between the daily mean ice thickness and the roughness under the ice thickening epoch, but as the ice cover is exposed to more solar radiation during the melting time (ice melting epoch), the roughness does not vary simply with the ice thickness (Rsq = 0.38). It is also important to note that the ice draft, h, is a positive definite quantity, and since the roughness is a large proportion of the mean (Fig. 3.6), the statistics are clearly not Gaussian. Fig. 3.7 displays satellite images of the surface cover from four separate periods of the year at the T1 mooring. The ice was fairly uniform on yearday 452 (ice thickening), with a little more break-up on yearday 473 (ice thickening). More leads are evident on yearday 534 (ice melting), and the ice is almost gone on yearday 594 (open water). Satellite images for ice formation and ice solidification epochs could not be accessed.

3.3 RESULTS

In this section the main results of the analysis are presented. The various statistics presented are generally computed over some small time window (usually 10 days) so that the variation of the statistic over the different ice epochs can be revealed. The first quantities presented are arrival angle statistics derived from an incoherent beamformer. Next, statistics of the reflected intensity including mean intensity and SI are presented, followed by Probability Density Functions (PDF's) of reflected intensity. The last quantity treated is the time (τ) intensity covariance function which gives information about pulse spread.

3.3.1 Beamforming

An incoherent beamforming method using just intensity was applied to the observations in order to estimate arrival angles (See Appendix A). An incoherent approach was used because of the variability in the phone to phone response (Fig. 3.2). Figure 3.8 shows the time dependence of the arrival angle for both the direct and surface-reflected paths, for mooring T1 and the 11 kHz signal. The result here is quite typical of the other moorings. Variations in arrival angle due to mooring pull downs (Fig. 3.4) are evident and agree with arrival angles estimated from the mooring motion. The time dependence of the rms arrival angle for the surface path at the T1 and DVLA moorings is also shown in Figure 3.8. The values change over the year from a maximum of 4.5° during the ice melting epoch to a minimum of 1° during the IT period. The rms angle is interpreted as a metric of the wide-angled-ness of the surface scatter. Largest values are found during the open water, ice formation, and ice melting epochs, and the lowest values are during the ice thickening period.

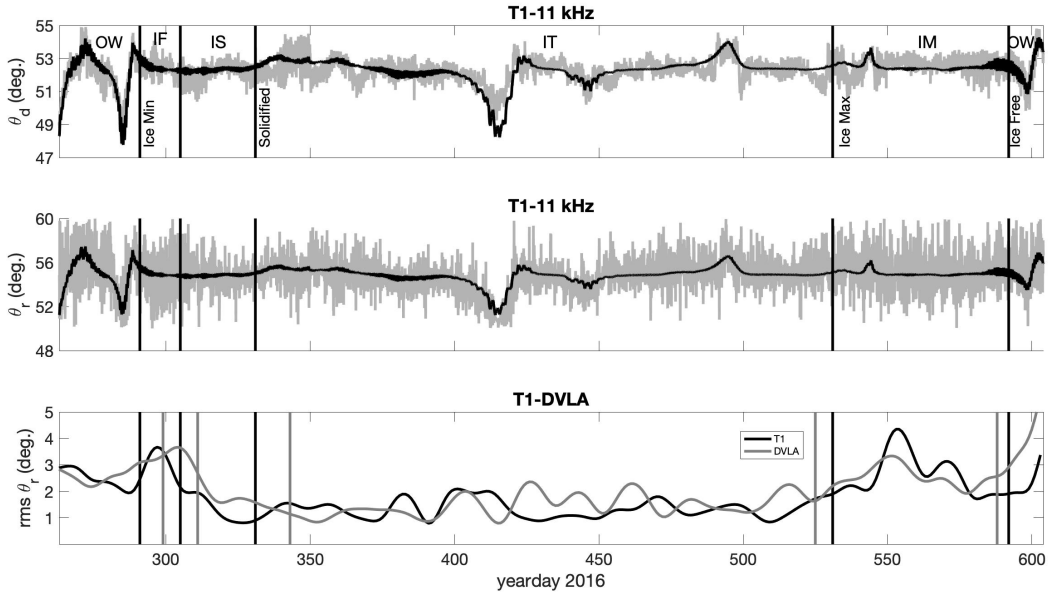

Figure 3.8: Examples of Direct Arrival Beamformer Angle (upper), reflected arrival beamformer Angle (middle) at the T1 mooring, and time series of 10-day average rms reflected angle at the T1 and DVLA mooring between 16 September 2016 (yearday 260) and 26 August 2017 (yearday 604). Gray line shows the computed beamformer angle, and the black line shows the predicted angle from mooring navigation. Black and gray vertical lines show the ice minimum, separation of ice formation and ice solidification, solidified ice, ice maximum, and ice-free periods for the T1 and DVLA, respectively. The reference hydrophone is in the center of the array, and located at depths of 120.4 and 183.6 meters at the T1 mooring and DVLA, respectively. First 30 hydrophones are processed at the DVLA mooring. The abbreviations are the same as in Fig. 3.2.

3.3.2 Moments of the Reflected Intensity

The next observables to be treated are the mean and the scintillation index, SI, of the reflected intensity, $I_{rc}(n, m, t)$ time series show fluctuations on time scales from hours to months and so we seek to interpret the slow modulation of I_{rc} as a changing mean while the fluctuations around that slowly changing mean will be interpreted in terms of SI. The scintillation index is a second moment of the intensity defined as $(< I^2 > - < I >^2)/< I >^2$ and quantifies as the name implies the degree of signal twinkling. SI is strongly impacted by signal interference, in

this case caused by reflections off of different regions of the rough ice surface. If SI is much less than 1 this implies a single dominant reflected path. For SI greater than 1 there are multiple paths causing a complex interference pattern. As the number of paths goes to infinite the Central Limit Theorem dictates that SI asymptotes to 1 [Colosi, 2016]. The slow modulation component is obtained by low pass filtering, that is

$$\overline{I}_{rc}(n,m,t) = LPF[I_{rc}(n,m,t)] \tag{3.4}$$

where the low pass cutoff frequency is 0.1 cycles per day (cpd). The fluctuations from which SI are computed are given by

$$\delta I_{rc}(n,m,t) = \frac{I_{rc}(n,m,t)}{\overline{I}_{rc}(n,m,t)}. \tag{3.5}$$

To get the mean reflected intensity, $\overline{I}_{rc}(n,m,t)$ is normalized with the yearlong time mean from each phone. This gives a relative variation over the year and removes the phone to phone variation. The mean reflected intensity is then defined as the depth-frequency average of this normalized quantity, that is

$$\hat{I}_{rc}(t) = \left\langle \left\langle \frac{\overline{I}_{rc}(n,m,t)}{\langle \overline{I}_{rc}(n,m,t)\rangle_t} \right\rangle_m \right\rangle_n \tag{3.6}$$

A depth-frequency average is used since no significant variation was observed over depth or frequency. Reflected intensity is therefore not a reflection coefficient, it just displays the relative variation of reflected intensity over the year. Figure 3.9 shows depth-frequency averaged reflected intensity as observed at the DVLA and T moorings respectively: the values do not show much variation across all the moorings. For the DVLA, the reflected intensity reaches a peak of roughly 2 under open water conditions. However, during ice formation the values decrease sharply

only to rise again during the ice solidification period. For the ice thickening epoch reflected intensity slowly decreases from a value of roughly 1.5 to 0.5. For the early part of the ice melting phase there continues to be some loss of reflected intensity reaching a minimum of 0.25, but then reflected intensity rapidly increases as the ice disappears.

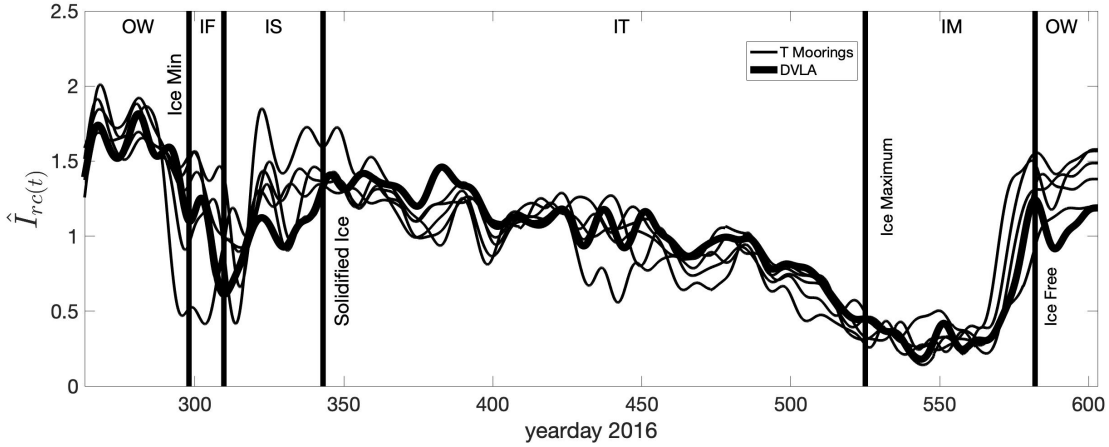

Figure 3.9: Example time series of depth-frequency averaged reflected intensity at the DVLA and T moorings between 16 September 2016 (yearday 260) and 26 August 2017 (yearday 604). Vertical lines show the ice minimum, separation of ice formation and ice solidification, solidified ice, ice maximum, and ice-free periods for the DVLA. A smoothing filter with a low pass cut off at 0.1 cph was applied to the observations. The abbreviations are the same as in Fig. 3.2.

SI also shows interesting variation throughout the different epochs. Here SI is calculated along a sliding 10-day window ($\delta t = 10$ days) using

$$SI(n, m, \hat{t}) = \left\langle \frac{\langle \delta I_{rc}^2(n, m, t) \rangle_{\delta t} - \langle \delta I_{rc}(n, m, t) \rangle_{\delta t}^2}{\langle \delta I_{rc}(n, m, t) \rangle_{\delta t}^2} \right\rangle_{\delta \hat{t}} \tag{3.7}$$

where $\hat{t}$ is the center of the time window. Figure 3.10 shows time series of depth-frequency averaged SI as observed at the DVLA and T moorings, and again frequency averaging was done because no significant frequency dependence was seen in our analysis. The figure shows no strong variation of SI is observed across

all the moorings. The highest reflected intensity (Fig. 3.9) and lowest SI, with values well below 1, were observed during open water conditions. In the early phase of ice formation, SI raises abruptly and then settles to a value near 1 during the IS and early ice thickening phases. Over ice thickening there is a slow increase in SI up to a value of 1.5. The largest values of SI are observed during the ice melting epoch and then there is a return to open water conditions with low SI.

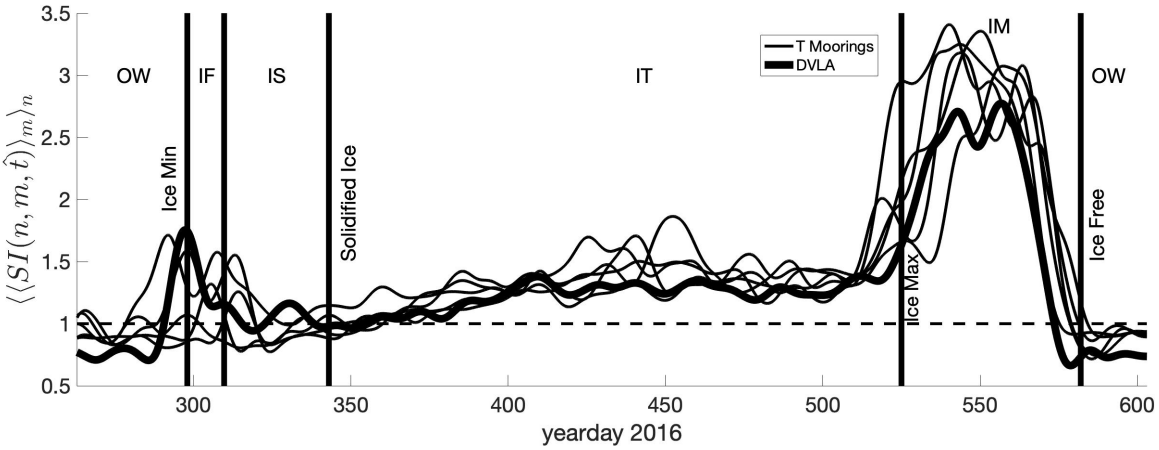

Figure 3.10: Example time series of depth-frequency averaged SI at the DVLA and T moorings between 16 September 2016 (yearday 260) and 26 August 2017 (yearday 604). Vertical lines show the ice minimum, separation of ice formation and ice solidification, solidified ice, ice maximum, and ice-free periods for the DVLA. The value of 1 is represented by the horizontal dashed line. The abbreviations are the same as in Fig. 3.2.

Unlike reflected intensity, $SI(n, m, \hat{t})$ shows a clear depth dependence. Figure 3.11 shows frequency averaged SI as a function of depth for three different ice epochs (open water, ice thickening, and ice melting). There is a clear trend towards lower scintillation at deeper depths. This effect is likely due to the depth dependence of the Fresnel zone for this geometry (Section IV) where deeper depths have a larger Fresnel zone, i.e., a larger region over which diffraction averages over the rough surface. The predicted scaling is that SI is inversely proportional to

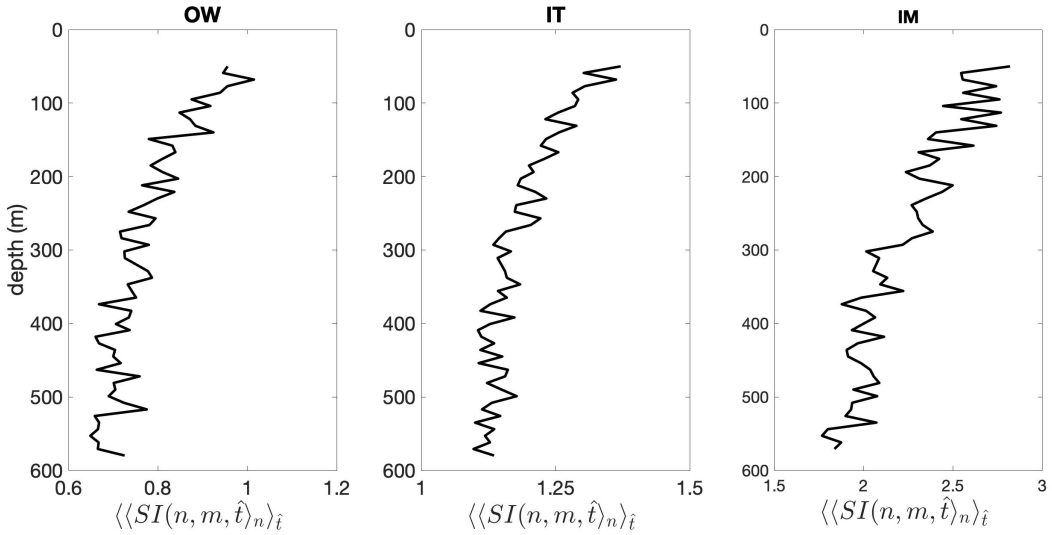

Figure 3.11: DVLA frequency averaged SI as a function of depth under the open water (left), ice thickening (middle) and ice melting epochs (right). The abbreviations are the same as in Fig. 3.2.

the Fresnel zone so the depth scaling is found to be $SI \propto z^{-1/2}$ (Section IV) which is close to what is observed.

3.3.3 PDF of the Reflected Intensity

In the previous section during all ice conditions it was found that the SI was between 1 and 2.5 implying that the propagation is in the partial and full saturation regimes. Here the PDF's of reflected intensity are examined to gain more insight into the propagation regime. Figure 3.12 shows the PDF of the $\delta I_{rc}(n,m,t)$ for the open water, ice thickening and ice melting epochs on the DVLA and T1 moorings. The observed PDFs are compared to an exponential PDF that would be expected in full saturation and a modulated exponential that would be expected in partial saturation [Colosi, 2016]. The modulated exponential

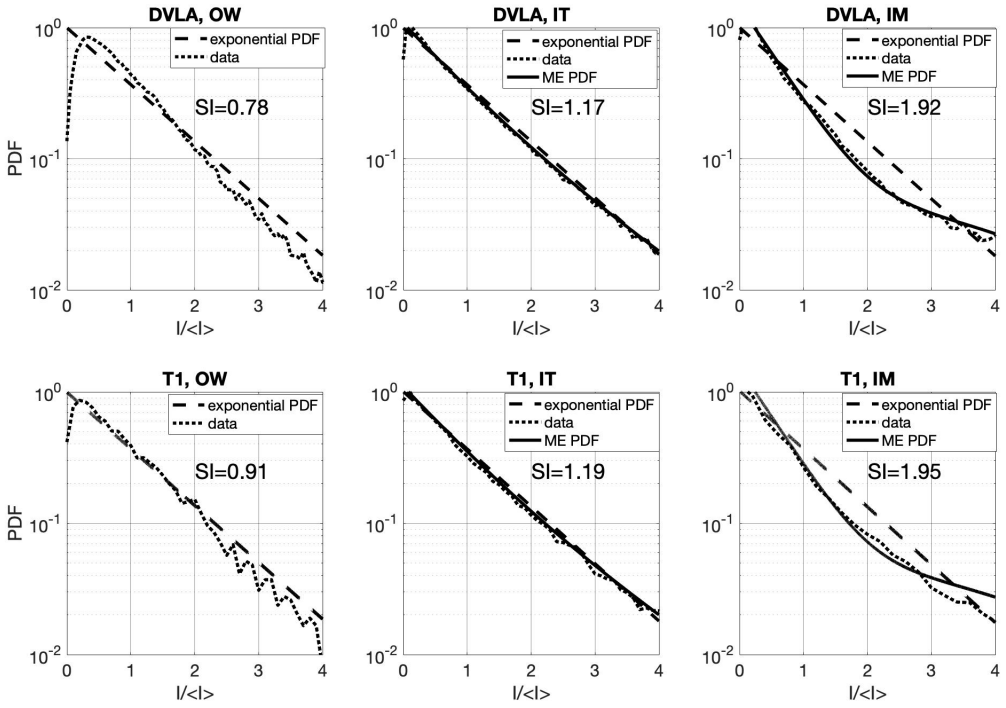

Figure 3.12: Example PDFs of the reflected intensity for 12 kHz measured during the thickening and melting ice periods at the DVLA mooring (upper panels) and at the T1 mooring (lower panels). The abbreviations are the same as in Fig. 3.2.

(ME) distribution is defined as [Colosi et al., 2001]

$$P_M(x) = P_0(x)\left[1 + \frac{b}{2}(x^2 - 4x + 2)\right] \tag{3.8}$$

where $x = I/\langle I\rangle$, SI=1+2b, $P_0(x) = \mathrm{e}^{-x}/\langle I\rangle$, and b, the modulation factor, should be less than about 0.5. There are two physical interpretations of the ME. One view holds that with a power law spectrum the small scales lead to saturated behavior ($SI = 1$) but the large scales in the rough interface modulate the interference making $SI > 1$. Another interpretation is that the modulation is a result of non-stationarity in the interface. In any case, the observed PDFs fit the ME PDF exceptionally well (b=0.09 and 0.1 for ice thickening epochs on

the DVLA and T1 moorings, respectively), even during the ice melting period (b=0.46 and 0.47 on the DVLA and T1 moorings, respectively) where SI is on the border of where the ME approximations should start to break down. For open water cases where $SI < 1$ the exponential is not a good fit, and it is estimated that the scattering regime is closer to the weak scattering case.

3.3.4 Pulse Time Spread (Time-Lagged Intensity Covariance)

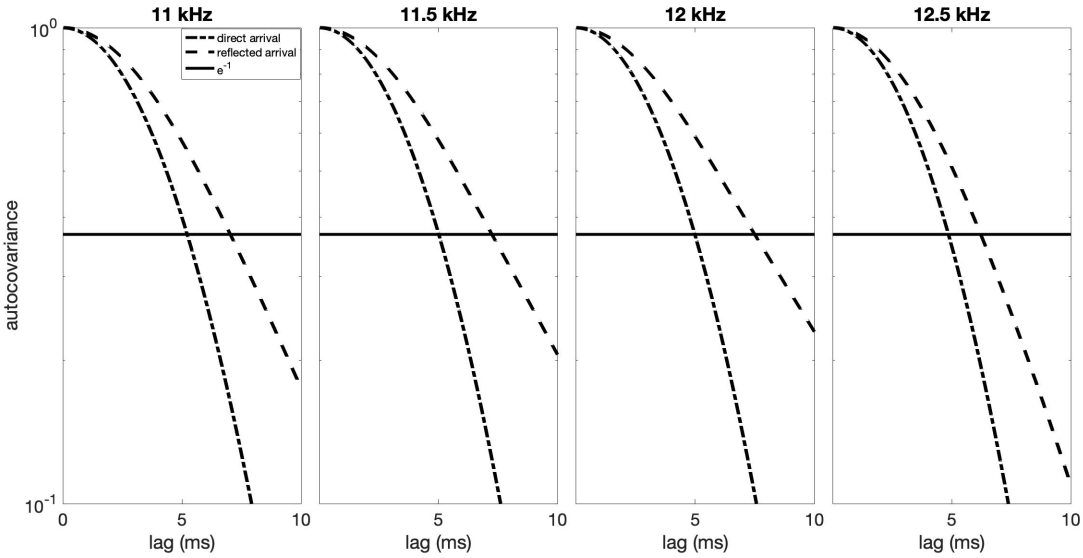

Figure 3.13: Examples of depth averaged, time-lagged intensity autocovariance at the DVLA mooring on 16 November 2016 (yearday 321). Dashed line indicates reflected arrival, dash-dot line indicates the direct arrival and solid line indicates the e^{-1}.

Pulse time spread is a statistical quantity derived from the time-lagged intensity covariance function, that can be considered physically as the inverse of the coherent bandwidth of the signal and does not depend on the signal time wander [Colosi, 2016]. In the time domain it can also be interpreted in terms of time delayed paths relative to the specular path that become ensonified by the effects

of the rough surface. Figure 3.13 shows time-lagged intensity covariance for both the direct and the reflected paths on yearday 321. Like the SI, an intensity covariance function is computed and then averaged over depth, frequency and some geophysical time window, δt, to produce a time spread estimate that is a function of time of the year. The calculation is done as follows

$$\langle II(\delta\tau)\rangle(\hat{t}) = \Big\langle \Big\langle \Big\langle \langle I_r(n,m,\tau,t)\ I_r(n,m,\tau+\delta\tau,t)\rangle_\tau \Big\rangle_{\delta t} \Big\rangle_m \Big\rangle_n \tag{3.9}$$

where the covariance is normalized by the zero lag value. Time-lagged intensity covariance for the reflected path is observed to be larger than the direct path during the entire year, as shown in Fig. 3.13. To get a time spread estimate, a Gaussian model is utilized [Colosi, 2016] of the form

$$\langle II(\delta\tau)\rangle = \frac{1}{2}\left[\exp\left(-\frac{\delta\tau^2}{2\alpha^2}\right) + \exp\left(-\frac{\delta\tau^2}{2\alpha^2+4\tau_0^2}\right)\right]. \tag{3.10}$$

where α is the time width of the unperturbed pulse and τ_0 is the time spread. The first term in this equation is simply the intensity covariance of the unperturbed signal, and the second term generates the time spread. The observations from Eq. 3.9 were used to estimate the unperturbed pulse time width α and the scattering induced time spread τ_0 (Eq. 3.10). This is done in a two-step process. First, by forming the intensity covariance of the direct arrival (Eq. 3.9, but now the τ values are limited to ones where there is direct path energy), α can be estimated by finding the e-folding scale. Knowing α, the observed intensity covariance from the reflected arrival can now be fit with Eq. 3.10 for the one unknown τ_0.

Figure 3.14 shows a time series of depth-frequency averaged pulse time spread, which is τ_0 / α, as observed at the DVLA and T moorings. To demonstrate the depth-dependency in the pulse spread, upper and lower DVLA HMs were analyzed

independently. The spread appears to be greater at lower depths. This impact is most likely due to larger Fresnel zone at the deeper depths where a wider region is available further away from the specular point (Section IV). Seasonal differences in pulse spread are seen in relation to open water and different epochs of ice evolution. As compared to other epochs, time spread is comparatively higher during ice formation and then declines significantly to about 0.12 once the ice solidification phase is reached where there is a smoother, more homogeneous surface. Spread increases slightly during the ice thickening phase and reaches 0.2 as the ice melts. It returns the open water values when the ice has almost disappeared.

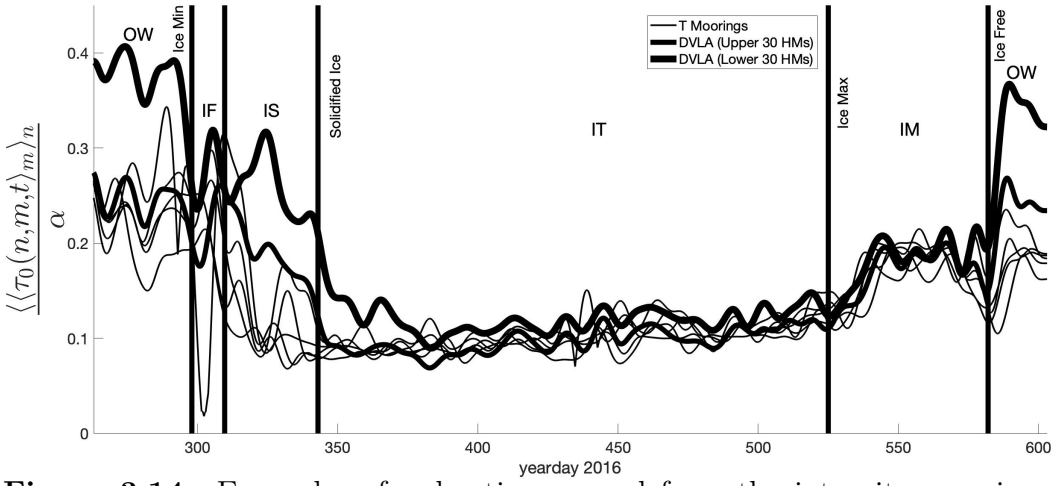

Figure 3.14: Examples of pulse time spread from the intensity covariance at the DVLA and T moorings between 16 September 2016 (yearday 260) and 26 August 2017 (yearday 604). Vertical lines show the ice minimum, separation of ice formation and ice solidification, solidified ice, ice maximum, and ice-free periods for the DVLA. Spread values are low-pass filtered as in Fig. 3.9. The abbreviations are the same as in Fig. 3.2.

3.4 DISCUSSION

Absent a precise ice scattering model, which will be the focus of future work, the goal of this section is to put the observations of rms arrival angle, reflected intensity, SI, and pulse spread into a conceptual physical context associated with various phases of the annual ice development. This can be accomplished using simple models existing in the literature. But before that is done some acoustical concepts will be covered for use in the subsequent discussion.

3.4.1 Existing forward scattering models

The geometry of the scattering problem is shown in Fig. 3.1. The source is at position $(0, 0, -D)$ and the receiver is at $(R, 0, -Z)$. The specular point is located at $(x_r, 0, 0)$, and the rough surface is located at $(x, y, h(x, y))$. The specular point is given by $x_r = RD/(D + Z)$, and gives a total distance traveled by the surface interacting path as $L_r = r_1 + r_2$, where $r_1 = \sqrt{x_r^2 + D^2}$, and $r_2 = \sqrt{(R - x_r)^2 + Z^2}$.

The received field is due to contributions from the entire rough surface. However, significant contributions arise only from the Fresnel zone, which is an ellipse with principle radii in the x and y directions, as discussed by [Yang et al., 1992]

$$R_{fx} = \left[\frac{\lambda Z}{\sin^3\theta}\left(1 - \frac{Z}{D}\right)\right]^{1/2} \tag{3.11}$$

$$R_{fy} = \left[\frac{\lambda Z}{\sin\theta}\left(1 - \frac{Z}{D}\right)\right]^{1/2} \tag{3.12}$$

where $\theta = \sin^{-1}(D/\sqrt{R^2 + D^2})$ is the the approximate grazing angle of the specular ray. These radii result from a quadratic expansion of the path length around the specular point [Clay and Medwin, 1977, Yang and McDaniel, 1991,

Yang et al., 1992]. Here it is seen that $R_{fx} > R_{fy}$ and that the Fresnel ellipse increases for increasing Z and λ and decreasing θ. $R_{fx} \simeq 1.4 R_{fy}$ for the CANAPE geometry, where R_{fy} is between 3 and 10 meters.

In a summary of the findings of theoretical treatments of rough surface scattering, [Thorsos, 1984a] found that the effect of roughness on forward scatter when the incident pulse length is long and beamwidths of the transmitter and receiver are wide, was that there is essentially no alteration of the received intensity compared with the flat interface case. This was interpreted as a consequence of energy conservation, and the fact that long pulses and wide or near omnidirectional beams cannot resolve any broadening of the scattered pulse or change of received angle. It may also be a consequence of using the quadratic expansion of the path length in the Fresnel approximation.

In the present case, short pulses were used to interrogate the rough surface, although the beamwidths of each transducer were still rather wide. With short pulses, one can observe a broadening of the received signal due to the acoustic field scattered from different parts of the Fresnel zone, which was noted in the section on pulse time spreads above. The more diffuse the scattered field, the more spreading is observed. The further from the specular point, the larger the time delay and thus more spread. The rms angle from the incoherent beamformer should be linked to this increased time spread, which is explored later in the discussion. In the literature on wave propagation in random media, pulse time spread depends on the cross frequency coherence function [Colosi, 2016], and in fact the time spread parameter α can be related to the reciprocal of the signal coherent bandwidth. This interpretation may be related to the geometric interpretation presented above, but requires more theoretical work to connect the two.

In [Thorsos, 1984a] the high-frequency limit of the Kirchhoff approximation is

used to model the ensemble average pulse for forward scattering geometries. Here the model is slightly modified to include a boundary condition appropriate for the water-ice interface by including the plane wave reflection coefficient, R, evaluated at the specular point. This simple multiplication by the reflection coefficient is the result of the high-frequency Kirchhoff approximation applied to penetrable surfaces, as shown in Ch. 13 and Appendix L of [Jackson and Richardson, 2007a]. Ambiguities between material properties and roughness exist for ice as well as seafloor acoustic remote sensing applications. The modified version with adjustments in notation is,

$$\langle I_s(\tau)\rangle = \frac{I_t A_0 |R|^2}{(r_1+r_2)^2} \begin{cases} 0 & \text{if } \tau < 0 \\ \text{erf}[\sqrt{\tau/\tau_0}] & \text{if } 0 \leq \tau < \alpha \\ \text{erf}[\sqrt{\tau/\tau_0}] - \text{erf}[\sqrt{(\tau-\alpha)/\tau_0}] & \text{if } \tau >\geq \alpha \end{cases} \tag{3.13}$$

where $\tau = t - t_s$ is the time delay from the specular time, α is the unperturbed pulse length (similar to the intensity covariance) and erf$[z]$ is the error function [Abramowitz and Stegun, 1972]. The parameter A_0 is an area factor, which we take to be the Fresnel zone area, and I_t is the transmitted intensity at 1 meter. The parameter τ_0 is an elongation time or time spread that is due to the scattered field arriving from different places on the rough surface. Equation 3.13 does not take into account time wander due to changing receiver locations, or variations in the mean water-ice interface over the scale of a Fresnel zone. In the present analysis the intensity covariance was used because it is insensitive to wander (Sec 3D). Be that as it may, [Thorsos, 1984a] defines the time spread parameter τ_0 in terms of the geometry and root-mean squared slope as

$$\tau_0 = \left[\frac{2r_1 r_2}{r_1 + r_2}\frac{\tan^2\gamma_0}{c}\right]\left[1 - e^{-\theta/\gamma_0}\right] \tag{3.14}$$

where $\tan\gamma_0$ is the rms slope of the rough interface, and γ_0 is the rms slope expressed as an angle in radians. It should be noted again that the high-frequency limit of the Kirchhoff approximation was used to obtain Equation 3.14.

Coherent reflection can also be taken into account in this model, but is likely absent in these measurements. The coherent reflection coefficient is parameterized by the Rayleigh factor,

$$\Phi = 2k_0\langle h^2\rangle^{1/2}\sin\theta \tag{3.15}$$

and is given by $\exp(-\Phi^2/2)$. For the high frequencies used in this work, Φ varies between 7 and 70 radians, corresponding to rms height of the ice interface of 0.1 to 1.0 m. Therefore, the exponential is extremely small, and coherent reflection is unimportant in this experiment.

In the model detailed above, several parameters of the rough surface and geometry affect the observables studied in this work. Ambiguities between material properties and roughness exist for ice as well as seafloor acoustic remote sensing applications [Jackson and Richardson, 2007a]. First, the water-ice reflection coefficient, R, directly impacts the received intensity, as I is proportional to $|R|^2$. This quantity is studied in the next subsection. Second, the rough interface does not change the peak intensity, only the pulse elongation through the rms slope, γ_0. Therefore, in this model, the trends in the reflected intensity can be attributed only to the changing material properties of the ice, not the roughness. The effects

of time spreads can be attributed solely to the changing rms roughness within the Fresnel zone and not material properties. It is this separation of the effects of material properties and ice roughness that makes remote sensing of each parameter plausible.

However, there are limitations to the scattering model used here. Ice roughness often has an exponential roughness covariance function, which has a power-law wave number spectrum [Wadhams, 2012, Gavrilov and Mikhalevsky, 2006a]. This type of multiscale surface is often poorly modeled by the standard Kirchhoff approximation [Thorsos, 1990b], with larger errors likely for the high-frequency limit. Therefore, at this time, it is not possible to perform remote sensing of ice roughness using pulse spreads, since a more appropriate model would need to be developed. However, since the reflected intensity is proportional to $|R|^2$ in both the standard and high-frequency Kirchhoff models, remote sensing of ice properties shows more promise, and some detailed modeling is performed in the next section that shows a good match with the data.

Similar limitations exist with existing models for the the scintillation index, which is a fourth moment of pressure. Assuming that the material properties of the ice are locally temporally stationary over the averaging window and spatially homogeneous over the Fresnel zone, the intensity fluctuations may be viewed as solely a function of the experiment geometry and interface roughness. Work by [Yang and McDaniel, 1991] and [Yang et al., 1992] could be used to link the scintillation index to the roughness covariance function and the Fresnel radius. Key ideas from these two references may have an impact on any quantitative remote sensing technique using the scintillation index.

These two models for SI involve a double spatial integral over an exponential of the phase structure function, which is related to the roughness structure

function. Here, a dimensionless number Λ takes into account the relationship between the Fresnel radius, roughness correlation scale, and wave number, as in $\Lambda \propto R_f/(kL_f^2)$, and is also used in [Colosi, 2016] for medium fluctuations. When Λ is small, significant correlation exists between contributions from points within the Fresnel zone and can drive the SI to unity (saturation regime), or even greater than unity [Yang et al., 1992, Colosi, 2016]. For small values of Λ, as the mean square phase, Φ, increases, the scintillation index increases from zero to slightly larger than unity and then falls back to unity as $\Phi \to \infty$. A small value of Λ is likely for this experiment, as the Fresnel radius varies between 3 and 14 m, and the ice roughness correlation length (excluding keels) range between 15 and 75 m [Gavrilov and Mikhalevsky, 2006a]. The integrals presented in [Yang et al., 1992] are complicated, and specialized techniques were developed for the Gaussian roughness covariance. For more realistic covariance functions, different integration methods must be developed, which is an opportunity for future research. Even given these limitations of the models of [Yang and McDaniel, 1991, Yang et al., 1992], the overall trends in terms of the dimensionless parameters Λ and Φ hold, and are used for power-law fluctuations in [Colosi, 2016].

3.4.2 Elastic Layer Reflection Coefficient

For simplicity, the reflection coefficient is treated here using a flat three-layer system composed of a liquid ocean half-space, an elastic ice layer, and an air half space [Morozov and Colosi, 2017, Brekhovskikh, 1960]. This is called the Elastic Layer Reflection Coefficient (ELRC) model, and it is described enough in the literature that the material is not repeated here. The key ice parameters are the thickness, H, the density, ρ, the p-wave

and s-wave speeds, c_p and c_s, and their attenuation factors, α_p and α_s [Hobæk and Sagen, 2016]. From measurements reported in the previous literature [Kuperman and Schmidt, 1986, Yang and Giellis, 1994, Jensen et al., 2011, McCammon and McDaniel, 1985, Gavrilov and Mikhalevsky, 2006a], historical p-wave speed and attenuation values range from 3000-3600 m/s and 0.07-0.76 dB/λ respectively [Hobæk and Sagen, 2016, Alexander et al., 2012]. For shear wave speed and attenuation, the range is 1500-1800 m/s and 0.05-2.5 dB/λ. With the near disappearance of multiyear ice, conditions are expected to have changed considerably since these earlier measurements based on ice-floe's history and the temperature and salinity of the ocean water at the time the ice was formed [Hope et al., 2017]. Recently, [Duda et al., 2021] used $c_p = 2500$ m/s, $c_s = 1200$ m/s, $\alpha_p = 0.07$ dB/λ, $\alpha_s = 0.25$ dB/λ, and $\rho_{ice} = 910$ kg/m^3 to model the first year ice. The sound speed of the water is taken as $c = 1430$ m/s, and density is $\rho = 1020$ kg/m^3. For air the values are $c = 340$ m/s and $\rho = 1.0$ kg/m^3.

The CANAPE observations show that the statistics of the ice-scattered acoustic fields change considerably over the seasonal evolution of the ice, and so one set of ice values for the whole year is not a realistic model. Seasonally changing ice properties are therefore considered relative to various epochs of the ice evolution. The first phase is ice formation, when there can be a slushy water/ice mixture, pancake ice, and dendritic ice formations. During this phase, one would expect low shear speeds, p-wave speeds between water and solid ice and high p-wave attenuation due to the porosity of the ice/water mixture and the dendrites. The second phase, ice solidification, sees a gradual trend towards solid ice properties like those described by [Duda et al., 2021]. The third and longest phase ice thickening conceivably only has two parameters that change, namely the ice thickness H and roughness. The temperature and salinity structure of the ice varies

over the year, also resulting in changes in wave speeds [Laible and Rajan, 1996], but ice porosity and thickness are reported to have a greater impact on the acoustic properties than salinity and temperature variation within the ice [McCammon and McDaniel, 1985, Alexander et al., 2013, Yew and Weng, 1987]. The last phase ice melting is where H is diminishing rapidly, there are melt ponds and ice leads, and more slushy ice/water mixtures are expected. This period is expected to have a drop in p-wave and s-wave speeds and an increase in p-wave attenuation much like in ice formation.

3.4.3 Interpretation

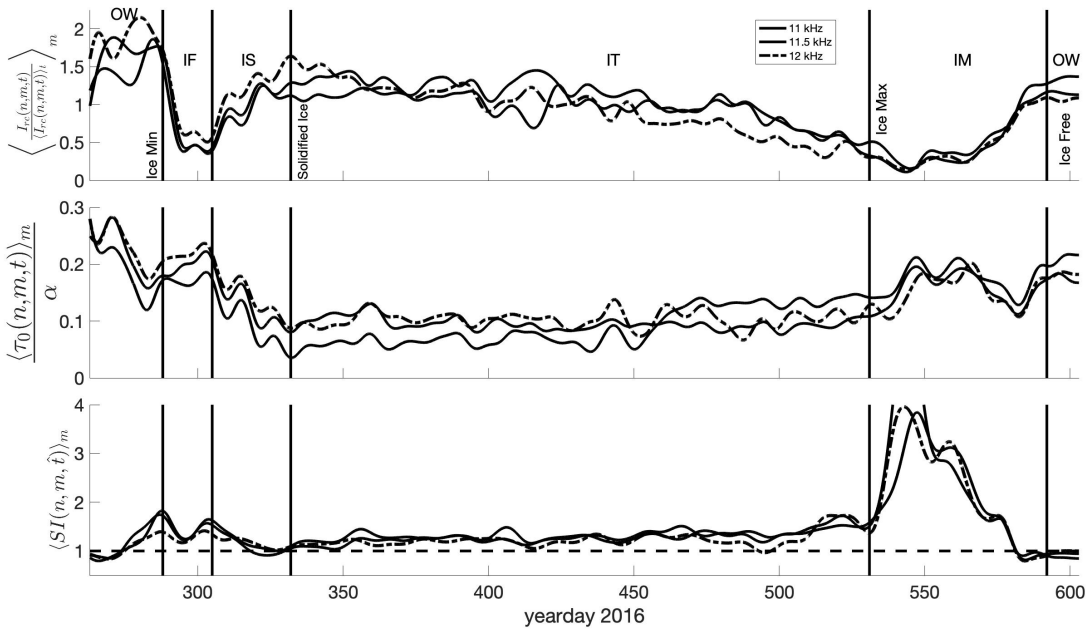

Figure 3.15: Comparisons of depth-averaged reflected intensity (top), pulse time spread from the intensity covariance (middle), and depth-averaged SI (bottom) for the T1 mooring between 16 September 2016 (yearday 260) and 26 August 2017 (yearday 604). Vertical lines show the ice minimum, separation of ice formation and ice solidification, solidified ice, ice maximum, and ice-free periods for the DVLA. The value of 1 is represented by the horizontal dashed line. The abbreviations are the same as in Fig. 3.2.

The ideas developed above are now used to qualitatively describe the possible processes driving the variability of the acoustic field statistics. Figure 3.15 shows the seasonal evolution of reflected intensity, pulse time spread and SI observed at mooring T1. The reader should also consider the evolution of rms receiver angle (Fig. 3.8) which is an indicator of the angular spread of the scattering. The four epochs of ice formation, ice solidification, ice thickening, and ice melting are marked on the figure. Figure 3.16 shows the seasonal evolution of three quantities: 1) ice thickness, H, 2) the square of ELRC (comparable to reflected intensity in Fig. 3.15) , and 3.3) the ice parameters, c_p, c_s, α_p and α_s; ice density is assumed constant at 910 kg/m^3. The ice parameters used in the ELRC model are listed in Table I.

Table 3.1: Geoacoustic Parameters of Arctic ice used in the ELRC model.

	Ice Formation	Ice Solidification	Ice Thickening	Ice Melting
C_p	2300 m/s[1]	2300-2500 m/s	2500 m/s	2500-2300 m/s
C_s	1200 m/s	1200-1300 m/s	1300 m/s	1300-1200 m/s
α_p	0.3 dB/λ	0.3-0.07 dB/λ	0.07 dB/λ	0.07-0.3 dB/λ
α_s	0.25 dB/λ	0.25 dB/λ	0.25 dB/λ	0.25 dB/λ
ρ_{ice}	910 kg m^{-3}	910 kg m^{-3}	910 kg m^{-3}	910 kg m^{-3}
θ_{gr} [2]	50-55	50-55	50-55	50-55

During the ice formation phase, reflected intensity is seen to diminish rapidly, spread slightly increases, and the SI is elevated relative to the pre-ice phase. The drop in the reflected intensity is attributed to the elevated p-wave loss due to the slushy ice/water mixture and in the ELRC calculation this behavior is mimicked qualitatively (Fig. 3.16). This hypothesis can be supported by previous studies, such as [Williams et al., 1992], which found that p-wave loss in ice is maximum within the skeletal layer. The p-wave critical angle is also likely to be a factor in decreases in reflected intensity. It is found to be equal to 51.55° for C_w=1430 m/s and C_p=2300 m/s. The spread and scintillation index results could be attributed

to rough surface effects. Because the roughness is weak during this period, the increasing spread is potentially due to the increased number of scattered paths away from the specular point. This hypothesis is supported by the slight increase in rms angle during this period (Fig. 3.8). Similarly SI is elevated by a factor of 2 due to more interference from scattered paths.

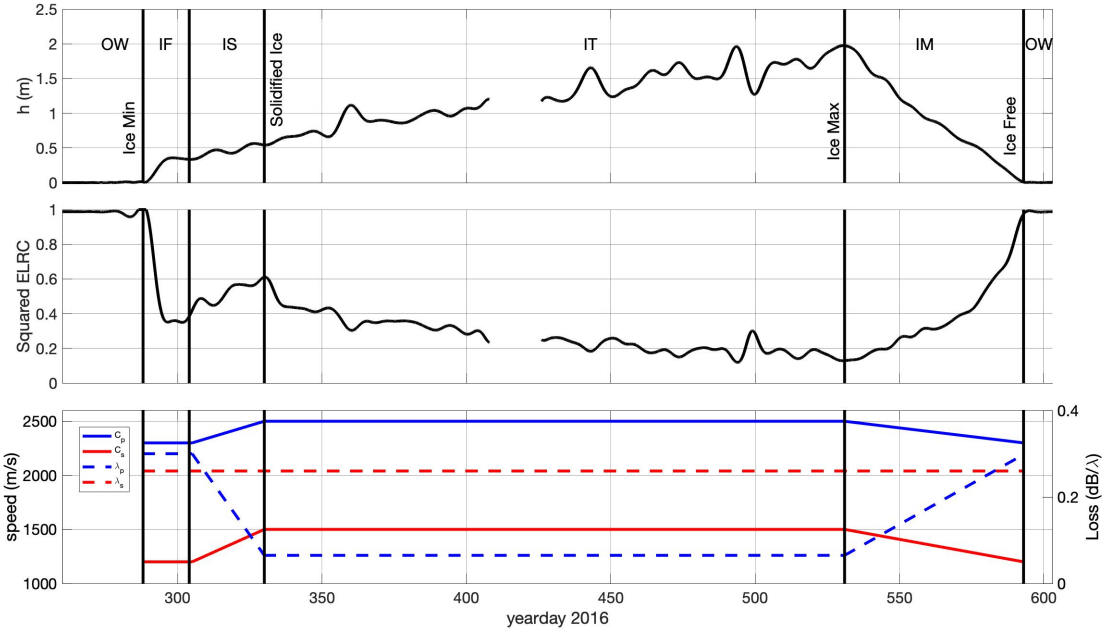

Figure 3.16: Ice thickness (top), squared ELRC model from a flat surface at grazing angle ranging from 50° to 55° for 11 kHz (middle) with changing ice parameters (bottom). Vertical lines show the ice minimum, separation of ice formation and ice solidification, solidified ice, ice maximum, and ice-free periods for the T1. Ice thickness and ELRC values are low-pass filtered as in Fig. 3.9. The abbreviations are the same as in Fig. 3.2.

At the start of the ice solidification phase, there is a notable inflection point for all three observables. Reflected intensity is seen to increase rapidly as the ice firms up. The hypothesis is that this increase is due to the reduction of the p-wave attenuation. Here, loss due to shear wave production is likely not significant since the ice is still thin and solidifying. Again the ELRC captures this increase adequately (Fig. 3.16). The model yields a decent performance in this epoch when

C_s=1200 m/s, however, C_s is assumed to increase from 1200 to 1300 m/s and C_p is expected to increase from 2300 to 2500 m/s during this phase due to improve the correlation between model results and observed reflected intensity. The formation of colder, less porous ice might be responsible for the rise in both C_s and C_p during this phase. Spread and SI are both dropping considerably. During the solidification process the roughness is expected to increase, but a reduction is seen in rms arrival angle (Fig. 3.8). The reduction in rms angle is consistent with the reduction in time spread as these variable angles could be associated with paths away from specular. A full-year time series of 10-day average rms reflected angle and spread with a sliding window of 1-day were evaluated using linear regression analysis to assess the relationship between them. In line with our predictions, the spread was positively related to the rms reflected angle with Rsq = 0.68, 0.66 and 0.57 for 12 kHz, 11.5 kHz and 11 kHz, respectively. For the SI there is a trend towards 1, and because the PDFs are close to exponential (Fig. 3.12), the acoustic fields are apparently tending toward saturation. Saturation could occur due to the increased ice roughness leading to more scattered paths, but those scattered paths would have to be close enough to the specular path so that they would not contribute to the time spread.

When the ice thickening phase begins, there is again an inflection point. Reflected intensity is seen to slowly diminish, while spread and SI slowly increase. The slow decrease in reflected intensity is likely due to the slow thickening of the ice and therefore increasing coupling into the ice shear waves (Fig. 3.15) and attenuation that the wave experiences when it propagates through the ice layer and back. There is also likely some decrease in reflected intensity due to the increasing ice roughness and ice keels. The reflected intensity starts at a value of about 1.5 and reaches a minimum shortly after the ice maximum of about 0.15.

This pattern is mimicked in the computed reflection coefficient with no roughness contribution (Fig. 3.16). Interestingly the time spread is rather insensitive to the thickening and evolution of the ice over this phase, and the low values are again strongly correlated with the low rms angle values (Fig. 3.3) (r=0.75) and partially correlated with percentage of ice keels during the ice thickening epoch (Fig. 3.6) (r=0.44). Lossy out-of plane scattering and high angle scattering are possibly caused by ice keels during this epoch [Ballard, 2019, Simon et al., 2018]. Apparently the time delayed paths that give rise to spread remain attenuated in energy over this time. The SI, on the other hand, shows a significant increase over the ice growth phase with a trend away from full saturation ($SI = 1$) to more partial saturation where correlated paths are constructively interfering to give high intensity glints. Again, because the spread is small, these paths contributing to the scintillation must be close to the specular point. The rise in SI could also mean there is more ice roughness non-stationarity since the PDFs match the modulated exponential fairly well. In this analysis, we cannot discriminate between partial saturation behavior and non-stationarity.

The last epoch is the ice melting phase which for reflected intensity and spread show a gradual rebound to open water conditions mostly tracking the diminishing ice thickness (Figs. 3.15 and 3.16). The reflected intensity continues to decrease as the ice melts in the early part of the ice melting phase. This decrease can be attributed to the decline in p-wave and s-wave speeds and rise in p-wave attenuation due to the melt ponds and slushy ice/water combinations, but it may also be related to brine channel melting and ice becoming more porous owing to warm water entering underneath the ice [Jackson, 1994]. The behavior of SI is much more interesting. Shortly after the ice maximum the SI rises abruptly to a strong peak of 3.5 to 4.5, corresponding roughly to the minimum in the reflected

intensity. From this maximum, the SI then declines steadily to the open water conditions. The cause of these high values of SI is unknown, but it is hypothesized that keels, leads and melt ponds may play an important role such that the signals are seeing a combination of ice and open water conditions (Fig. 3.6).

3.5 SUMMARY AND CONCLUSIONS

In this work, sea ice scattering statistics of 11 to 12.5 kHz acoustic transmissions in the Beaufort Sea region of the Arctic Ocean are quantified over an annual cycle, and five significant surface scattering epochs are defined by shifts in the rms arrival angle, reflected intensity, spread, and SI. Observations show apparent changes in the quantities with varying time scales in each epoch. The reflected intensity is highest during the open water period and lowest during the early ice melting period. It varies significantly during the ice formation, ice solidification, and ice melting epochs but steadily decreases during the ice thickening epoch. Unlike the reflected intensity, SI is lowest during the open water period, with values slightly below 1, and highest during the early ice melting period. Again, SI varies dramatically during the ice formation, ice solidification, and ice melting epochs. It increases rapidly before settling to a value near 1 during the ice solidification and gradually evolved to a value of 1.5 in the later part of the ice thickening phase. SI and spread, unlike the reflected intensity, are observed to be both time and depth-dependent.

While increased roughness results in a longer time delay under the Gaussian surface layer, the spread is found to be relatively lower under the ice thickening than the ice formation and ice solidification. The hypothesis here is that two different mechanisms may have been responsible for the observed variations in the spread. First, increasing square rms phase and decreasing the isotropic correlation length reduce the contributions to the mean square pressure by driving the structure function's exponential to zero. Second, increased roughness and ice keels lead to out-of plane scattering and high angle scattering, causing less energy to be scattered in the direction of the receiver. The lower values in the rms angle during the ice thickening phase support this hypothesis as only the area near the

specular point may scatter the rays into the receiver. What to conclude from the pulse spread in changing ice conditions remains an open question.

The ELRC model is used to estimate ice parameters, including p-wave and s-wave attenuations and speeds and describe the possible processes controlling these variations qualitatively. There are two minimums in the Elastic Layer Reflection Coefficient (ELRC): one in the ice formation and one in the ice melting. The elevated p-wave loss caused by the slushy ice/water mixture may be responsible for the decreases during the ice formation and ice melting. The results of the two processes in squared ELRC are similar to the fluctuations observed in the data (r=0.78). The reflected intensity is seen to increase rapidly as the ice solidifies. The present analysis suggests that the observed rise in the reflected intensity is caused by the reduction of the p-wave attenuation and increase in p-wave and s-wave speeds. The reflected intensity decreases steadily as the ice thickness increases. During the ice melting, melt ponds and slushy ice/water mixtures are predicted to raise p-wave attenuation and decrease p-wave and s-wave speeds.

In summary, sea ice scattering statistics in the Arctic Ocean were quantified in this study with the aim of using this knowledge to monitor the ice properties. Five distinct ice epochs were defined, and ice parameters were predicted as a function of time for each epoch. The conclusion is that the observed changes in the reflected intensity result from a combination of processes involving the ice composition, thickness, and roughness and ice keels at the ice/water interface. Future study will focus on developing a physics-based quantitative model that links scattering statistics to specific ice and surface characteristics. The experimental arrangement needs to be improved to make the results less prone to error. Namely, better broadband sources using coded signals would reduce the inter transponder interference and allow the more frequent transmission to examine temporal statis-

tics. Furthermore, appropriate receivers designed to record mid-to high-frequency signals is necessary to quantify the signals' vertical statistics. These advancements in modeling/theory and observational capability will be prerequisite to fulling the promise for acoustically observing changing ice conditions across the Arctic.

Acknowledgments

This research was supported by the Office of Naval Research (ONR) and the author, Murat Kucukosmanoglu was supported by an ONR Ocean Acoustics Graduate Student Fellowship under Award Number N00014-19-1-2203. The IPS ice draft measurements were funded by the ONR Arctic and Global Prediction Program (ONR 322AG) under Award Number N00014-15-1-2782 to the Woods Hole Oceanographic Institution. This material is based on work supported by the ONR under Award Number N00014-15-2068 to the Scripps Institution of Oceanography. We acknowledge Richard Krishfield and Andrey Proshutinsky of Woods Hole Oceanographic Institution for generously providing essential IPS ice draft measurements. Any opinions, findings, and conclusions or recommendations expressed in this publication are those of the authors and do not necessarily reflect the views of the ONR.

APPENDIX: Derivation of the Angular Dependent Time Delay

The angular dependent time delay between the reference hydrophone and other hydrophones, $\delta\tau(m, \theta_b)$, is explained here (Fig. 3.17). The output of the beamformer for both the reflected and direct arrivals is defined as

$$I_{beam}(n, \theta_b, \tau, t) = \frac{1}{N} \sum_{m=1}^{N} I_{d,r}(n, m, \tau + \delta\tau(m, \theta_b), t) L_{d,r}^2(n, m, t) \tag{3.1}$$

where N is the number of total hydrophones, $\delta\tau(m, \theta_b)$ is the angular dependent time delay, $L_{d,r}$ is the direct and reflected path distance, and θ_b is the bearing angle. The arrival angle $\theta_{d,r}(n, t)$ relative to the mooring is then determined by the maximum of $I_{beam}(n, \theta_b, \tau, t)$ for each n and t (Fig. 3.4). Lastly, $\theta_{d,r}(n, t)$ is corrected for the mooring tilt.

It is assumed that acoustic waves are propagating along the array with the sound speed at the reference hydrophone c_0. Using the reference hydrophone location $\vec{r}_{m_r}(t)$ and other hydrophone location $\vec{r}_m(t)$, the distance and angle between the hydrophones are given by

$$R_i(m, t) = \sqrt{(\vec{r}_m(t) - \vec{r}_{m_r}(t))^2} \tag{3.2}$$

$$\tan(\theta_i(m, t)) = \frac{z_m(t) - z_{m_r}(t)}{r_m(t) - r_{m_r}(t)} \tag{3.3}$$

where $r_m(t) = (x_m(t), y_m(t))$ and $r_{m_r}(t) = (x_{m_r}(t), y_{m_r}(t))$. The direction of propagation is perpendicular to the wave front, and the distance between same wave fronts on the different hydrophones, l_i, can be used to compute the time delay by $\delta\tau(m, \theta_b) = l_i(m, \theta_b)/c_0(m_r, t)$. Writing $l_i(m, \theta_b) = R_i(m, t)\cos(\theta_i - \theta_b)$, it

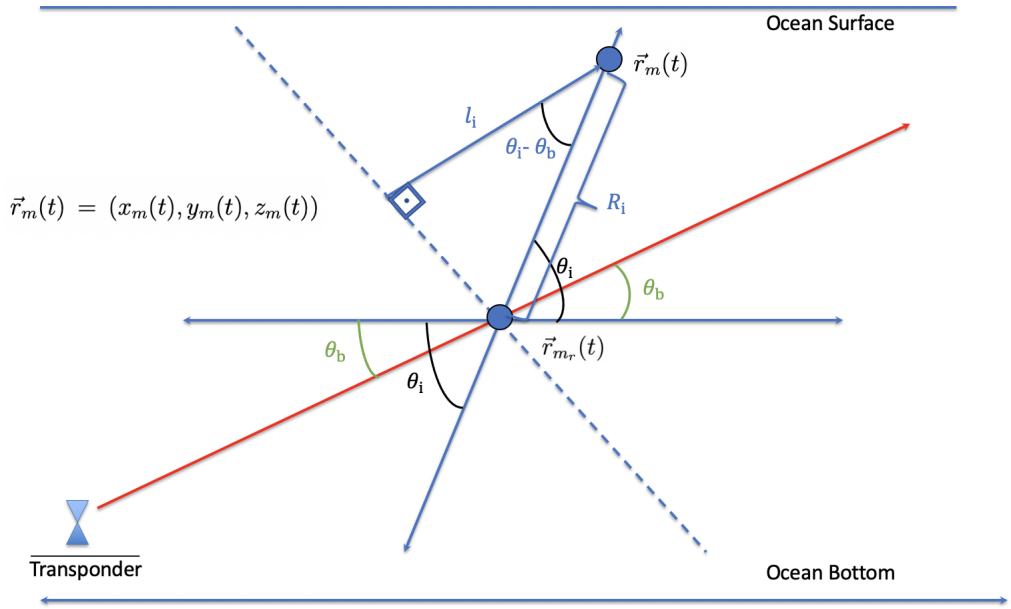

Figure 3.17: Illustration of angular dependent time delay for the direct path (no refraction). The lower blue circle represents the reference hydrophone, and the upper blue circle represents another hydrophone along the array. Blue dashed line indicates the direct path's wave front, and the solid red line indicates the direction of the propagation.

can further be written as

$$\delta\tau(m, \theta_b) = \frac{R_i(m,t)\cos(\theta_i(m_r,t) - \theta_b)}{c_0(m_r,t)}. \tag{3.4}$$

Fig. 3.18 shows the beamformer output of the reflected path for the yearday 510.

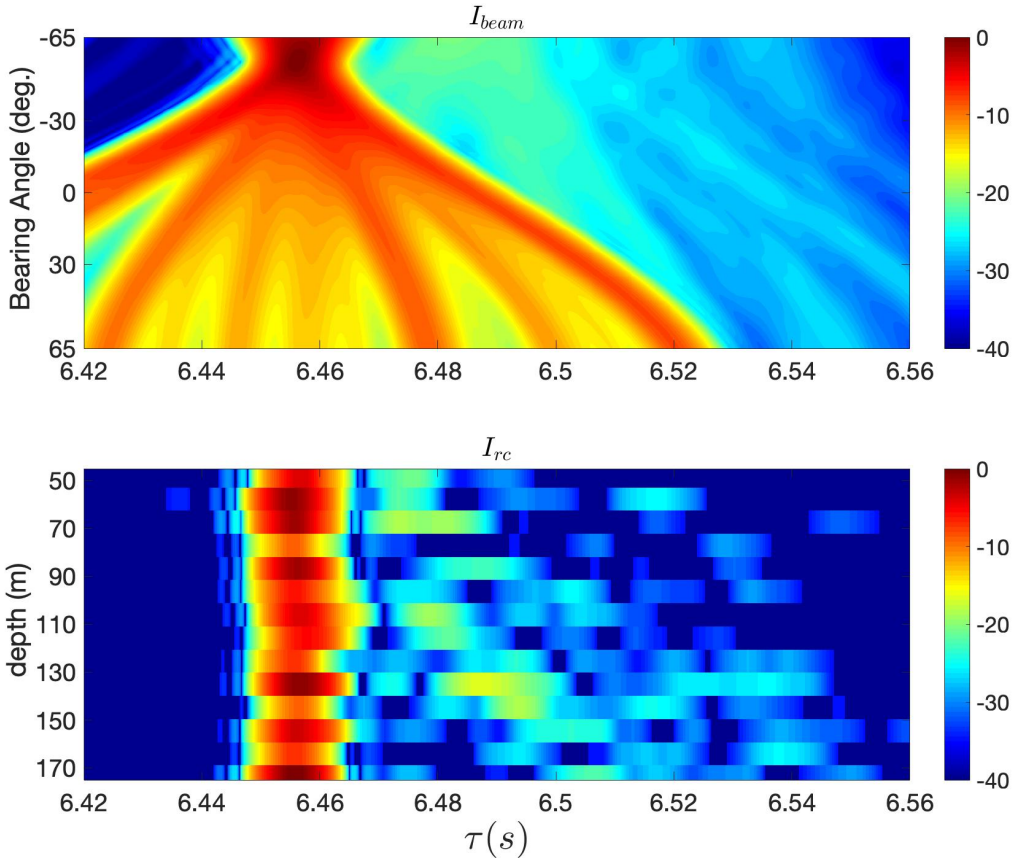

Figure 3.18: Upper panel shows the incoherent beamforming output of the reflected path for the bearing angles between -65° and +65° at 11 kHz, and lower panel shows the time front of the straightened arrivals at T1 mooring on 24 May 2017 (yearday 510).

Chapter 4

Observations of the space/time scales of Beaufort Sea acoustic duct variability and their impact on transmission loss via the Mode Interaction Parameter

Abstract

The Beaufort duct (BD) is a subsurface sound channel in the Western Arctic Ocean formed by cold Pacific winter water (PWW) sandwiched between warmer Pacific summer water (PSW) and Atlantic water (AW). Sound waves that are trapped in this duct can travel long distances without losing energy due to sea ice and surface waves interactions. This study analyzes the vertical and temporal variability of the BD using oceanographic measurements from the 2016-2017 Canada Basin Acoustic Propagation Experiment (CANAPE) and the 2019-2020 Coordinated Arctic Acoustic Thermometry Experiment (CAATEX). Here the focus is on BD normal mode propagation, and mode coupling induced by deterministic ocean features such as eddies and spicy intrusions. The observations show variability that is significant in the PSW, weak in the PWW, and moderate in the AW. Typical time scales for this variability are days to weeks. A non-dimensional quantity, the mode interaction parameter (MIP) Γ_{mn} has been defined [Colosi and Zinicola-Lapin, 2021] and quantifies the mode coupling strength between a duct mode m, and all the other modes n: MIP greater-than/less-than 1 gives strong/weak coupling. The MIP is a function of acoustic frequency, and the vertical and horizontal scales of a given perturbation field. Acoustic numerical simulations demonstrate numerous effects.

4.1 INTRODUCTION

The ongoing climate conditions that are reflected in variations in sea ice cover and thermohaline structure have had a significant impact on underwater sound transmission in the Western Arctic Ocean [Ballard et al., 2020, Duda et al., 2021, Worcester et al., 2020, Lynch et al., 2018]. In the Beaufort Sea, a cold and fresh surface layer (SL) extends to depths between 40 and 100 m, followed by a warmer and saltier layer termed the Pacific summer water (PSW) that is present between depths of 50 to 150 m [Timmermans et al., 2018, Timmermans et al., 2014]. Below the PSW lies a 100-200 m thick cold layer termed the Pacific winter water (PWW), and below that is the warmer and saltier Atlantic water (AW). From an acoustic aspect, the SL and the PSW form a shallow surface duct that traps sound waves and causes them to repeatedly interact with the underside of the seasonal ice cover [Hope et al., 2017] that varies over time and space across the annual cycle [Kucukosmanoglu et al., 2022]. Below the surface duct, a secondary duct is formed, termed the Beaufort Duct (BD), where the cold, low sound speed PWW is sandwiched between the warmer, higher sound speed PSW and AW layers [Duda et al., 2021, Kucukosmanoglu et al., 2021, Worcester et al., 2020]. The purpose of this paper is to utilize several yearlong time series of moored temperature and salinity observations to quantify the sound speed variability in the three layers that make up the BD. Here we take the view that there is a stable, roughly time-invariant background sound speed profile for the BD, and we analyze space and time perturbations to this duct, mainly due to eddies and spicy intrusions [Kucukosmanoglu et al., 2022].

The BD has been slowly strengthening across the entire western basin due to increasing ocean heat content in warm halocline water [Duda et al., 2021, Timmermans et al., 2018, Timmermans et al., 2017]. However, shorter time and

space scale ocean dynamics can affect the physical parameters of the BD [Kucukosmanoglu et al., 2021], resulting in acoustic scattering processes that can be a strong function of frequency. In discussing acoustic effects, we rely here on the normal mode interpretation of duct propagation and scattering (mode coupling) because these ducts typically support a small number of modes at 250 Hz. At higher frequencies, many modes will propagate in the duct and analysis of coupled mode propagation is less informative. Higher frequencies are prone to strong mode coupling from duct inhomogeneities leading to a complex acoustic wavefield in the duct. On the other hand, lower frequencies have fewer modes that are not as strongly trapped and show weaker coupling. But this weaker coupling can lead to energy moving out of the duct generating anomalous loss. For example, at 400 Hz, there may be only two trapped modes, so coupling of one or both of these modes into non-ducted modes can severely increase loss. It is important to note that coupling can work both ways, namely energy exiting and entering the duct [Zinicola-Lapin, 2020].

Deterministic ocean features (e.g., ocean stratification, eddies, fronts ..) can directly impact mode coupling between ducted and non-ducted modes. The Dyson series approach, which has been successfully applied in mixed layer ducts in prior works [Colosi, 2008, Colosi and Zinicola-Lapin, 2021, Yang, 2014], is used in this research to study how these features induce coupling between modes in the BD. We use the non-dimensional mode interaction parameter (MIP) matrix Γ_{mn} which quantifies the strength of mode coupling between a ducted mode m and the other n modes [Colosi and Zinicola-Lapin, 2021]. When Γ_{mn} exceeds 1, strong mode coupling and significant changes in TL can be expected. Weak coupling and small variations in TL are expected when the Γ_{mn} is less than 1. The computation of Γ_{mn} requires four important inputs, 1) the acoustic frequency, 2) the background

sound-speed profile, and the 3) depth and 4) horizontal structure of the sound-speed perturbation. The first three inputs are readily available in the present study because we have moored sound speed observations. The horizontal structure we treat as being Gaussian, with a free parameter being the typical half-width, Δ. The theory shows us that for both large and small Δ, MIP goes to zero (adiabatic limit and sudden approximation, respectively). In between these limits, there is a maximum, and in the cases analyzed here, we find maximum coupling for Δ in the range 1.5 to 2.2 km at 250 Hz.

Eddies cause significant perturbations in sound speed in the Western Arctic Ocean [Kucukosmanoglu et al., 2022], and the MIP calculation requires the vertical and horizontal scales of the eddy-driven perturbations. Our observations capture the vertical structure but not horizontal structure. In this study, we used the Massachusetts Institute of Technology General Circulation Model (MITgcm) forced with 2016 meteorological conditions that give four-dimensional (space and time) hydrographic fields of the Beaufort and Chukchi Seas [Marshall et al., 1997, Losch et al., 2010, Duda et al., 2021]. The model's outputs provide estimates of the typical horizontal scales of eddies and filaments that strengthen and weaken the BD. Two-dimensional (2D) Fourier transforms computed over 2D PSW, PSW and AW sound speed fields are used to obtain power spectra of different wave numbers in the 2016-2017 Canada Basin Acoustic Propagation Experiment (CANAPE). Our results show a red, isotropic horizontal wave number spectrum with spectral slopes of roughly k^{-3} over wave numbers between 0.01 and 0.1 cpkm (cycle per km), and roughly k^{-4} over the wave numbers between 0.1037 and 0.1561 cpkm, where maximum coupling will be shown to occur in the Beaufort Sea.

The paper's organization begins with the observations from the CANAPE and

the 2019-2020 Coordinated Arctic Acoustic Thermometry Experiment (CAATEX) in Sec. II. The MITgcm model output is also described in Sec. II. Next, Sec. III presents the methods of analysis, including a review of mode coupling, the BD acoustics, the Dyson Series, and the MIP theories. Mean mode loss, as well as its variability, are discussed in Sec. IV, and it is found how Γ_{mn} helps in predicting the stability of the BD's modes. Section V presents the geographic variability of max Γ_{mn} across the moorings. Section VI contains a summary and conclusions.

4.2 CANADA BASIN DATA AND MODEL FIELDS

Oceanographic observations from the CANAPE and the CAATEX experiments were used to evaluate the underwater acoustic conditions of the Beaufort Sea. These observations emphasize deterministic factors that influence sound propagation over a range of geographical and temporal scales up to the annual cycle. We used several standard oceanographic instruments to measure temperature, conductivity, depth (CTD) and temperature alone, to investigate the depth and temporal variations of the sound-speed profile during the CANAPE and CAATEX experiments [Kucukosmanoglu et al., 2021, Worcester et al., 2020, Sagen et al., 2020]. The time-coordinate is defined in yeardays such that 01 January 2016, 1200 UTC (CANAPE), and 01 January 2019, 1200 UTC (CAATEX), each corresponds to yearday 1.5. Fig. 4.1 shows the overall experimental geometry and bathymetry. Around 74.5°, the array approaches the critical latitude where the M2 tidal frequency is equal to the Coriolis frequency.

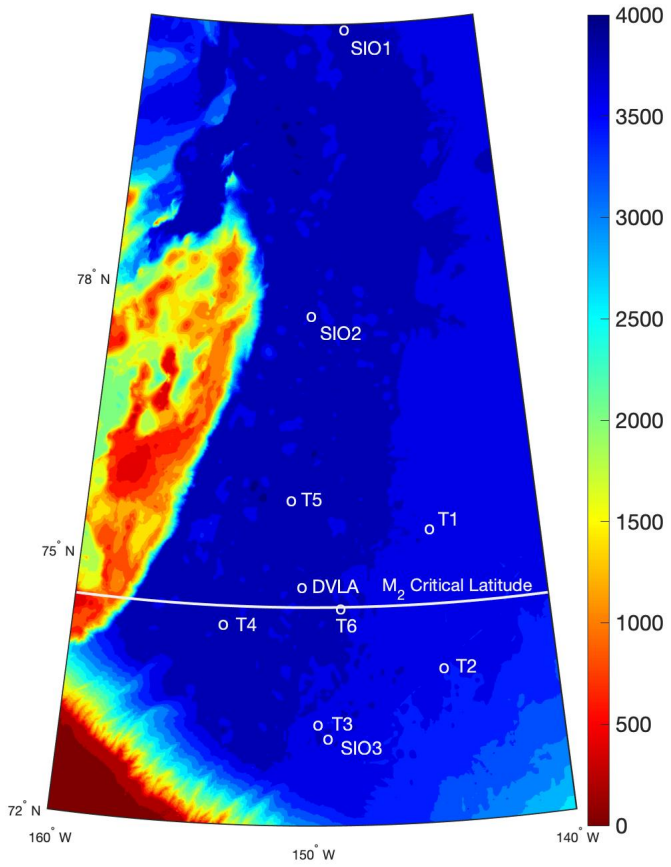

Figure 4.1: The mooring geometry for CANAPE 2016 (T1-T6, DVLA) and the three western moorings from CAATEX 2019 (SIO1-SIO3). Topography is from Sandwell/Smith [Smith and Sandwell, 1997, Becker et al., 2009, Smith and Sandwell, 2019].

4.2.1 CANAPE and CAATEX observations

The water masses of surface layer (SL), Pacific summer water (PSW), Pacific winter water (PWW), and Atlantic water (AW) play an essential role in understanding acoustic propagation in the Canada Basin. Each water mass has a specific temperature and salinity relationship [Kucukosmanoglu et al., 2021], and the resulting sound speed has important effects on ducted sound propagation.

The PSW is characterized by large temperature and salinity fluctuations, which modify the sound speed at the top of the BD. Much smaller variations are seen in the PWW and AW layers, and our measurements do not capture the SL. The SIO 2 mooring shows the warmest PSW layer of all the moorings and forms the strongest BD (See Appendix A for details). Fig. 4.2 shows the mean profiles of temperature, salinity, and sound speed derived from the CANAPE and CAATEX yearlong records (Appendix B lists oceanographic instrumentation).

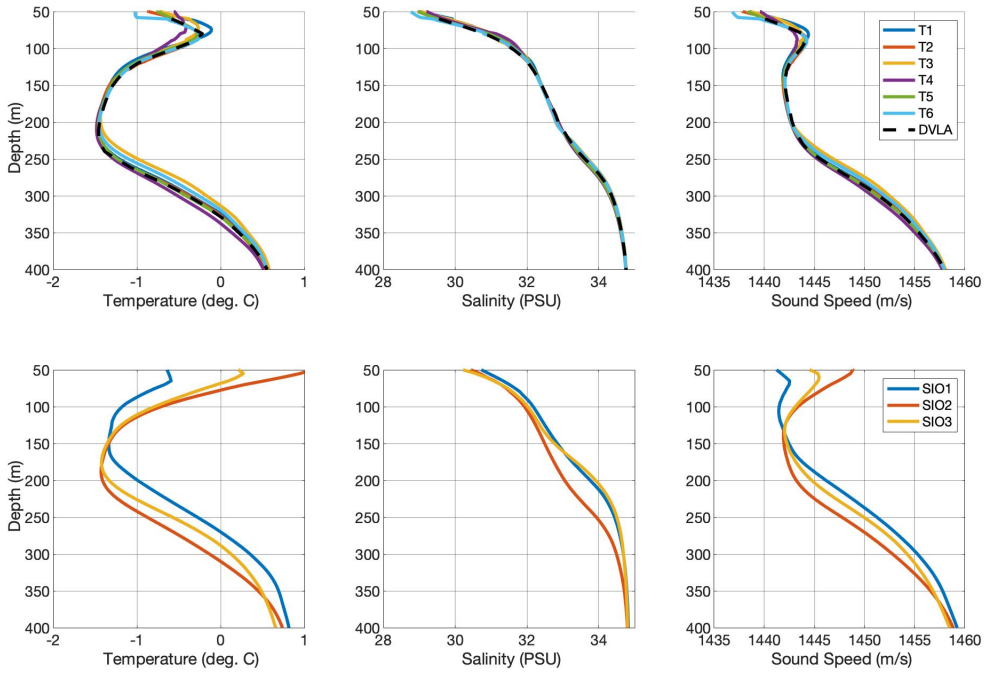

Figure 4.2: Mean profiles of temperature, salinity, and sound speed derived from the CANAPE (top) and CAATEX (bottom) moorings.

The PSW, PWW, and AW can be identified across the moorings although there are significant spatial variations of each layer. The PSW is warmer and less saline than the PWW, and the AW is warmer and more saline than the PWW. The PSW temperature maxima are 0°C at the CANAPE moorings, and greater than 0°C at the CAATEX experiment's SIO 2 and SIO 3 moorings. The PSW temperature

maxima are also shallower at SIO2 and SIO3 than at the CANAPE moorings. PWW temperature minima are nearly identical at all moorings, although they lie 20 to 30 m shallower at the CAATEX moorings. Two haloclines can be seen in both experiments, one strong in the PSW and the other weaker between the PWW and the AW.

4.2.2 MITgcm Ocean Model

The MITgcm regional hydrodynamical ocean model is described briefly here. An extensive description of the model can be found in [Duda et al., 2021]. The ocean-sea ice coupled module of the MITgcm is configured for the Chukchi Sea and Canada Basin to solve the hydrostatic primitive equations as well as sea ice momentum and thermodynamic equations using a nonlinear equation of state [Duda et al., 2021, Jackett and Mcdougall, 1995].

The model is initialized on 1 January 2016 with 3-dimensiontal temperature and salinity fields from the Arctic subpolar gyre state estimate (ASTE)[Nguyen et al., 2017, Duda et al., 2021]. It is forced on the surface by daily atmospheric conditions of 2016 from the North American Regional Reanalysis (NARR) [Mesinger et al., 2006]. The model's horizontal resolution varies throughout space. The central study domain (167°W-147°W and 71°N-76°N) has a resolution of 1 km in both the x and y directions. It covers all of the moorings in the CANAPE except T1 and T2. Beyond this domain, the horizontal resolution gradually decreases to 5 km. As for the vertical resolution, there are 40 layers with a 4 m spacing in the upper 160 m, 50 layers with a 5 m spacing between 160 and 410 m, and 16 levels with a 10 m spacing between 410 and 570 m.

The 2D FFT approach is applied to investigate the horizontal scales of eddies and filaments. Modeled sound speed field in a domain ranging from 160° to 147°

W and 73° to 76° N is used, as it includes the major region of interest from the CANAPE (See Fig. 4.1). PSW, PWW, and AW were investigated at depths of 102, 150, and 280 meters. Statistical quantities of the modeled field are found to be consistent with those observed during the CANAPE as follows: Modeled sound speeds at 102, 150, and 280 m averaged in a sub-domain covering 150°W to 151°W and 74°N to 75° have standard deviation of 0.27, 0.13, and 0.18 m/s, respectively. The CANAPE-observed sound speed standard deviations at the DVLA, which lies in the subdomain, are 0.30, 0.12, and 0.22 m/s.

We first compute the daily 2D sound speed anomaly fields for the modal by removing large-scale trends. Each anomaly field was Hanning windowed and subjected to a 2D FFT and then power spectral analysis. The spectral result was then averaged across all of the profiles as a function of horizontal wave numbers k_x and k_y. Lastly, we transformed spectrum from cartesian to polar coordinate system (k, θ), and computed the averaged 2D spectrum values along k. Results of the spectral density of sound speed anomaly at three different depth representing three different water masses in the sub-domain of 167-147°W and 71-76°N are shown in Fig. 4.3.

It can be seen from this figure that the variance is concentrated at wave numbers lower than 0.1 cpkm. The highest spectral density is in the PSW layer and occurs at the wavenumber of 0.0063 cpkm, which corresponds to a wavelength of 158.5 km. In all water masses, the majority of variance is found in the mesoscale frequency range of 0.1 to 0.01 cpkm. The variance in the submesoscale frequency domain (0.1 to 1 cpkm) decreases as eddy activity decreases. The red lines in Fig. 4.3 highlight the wavenumber range of maximum coupling for the first mode in the BD (Sections III and IV). With this wavenumber range, the standard deviations of PSW, PWW, and AW are 0.08, 0.03, and 0.01 m/s, respectively.

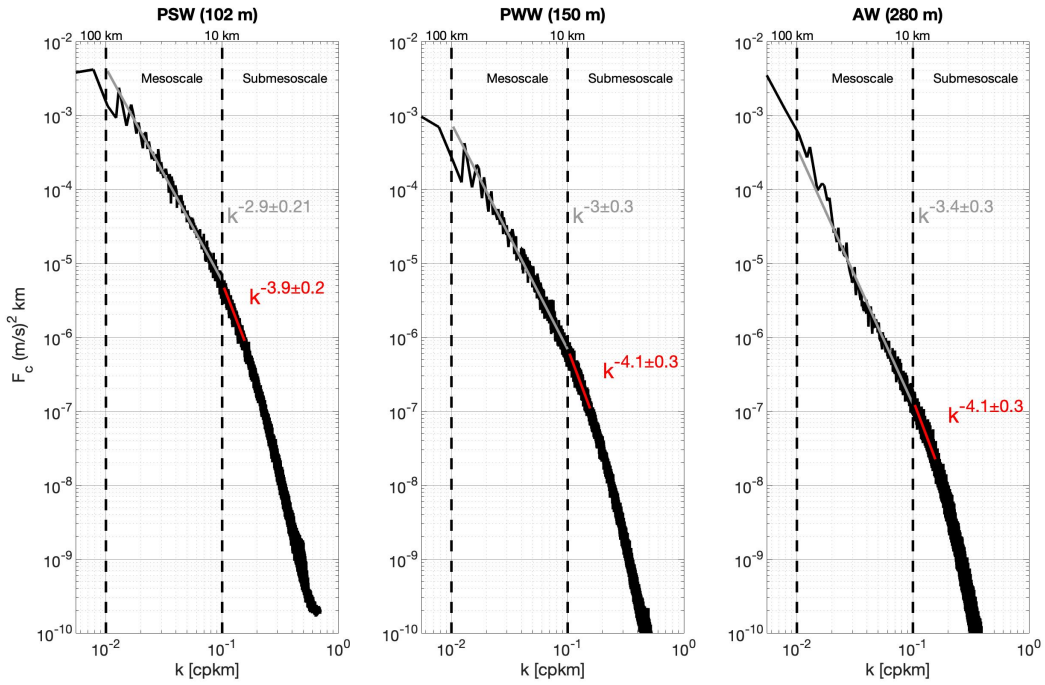

Figure 4.3: Power spectral density of sound speed at depths of 102 m (left), 150 m (middle) and 280 m (right). The wavelengths 10 and 100 km are indicated by dashed vertical lines. Power law fits (gray and red lines) to the spectra between 0.01 and 0.1 cpkm and between 0.1037 and 0.1561 cpkm are shown along with the power law exponents.

The spectrum is depth dependent in all wavenumber ranges. The PSW layer has the most variance in the mesoscale band, followed by the PWW and AW; the variance diminishes more rapidly with wave number in the AW. In the PSW, the spectra reveal the presence of an energetic submesoscale eddy field (red line). This variance is ten times that of the PWW and one hundred times that of the AW. This suggests that the PSW might have a greater impact on normal mode propagation in the BD than the PWW and AW (Section 4.4).

4.3 METHODS

4.3.1 Normal Modes

Acoustic normal modes can be classified as ducted, surface, and mixed that in the Western Arctic Ocean. The ducted modes are mode energy that is primarily confined within the BD. Surface modes are largely confined to the layers above the PSW, which are variable over the region but are not examined in detail here. The term "mixed-mode" applies to the modes in which energy is roughly equally divided between BD and surface duct.

Using normal modes [Colosi, 2016, Morozov and Colosi, 2017], the pressure field as a function of depth z and range r from a source for a given frequency ω can be expressed

$$p(r,z) = \sum_{n=1}^{N} \frac{a_n(r)\phi_n(z)}{\sqrt{k_n r}}, \tag{4.1}$$

where N is the total number of modes and $a_n(r)$ is the range-dependent mode amplitude. $\phi_n(z)$ and k_n are the vertical eigenmode function and eigen wave number for the unperturbed sound-speed profile, respectively, and they satisfy the unperturbed mode equation.

$$\rho_0(z)\frac{\partial}{\partial z}\left(\frac{1}{\rho_0(z)}\frac{\partial \phi_n}{\partial z}\right) + \left(k^2(z) - k_n^2\right)\phi_n = 0, \tag{4.2}$$

where ρ_0 is the background density and $k(z) = \omega/c(z)$. For boundary conditions, $\phi_n = 0$, and continuity of pressure and normal velocity at the water/seafloor interface. The acoustic variability induced by sound speed perturbations is contained by $a_n(r)$, which can be described using one-way coupled mode equations [Colosi, 2016, Morozov and Colosi, 2017, Colosi, 2008,

Dozier and Tappert, 1978].

$$\frac{d\hat{a}_n}{dr} = -i \sum_{m=1}^{N} \rho_{mn}(r) e^{il_{mn}r} \hat{a}_m(r), \quad l_{mn} = l_m - l_n, \tag{4.3}$$

where $\hat{a}_n(r) = a_n(r)e^{il_{mn}r}$ is the demodulated mode amplitude, $l_n = k_n + i\alpha_n$ is the horizontal complex wave number, and ρ_{mn} is the mode coupling matrix due to volumetric sound-speed fluctuations and dictates the strength of coupling between mode m and n [Colosi and Zinicola-Lapin, 2021].

Fig. 4.4 shows the normal modes for 250 Hz as a function of depth and increasing mode index for the SIO 1, SIO 2, SIO 3, and DVLA moorings yearly mean sound-speed profiles. Mode index 1 is used to begin numbering the overall modes. When it comes to duct mode numbers, BD mode 1 is the first mode trapped in the BD. SIO 2 has a stronger duct than the other moorings because it has more trapped modes. It contains roughly four modes, which are BD modes 1-4. Mode 6 is also trapped in the BD; however, there is minor leakage into the surface duct. Mode 6 and higher modes are mixed modes with varying energy amounts in the surface and BD. SIO 3 and DVLA mode sets have two completely trapped modes and one partially trapped mode in the BD. Modes 3 and 4 are ducted modes for the DVLA. Modes 2 and 3 are the ducted modes for the SIO 3. SIO 1 has just one entirely trapped mode in the BD.

The frequency dependence of the normal modes is strong. As the frequency decreases, the vertical scale of the acoustic normal modes expands, and some of them begin to interact with sea ice and surface waves, losing energy to them [Worcester et al., 2020].

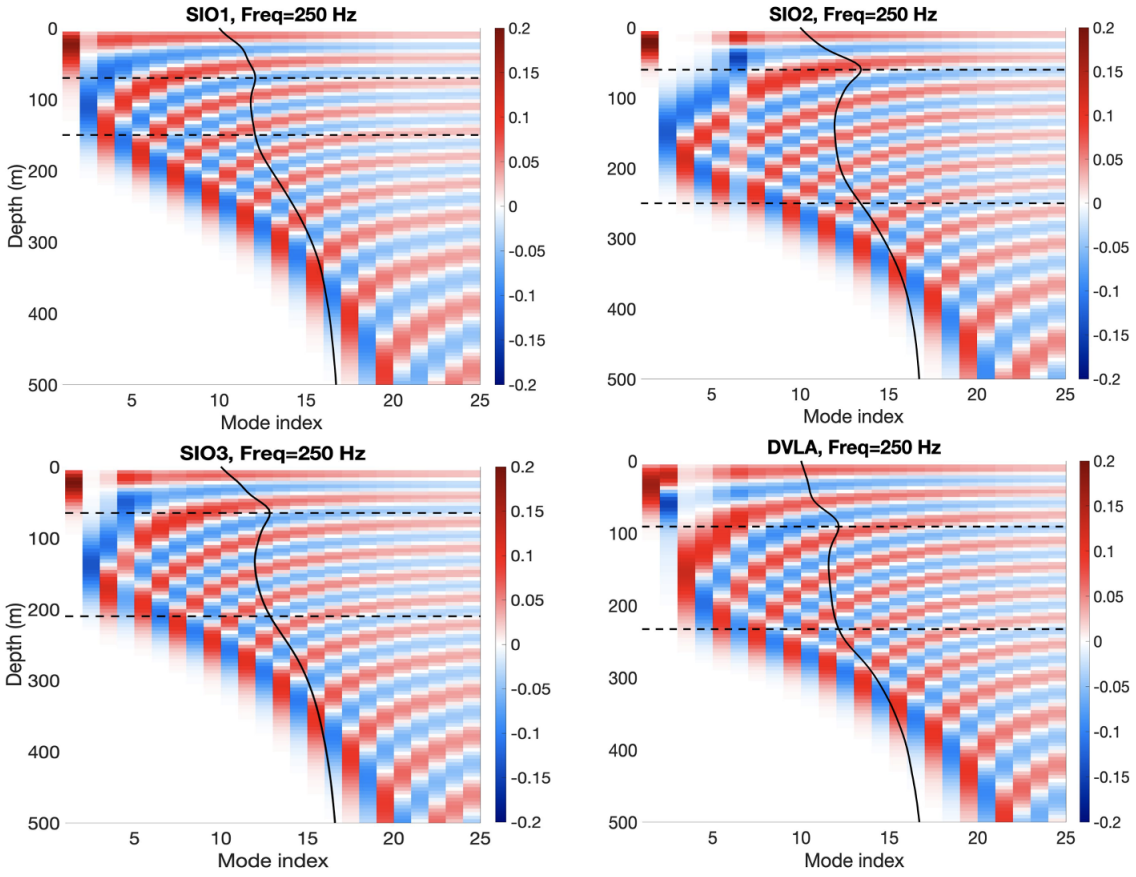

Figure 4.4: The 250 Hz normal modes for the annual average sound speed profiles (Black curves) are shown for moorings SIO 1-3 and DVLA. The depth of the sound-speed maximum in the PSW and corresponding conjugate depth are shown by dashed lines. KRAKEN (Acoustics Toolbox 2017) was used to do the calculations (HLS Inc., San Diego, CA.).

4.3.2 Beaufort Duct Acoustics

Fig. 4.5 shows the number of modes trapped in the BD as a function of time at the SIO 2 and DVLA moorings. The mode cutoff frequency and the maximum mode number are computed using the equations below [Kucukosmanoglu et al., 2021], assuming the BD is a bi-linear duct (asymmetry of the duct enters at second order).

$$f_c = \left(\frac{c_a^3}{\delta c}\right)^{1/2} \frac{1}{\delta z} \frac{3}{4\sqrt{2}} (\hat{n} - 1/2), \tag{4.4}$$

$$\hat{n} = f_c \left(\frac{c_a^3}{\delta c}\right)^{-1/2} \delta z \frac{4\sqrt{2}}{3} + 1/2, \tag{4.5}$$

where f_c is the modal cutoff frequency, c_a axial sound speed at depth z_a, c_m is maximum sound speed above and below the axis at depths z^+ and z^-, $\delta c = c_m - c_a$, $\delta z = |z^+ - z^-|$, and $\hat{n}$ is mode number.

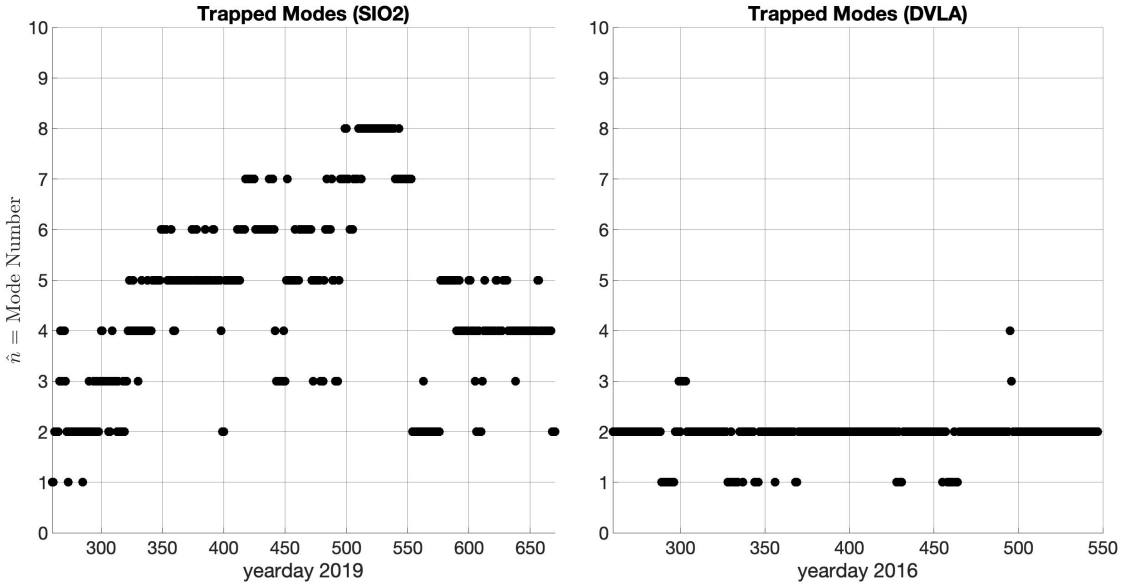

Figure 4.5: Left figure shows the time series of the entirely trapped normal modes' number for 250 Hz in the BD at the SIO 2 mooring between 16 September 2019 (yearday 260) and 31 October 2020 (yearday 670). The right panel shows the time series of the trapped normal modes' number for 250 Hz in the BD at the DVLA mooring between 16 September 2016 (yearday 260) and 03 July 2017 (yearday 550). The mode number is rounded to the nearest integer value.

Here, the yearlong trend in trapped mode numbers suggests that duct strength evolves with time, with more modes trapped in a strong duct and fewer modes trapped in a weak duct. At the DVLA mooring, the duct is relatively stable. Only one or two modes are trapped during most of the year. As for the SIO 2, the

PSW's cooling, in particular, enables more modes to leave the duct. For example, when it is colder before yearday 300 (Appendix A), only 1-3 modes are trapped. The PSW, on the other hand, warms up between yearday 500 and 550, trapping 7 to 8 modes. The relationship between temperature and salinity maxima at the PSW and the number of trapped modes in the BD were assessed using linear regression analysis (Rsq). Although both parameters are positively correlated with the number of trapped modes, temperature maximum (Rsq=0.947) is more correlated than salinity (Rsq=0.763).

Figure 4.6 shows a scatter plot of BD length δz and BD strength δc at the SIO 1- SIO 3 and DVLA moorings. The $f_c = 250$ Hz lines are derived using Eq. 4.4, marking the cutoff of modes $\hat{n} = 1$ to 5, δz and δc. Since c_a is quite stable and identical in both field experiments, the average value was used in this calculation. At the DVLA, the majority of the points are between $\hat{n} = 2$ and $\hat{n} = 3$, resulting in only two entirely trapped modes. As previously noted, SIO 2's thermohaline structure produces a strong BD, with the majority of the points in the $\hat{n} > 4$ region. The trapped modes of SIO 3 are concentrated in $2 < \hat{n} < 4$, implying that 2 and 3 modes are entirely trapped. SIO 1 is further north than the other moorings (Fig. 4.1), and the PSW is colder or non-existent at this location. As a result, only one duct is fully trapped for most of the year. Table I lists BD parameters for the DVLA and three SIO moorings.

Table 4.1: Statistics of the BD for the SIO and DVLA moorings

	δz (m)	δc (m/s)	c_a (m/s)	f_c [1] (Hz), n=1	f_c (Hz), n=2	f_c (Hz), n=3	f_c (Hz), n=4
SIO 1	103 ± 34	2.7 ± 1.8	1441 ± 0.6	119±96	357±288	595±480	833±672
SIO 2	203 ± 31	7 ± 3.2	1442 ± 0.4	32±15	96±45	160±75	224±105
SIO 3	147 ± 23	3.9 ± 2.0	1442 ± 0.6	58±29	174±87	290±145	406±203
DVLA	144 ± 10	2.2 ± 0.4	1442 ± 0.1	69±12	207±36	345±60	483±84

The error bar is the standard deviation of the variability around the mean

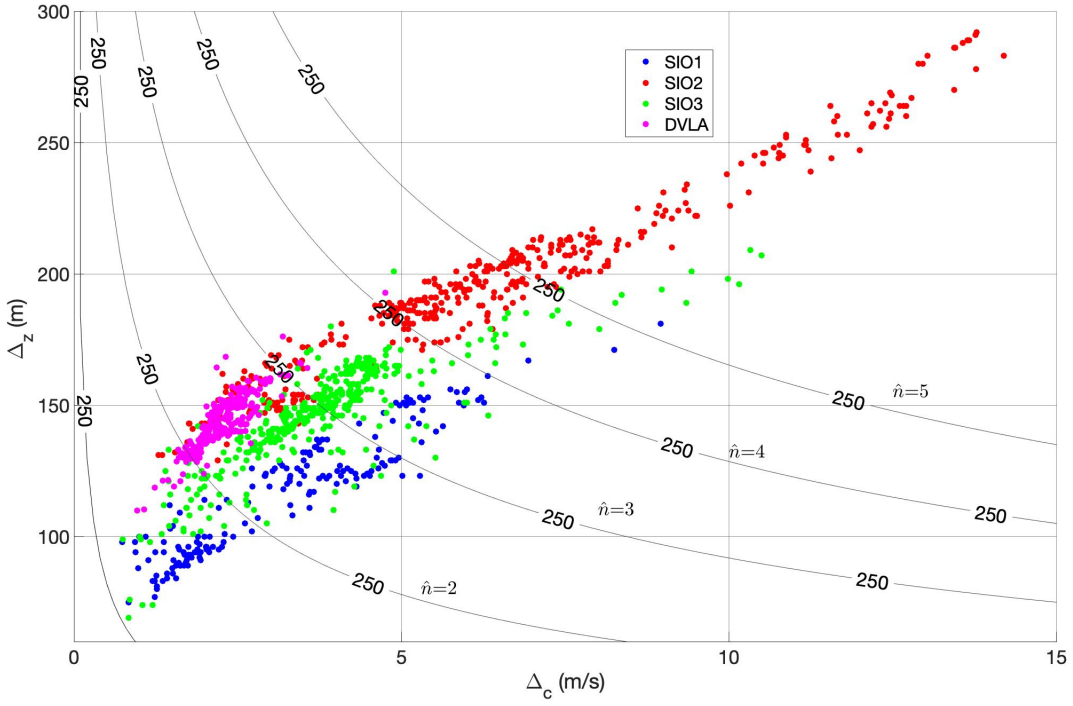

Figure 4.6: The scatter plot of δz and δc in the BD at the DVLA and SIO 1-SIO 3 moorings between 16 September 2016 (yearday 260) and 31 August 2017 (yearday 609) and between 16 September 2019 (yearday 260) and 31 October 2020 (yearday 670) respectively. Cutoff frequency, $f_c = 250$ Hz lines derived using Eq. 4.4 are shown with black lines.

during the year. The BD parameters at the DVLA were more stable than at the other moorings. The cutoff frequencies with and without the assumption of bilinear duct are well-correlated. The cutoff frequency of the bi-linear duct is approximately 7-15% greater than the cutoff frequency of the actual duct.

4.3.3 Dyson Series and Mode Interaction Parameter (MIP)

The Dyson series from quantum mechanical perturbation theory is used in this study to address the change in the mode amplitudes caused by deter-

ministic ocean features [Sakurai and Commins, 1995, Dyson, 1949, Colosi, 2008, Colosi and Zinicola-Lapin, 2021]. The ocean features are modeled using a Gaussian perturbation centered at range r_0 with width Δ,

$$\delta c(r,z) = \delta c_0 \psi(z) \exp\left(-\frac{(r-r_0)^2}{\Delta^2}\right), \tag{4.6}$$

where δc_0 is the perturbation strength and $\psi(z)$ is a unit maximum depth function, r_0 the position of the feature. It has been shown [Colosi, 2008] that the first-order change in mode amplitude at range R having traversed the perturbation in Eq. 4.7 is

$$|a_n(R)|^2 = \left[|a_n(0)|^2 + \sum_{m=1}^{N} A_{mn} Z_{mn} X_{mn} \sin(k_{mn} r_0)\right] e^{-2\alpha_n R}, \tag{4.7}$$

where $A_{mn} = A_m A_n$ is a matrix of the initial mode amplitudes, $k_{mn} = k_m - k_n$ is the beat wave number, and r_0 is the center of the feature [Colosi and Zinicola-Lapin, 2021, Colosi, 2008]. Z_{mn} represents the contribution to mode coupling due to the depth structure of the acoustic modes and ocean features, and X_{mn} represents the contribution due to the horizontal structure of the ocean feature. These matrices can be written as follows:

$$Z_{mn} = -\frac{\delta c_0}{c_0} \frac{q_0^2}{\sqrt{k_m k_n}} \int_0^\infty \psi(z) \frac{\phi_n(z)\phi_m(z)}{\rho_0(z)} dz, \tag{4.8}$$

$$X_{mn} = 2\pi^{1/2} \Delta \exp\left[-\frac{k_{mn}^2 \Delta^2}{4}\right]. \tag{4.9}$$

Z_{mn} is dependent on the overlap between the ocean perturbation as a function of depth and the vertical eigenmode functions of modes m and n. If the perturbation occurs at a depth where neither mode n nor mode m has significant amplitude, this term goes to zero, and, the change in mode energy goes to zero.

As for the horizontal structure, X_{mn} will go to zero for both large and small Δ. Maximum coupling between modes therefore occurs for some intermediate value. The sine term in Eq. 4.7 means that depending on the distance between r_0 and the position of the source/receiver, the change in mode energy will fluctuate.

Here, the dimensionless mode interaction parameter (MIP) of [Colosi and Zinicola-Lapin, 2021] is used to quantify the strength of coupling between modes m and n, and just a brief discussion of the MIP is given here. The MIP contains the matrixes X_{mn} and Z_{mn} and can be expressed as

$$\Gamma_{mn} = |Z_{mn}| X_{mn}. \tag{4.10}$$

Γ_{mn} is a function of the acoustic frequency, ocean perturbation parameters, and the vertical eigenmode functions and eigen wave numbers of modes m and n. It is not dependent on the source and receiver depths, and it does not specify explicitly that mode m or n loses or gains energy. When $\Gamma_{mn} > 1$, multiple scattering and strong coupling occur, and significant changes in TL are expected. When $\Gamma_{mn} < 1$, single scattering and weak coupling occur, and minor changes in TL are found. Because of the form of X_{mn}, there is a value of Δ that gives a maximum in Γ, i.e., $\Delta = 2^{1/2}/k_{mn}$, where $k_{mn} = 2\pi/\lambda_{mn}$. When plugging this into the equation for maximum coupling, it was found that $\Delta = \lambda_{mn}/\sqrt{2}\pi$. Maximum coupling for the first mode in the BD was computed across the CANAPE, and was found that it occurs between 0.1037 and 0.1561 cpkm, which corresponds to 2.2 and 1.5 km for Δ values.

4.3.4 Application to the Beaufort duct

Figure 4.7 shows an example of perturbed, $c(z)$, and unperturbed, $\bar{c}(z)$, profiles from the SIO 1 mooring. The unperturbed profile is the year-long mean sound

speed profile, and the perturbed profile is the daily mean sound speed profile on 22 April 2020. The sound speed perturbation is

$$\delta c_0 \psi(z) = c(z) - \bar{c}(z) \tag{4.11}$$

The cutoff frequencies for the unperturbed profile for BD modes 1–3 are 173, 521, and 869 Hz, respectively. In this example, the PSW has shifted and cooled significantly in the top 100 m. Therefore, the BD gets thinner, δ_z is reduced, and the cutoff frequencies rises to 254, 763, and 1272 Hz. Because of this severe disruption, the sound is expected to escape the duct, causing the ducted sound level to diminish.

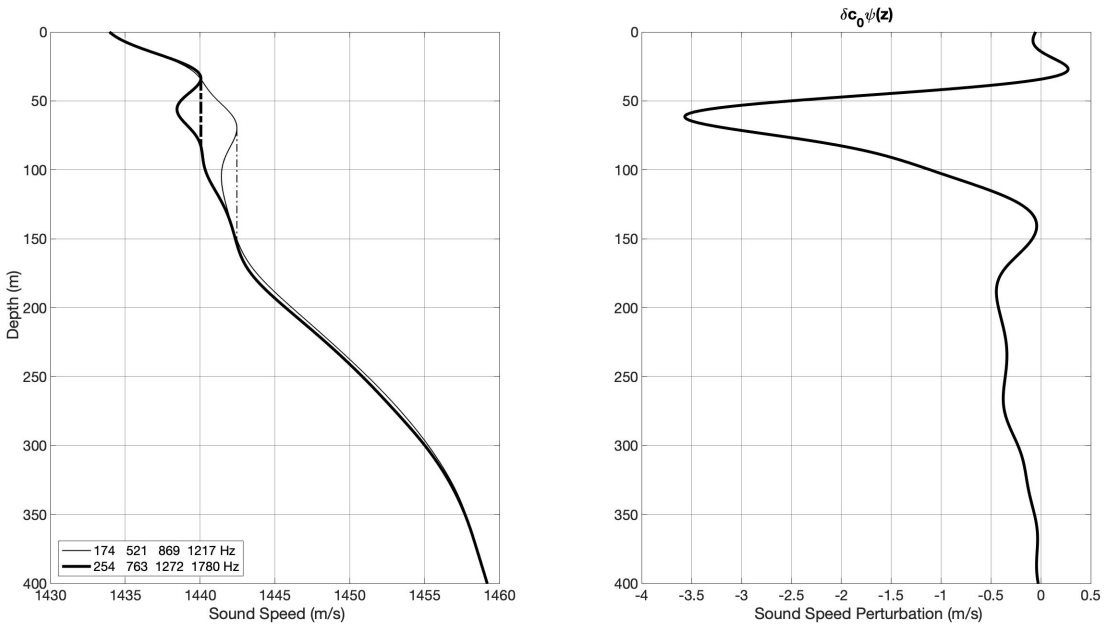

Figure 4.7: (Left) Perturbed and unperturbed sound-speed profiles in the upper 400 m at SIO 1 mooring. The thick black line is the perturbed profile on 22 April 2020, and the thin black line is the yearly mean profile. Dash-dot lines indicate the vertical length of the duct for each sound-speed profile. (Right) The sound speed perturbation in the upper 400 m.

As previously noted, the acoustic frequency sets the resonant beat wave num-

ber for the background sound-speed profile (Eq. 4.9). The beat wave number leads to strong fluctuations in the acoustic intensity if it overlaps the horizontal scales of sound speed variability. Therefore, the frequency dependence of the strength of coupling between ducted modes is also a key question. Fig. 4.8 shows the Γ_{mn} analysis of mode 2 at 250 Hz (Γ_{2n}) and mode 5 at 950 Hz (Γ_{5n}) as a function of n and Δ for the same environment as Fig. 4.7. BD mode 1 corresponds to waveguide modes 2 and 5 at 250 and 950 Hz, respectively. At 250 Hz, it can be seen that mode 2 strongly interacts with mode 3, and slightly interacts with modes 1 and 5. Maximum interaction occurs at about $\Delta = 2$ km. At 950 Hz, mode 5 interacts with modes 6 and 7. Maximum interaction occurs at about $\Delta = 1.5$ km and is higher than the maximum interaction at 250 Hz. This is most likely because higher frequencies are subject to greater mode coupling.

To demonstrate the relationship between Γ_{mn} and cutoff frequency, a scatter plot of them, as well as the time series of both parameters, are shown in Fig. 4.9. About half of the points in this figure are for Γ_{mn} values substantially lower than 1, and f_c below 100 Hz. This indicates weak or moderate coupling and, most likely, modest TL fluctuations due to the low MIP values. When the Γ_{mn} value exceeds 1, the cutoff frequency increases and more coupling, multiple scattering, and TL fluctuations are expected. Between yeardays 340 and 500, the duct weakens or disappears, and f_c rises to significantly higher or infinite values. BD mode 1 scatters out of the duct and couples with non-ducted modes because f_c is higher than the acoustic frequency of 250 Hz. Γ_{mn} values are also at their peaks at these times.

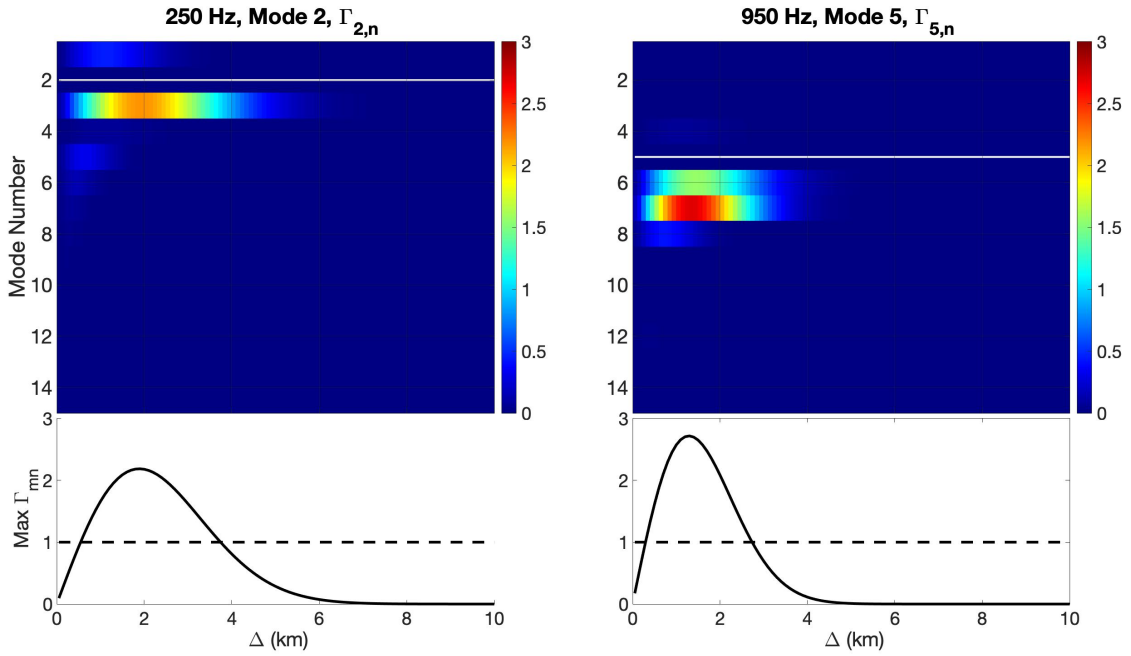

Figure 4.8: The upper panel shows Γ_{mn} values as a function of Δ and neighbour n for two different frequencies, 250 and 950 Hz, and for two different modes. As for Fig. 4.7, the date is 22 April 2020. Mode 2 and Mode 5 are represented by the white lines. Lower panels show the maximum of Γ_{2n} and Γ_{5n} at 250 Hz and 950 Hz as a function of Δ.

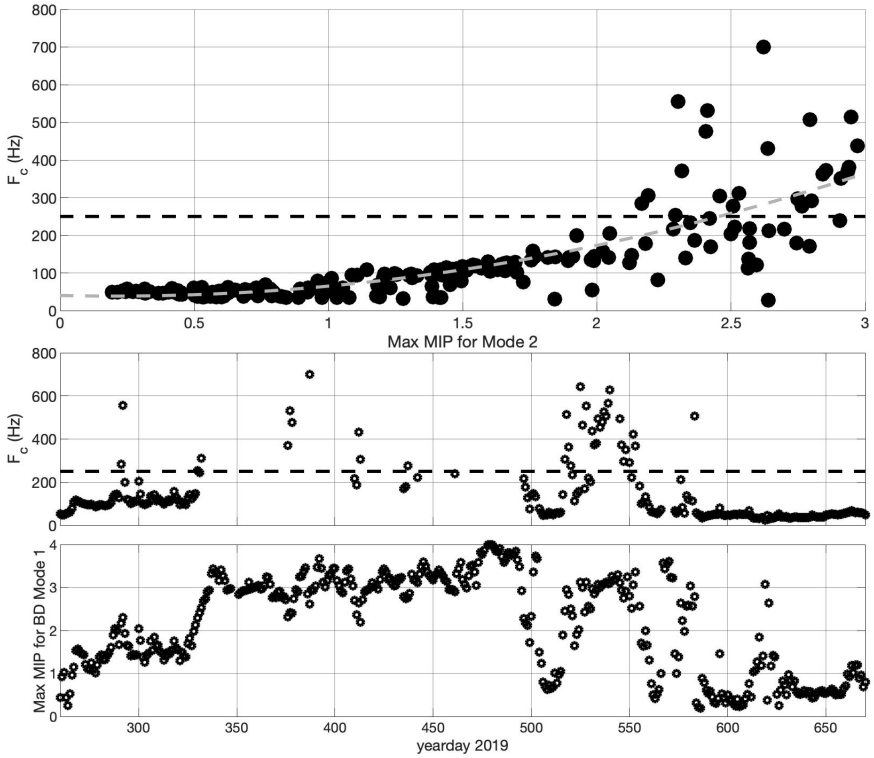

Figure 4.9: The upper panel shows the scatter plot of the maximum MIP for mode 2 at 250 Hz (BD Mode 1) (See Fig. 4.4) and cutoff frequency f_c for mode 2 at SIO 1 mooring between 16 September 2019 and 31 October 2020. The grey curve line is a second-order polynomial curve. 250 Hz is indicated with a horizontal dashed line. The middle and lower panels show the time series of f_c for mode 2, and the time series of the maximum MIP for mode 2.

4.4 MODE COUPLING IN TYPICAL FEATURES

Using numerical simulation, this section discusses ducted modal loss variability at 250 Hz for three separate perturbation scenarios: an upper halocline cold eddy, an upper halocline warm eddy, and a lower halocline cold eddy. Because SIO 2 and 3 have more trapped modes than SIO 1 mooring (Fig. 4.4), the coupling between the ducted modes is computed for these moorings. The numerical solution of one-way coupled-mode equations is used to carry out the acoustic propagation simulations, as explained in [Colosi and Zinicola-Lapin, 2021, Dozier and Tappert, 1978], using input from observations. Statistics of mode loss variability and the BD's MIP are compared as a function of width Δ. The simulated range dependent mode amplitude is used to define modal loss for a given Δ [Colosi and Zinicola-Lapin, 2021] and is provided by

$$\text{Loss}_m(r) = -20\log_{10}\left(\frac{|a_m(r)|}{|a_m(0)|}\right). \tag{4.12}$$

When $\text{Loss}_m(r)$ is positive, the mode is losing energy. When it is negative, the mode is gaining energy.

4.4.1 Upper Halocline Cold Eddy (SIO 2)

Figure 4.10 shows the observed unperturbed and perturbed profiles at SIO 2 for a cold eddy to demonstrate the sound-speed variations that change the duct configuration. The cold eddy has no effect on the cutoff frequency in this example, but it creates a -3 m/s perturbation, displacing the duct axis upper by 28 m, from 141 to 113 m, causing it to take on an asymmetric form.

The observations do not constrain the horizontal structure of the sound-speed

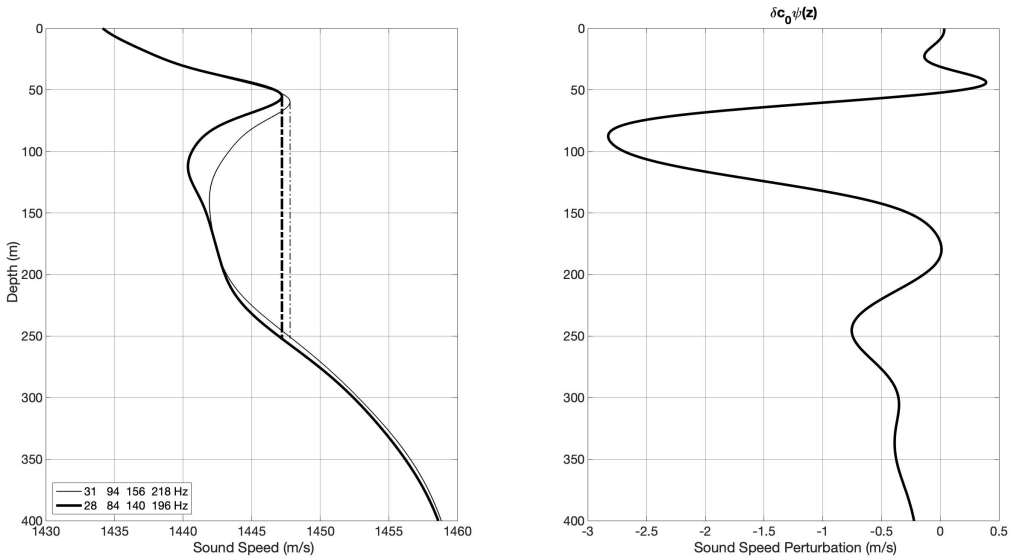

Figure 4.10: Same as Fig. 4.7 except for a cold eddy at SIO 2 on 14 February 2020.

perturbation. As stated earlier, Γ_{mn} goes to 0 for both small and large Δ values, and the TL and mode energy are expected to show little or no fluctuation. Direct numerical simulations are used to explore the effects of the intermediate values of Δ. The total sound speed perturbation is modeled as a function of depth and range using the Eq. 4.11 with parameters r_0=30 to 70 km at 10 km intervals, Δ = 0.1, 0.25, 0.5, 1, 2, 3... 10 km, and r ranges from 0 to 100 km. The source is located at a depth of 110 m. The receiver range is 100 km. The sound speed perturbation at $r = r_0$ is identical to the measurements in the right panel of Fig. 4.10. The simulation gives $a_n(r)$.

Comparing the statistics of $\text{Loss}_m(r)$ over the values of r_0 to the Γ_{mn} as a function of Δ for modes 2 and 3 at 250 Hz (BD modes 1 and 2) (Fig. 4.4) provides more information. The mean and standard deviation of $\text{Loss}_m(r, \Delta)$ over the values of r_0 at $r = 100$ km are computed. The mean loss is

$$\text{Loss}_m(r,\Delta) = \frac{\sum_{i=1}^{N} \text{Loss}_m(r, r_{0i}, \Delta)}{N}, \tag{4.13}$$

where N is the number of r_0, used in the simulations. The maximum of Γ_{2n} occurs for $n = 3$, while the maximum of Γ_{3n} occurs for $n = 4$. When Δ is smaller than 0.5 km and larger than 4 km, both Γ_{mn} and $\text{Loss}_m(r)$ go to zero, and the standard deviation of $\text{Loss}_m(r)$ is small. However, when Δ is between 0.5 and 4 km, the maximum Γ_{mn} for modes 2 and 3 rises above 1, showing significant coupling between modes. In this case, the mean mode gain/loss and its variability are higher. It should be emphasized that loss varies depending on the source depth, and Γ_{mn} only provides the strength of the coupling between the modes, not the details of the losses. In this example, the perturbation brought the duct axis closer to the source depth, which might explain why mode 2 with smaller horizontal launch angles gained energy, while mode 3 with larger horizontal launch angles lost energy.

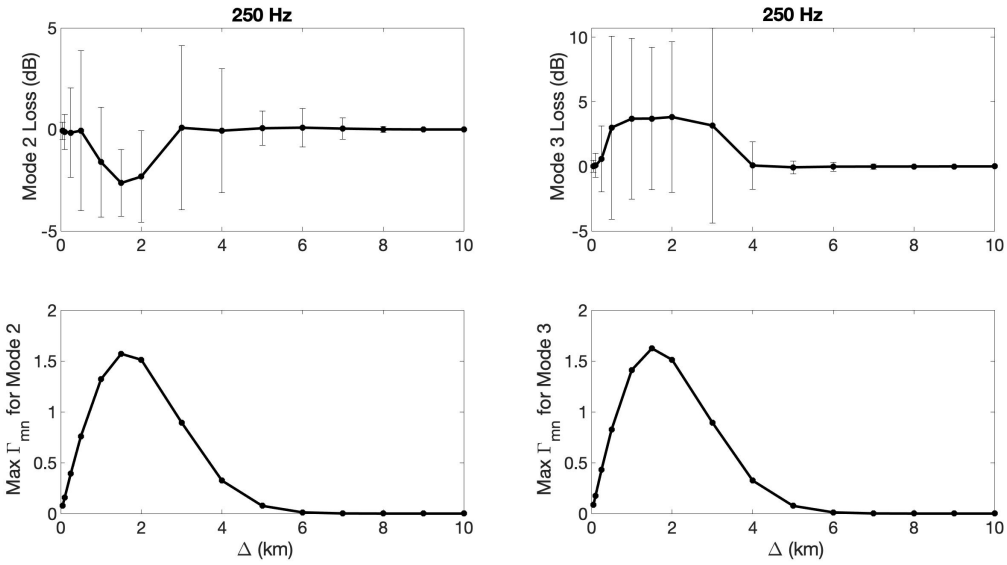

Figure 4.11: (Top) For the upper halocline cold eddy (Fig. 4.10) statistics of mode 2 and 3 losses at 250 Hz as a function of Δ. (Bottom) For $m = 2$ and $m = 3$ maximum Γ_{mn} as a function of Δ.

4.4.2 Upper Halocline Warm Eddy (SIO 2)

Unperturbed and perturbed sound speed profiles for a warm eddy at the SIO 2 are shown in Fig. 4.12. The warm eddy strengthened the duct significantly and reduced the cutoff frequency by a factor of two. The depth of the duct axis increased from 141 to 156 m, and the maximum perturbation was roughly 6 m/s at a depth of 50 m.

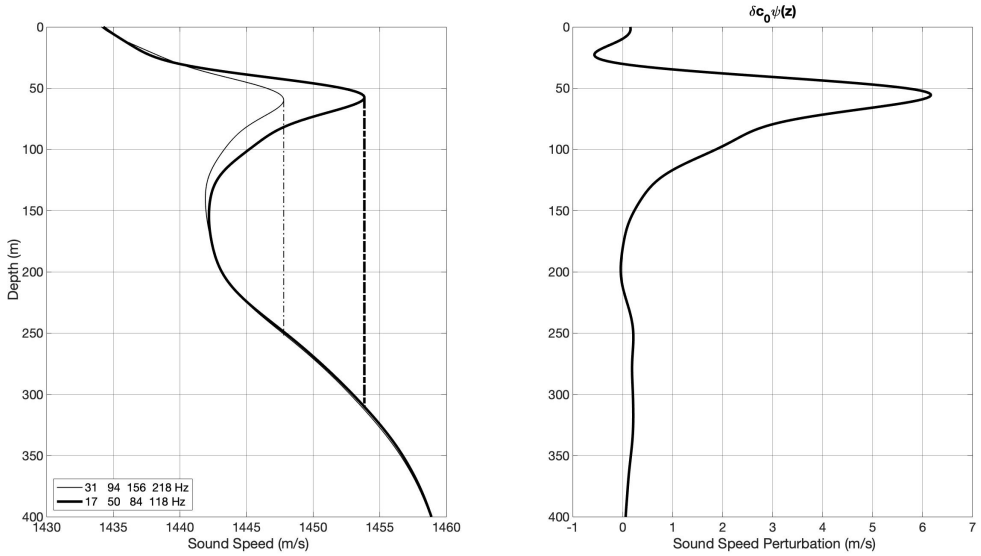

Figure 4.12: Same as Fig. 4.7 except for a warm eddy at SIO 2 on 28 May 2020.

Figure 4.13 shows the losses for modes 2 and 3, as well as the maximum Γ_{mn} values, as a function of Δ. The parameters r_0 and Δ, as well as the source depth and acoustic frequency, are the same as in the "Cold Eddy" case. Again, the maximum Γ_{2n} occurs for n=3, while the maximum Γ_{3n} occurs for n=4. When Δ is lower than 0.5 km and larger than 4 km, the $\text{Loss}_m(r)$ and Γ_{mn} go to 0, and the standard deviations are small. However, as Δ varies between 0.5 and 4 km, Γ_{mn} for mode 2 rises but stays below the 1. Γ_{mn} for mode 3 increases slightly over the 1. The correlation between Γ_{mn} and $\text{Loss}_m(r)$ is robust, but mode loss and its variability for modes 2 and 3 are lower than in the cold eddy case. Both modes 2

and 3 have losses of up to 2 dB.

Again, depending on the source depths, the loss will vary. In this scenario, the perturbation pushed the duct axis 15 m away from the source depth, and the Γ_{mn} values for mode 2 are less than one, which might explain why modes 2 and 3 both lose energy despite the duct being stronger.

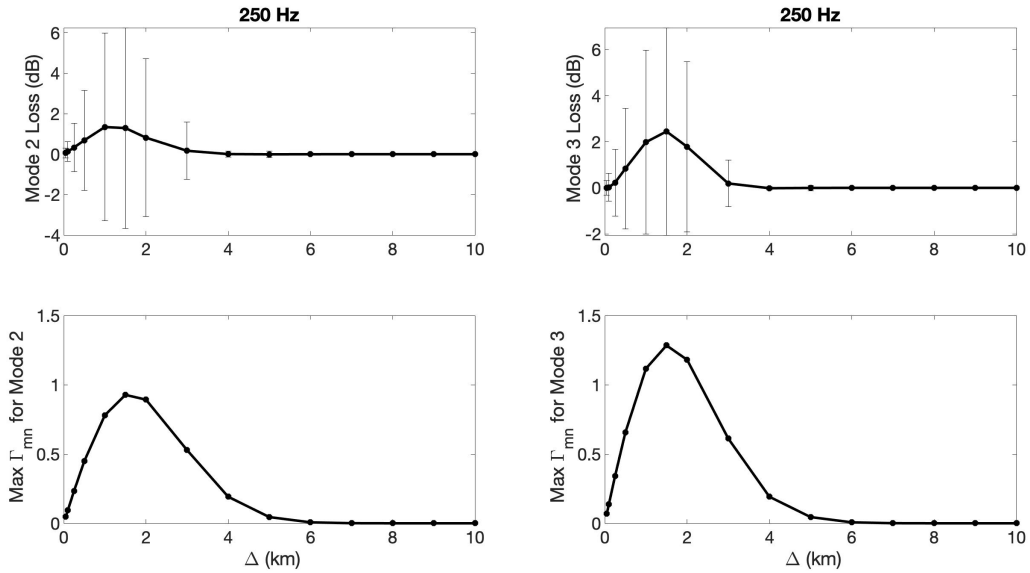

Figure 4.13: Same as Fig. 4.11 except for an upper halocline warm eddy (Fig. 4.12) at SIO 2.

4.4.3 Lower Halocline Cold Eddy (SIO 3)

Figure 4.14 shows perturbed and unperturbed sound-speed profiles for a lower halocline cold eddy at SIO 3. Unlike previous examples, this profile was taken from the SIO-3 mooring. In this case, the cold eddy strengthened the duct and lowered the cutoff frequency. The duct axis did not change, and the maximum perturbation was roughly -4 m/s at a depth of 250 m.

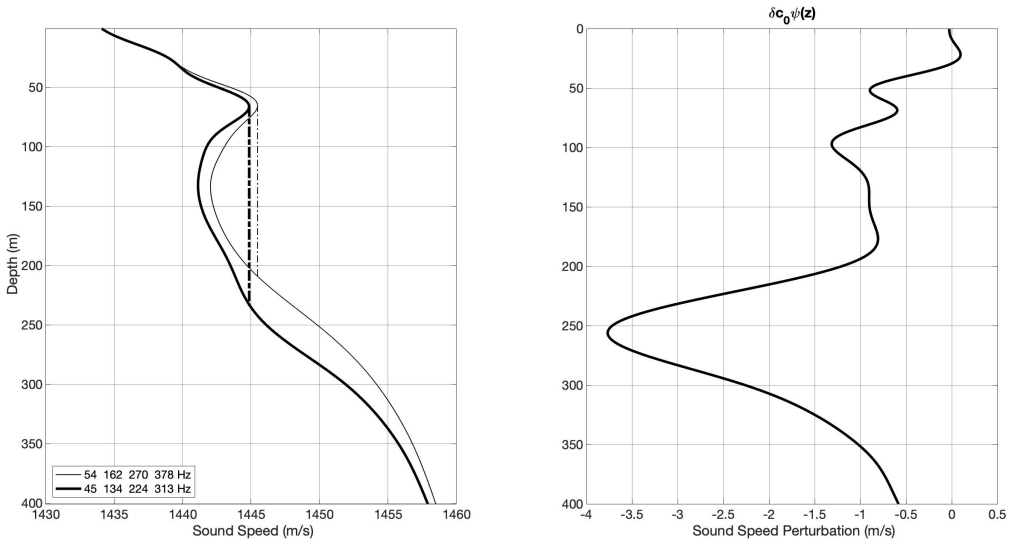

Figure 4.14: Same as Fig. 4.7 except for a lower halocline cold eddy at SIO 3 on 21 September 2020.

The BD at SIO 3 is weaker duct than at SIO 2, and the yearly average profile has trapped two modes: mode 2 and mode 3 (BD modes 1 and 2) (Fig. 4.4). Fig. 4.15 shows the statistics for these modes, which were calculated using the same r_0 and Δ parameters as in previous eddy examples, as well as the same source depth and acoustic frequency. Modes 2 and 3 have the largest Γ_{mn} value with each other, unlike the preceding examples. When Δ is lower than 0.5 km and larger than 5 km, both Γ_{mn} and $\mathrm{Loss}_m(r)$, as well as the standard deviations, are almost zero. When Δ varies between 0.5 and 5 km, modes 2 and 3 have losses of

less than 0.2 dB. Γ_{mn} never exceeds 0.2, suggesting the weak scattering regime. The correlation between Γ_{mn} and $\mathrm{Loss}_m(r)$ is again excellent.

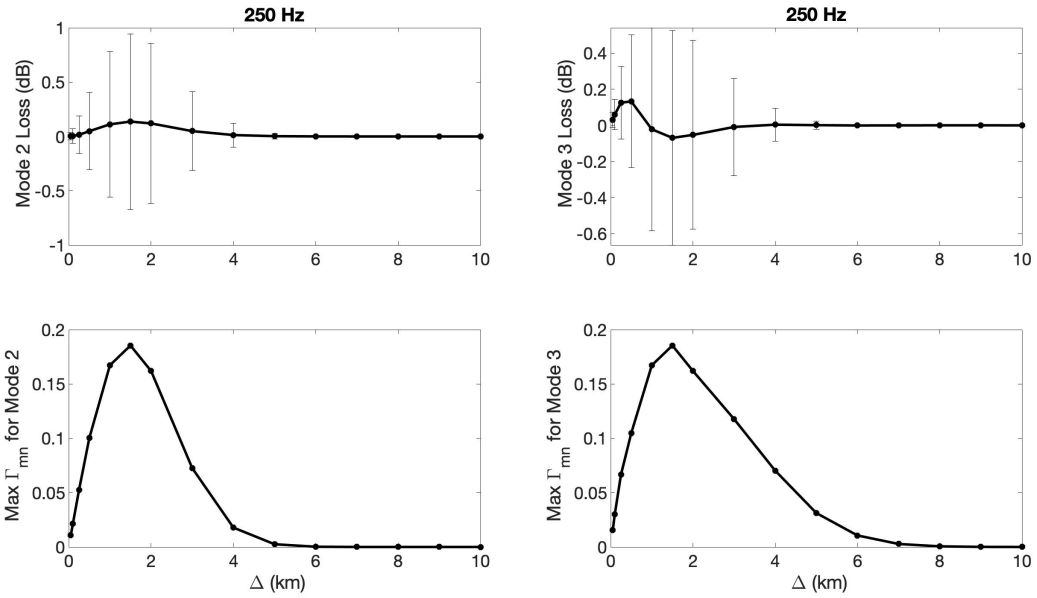

Figure 4.15: Same as Fig. 4.11 except for a lower halocline cold eddy at SIO 3 (Fig. 2.15).

4.5 GEOGRAPHIC VARIABILITY OF THE MAXIMUM Γ_{mn} ACROSS Δ

For 250 Hz, the maximum Γ_{mn} across eight moorings were computed for two periods, 16 September 2016 (yearday 260) to 31 August 2017 (yearday 609) for the six T-moorings and DVLA, and 16 September 2019 (yearday 260) to 31 August 2020 (yearday 609) for the SIO 3 mooring. The most weakly trapped BD mode was selected to analyze the influence of deterministic features on the maximum Γ_{mn}. These modes interact with the upper and lower boundaries of the BD (mode 4 for the DVLA and T-moorings and mode 3 for SIO 3), making these modes more sensitive to the deterministic features in the PSW along the upper boundary.

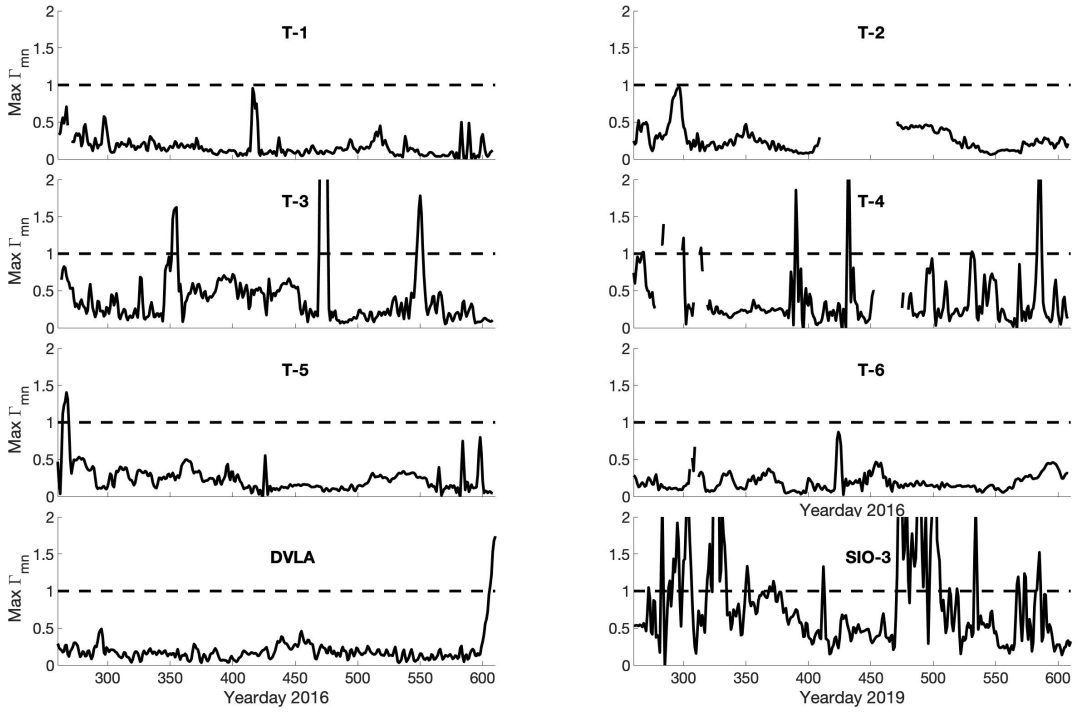

Figure 4.16: Γ_{mn} as a function of yearday for moorings T1-T6, DVLA, SIO 3. Mode 4 was used for the T1-T6 and DVLA moorings, and mode 3 was used for the SIO 3 mooring. Γ_{mn}=1 is indicated by a horizontal dashed line.

The maximum Γ_{mn} is found to be relatively stable for the CANAPE moorings, except for T3 and T4. These two moorings contain more energetic upper ocean eddies, which, might be significant scatterers of acoustic energy away from the duct. These characteristics are successfully captured by the MIP, which is greater than 1 upon these yeardays. The SIO 3 and T3 moorings are located in the same region (Fig. 4.1) but are separated in time by 3 years. Despite their proximity, the PSW yearly mean maximum temperature is warmer by 0.5° and the PSW depth is shallower by 20 m at SIO 3 (Fig. 4.2). The PWW minimum temperature remained constant, but is shallower by about 20 m at the SIO 3. At the SIO 3 mooring, 23% of the maximum Γ_{mn} values are greater than 1. T4 and T3 have around 8% and 6% of the total greater than 1, respectively. Maximum Γ_{mn} values less than 1 occur less than 1% of the ratio at the rest of the moorings.

4.6 Summary and Conclusions

In this work, the non-dimensional mode interaction parameter Γ_{mn} was defined, and the single-scattering Dyson series technique [Colosi, 2008] was proven to be successful in explaining acoustic propagation stability across perturbations induced by various types of eddies in the BD. Three different eddy cases with source depths of 110 m were studied using direct coupled mode numerical simulations at 250 Hz, and two distinct propagation regimes were found. Multiple scattering and strong mode coupling were observed when the Γ_{mn} between the modes m and n is greater than 1. Moderate or weak coupling was observed when the Γ_{mn} between the modes is less than 1. Source or receiver depths do not affect Γ_{mn}, and Γ_{mn} does not indicate whether mode n or m loses or gains energy. However, it accurately provides the coupling strength between the modes m and n.

In the typical Beaufort Sea environment, maximum variations in mode energy are predicted for at horizontal perturbation scales between 1.5 and 2.2 km, where variance in the regional MITgcm model are much less than in the mesoscale eddy band (Fig 4.3). Changes in the mode energy are almost non-existent for the horizontal scales perturbation less than 0.5 km and greater than 5 km. Except for the T3 and T4 moorings, the maximum Γ_{mn} is found to be relatively stable in the CANAPE experiment. At 950 Hz the maximum Γ_{5n} occur at slightly smaller value of Δ than the maximum Γ_{2n} at 250 Hz.

Acknowledgments

This research was supported by the Office of Naval Research (ONR), and the author, Murat Kucukosmanoglu, was supported by an ONR Ocean Acoustics Graduate Student Fellowship under Award Number N00014-19-1-2203. This material is based on work supported by the ONR under Award Number N00014-15-2068 and Research Council of Norway under Grant No. 280531. We thank the Royal Norwegian Coast Guard and crew on board KV Svalbard, for allocating ship time and field support during the cruise. Any opinions, findings, conclusions or recommendations expressed in this publication are those of the authors and do not necessarily reflect the views of the ONR.

APPENDIX A: Depth-time series of the temperature and mean profiles at the SIO 2 mooring

Fig. 4.17 shows a yearlong depth-time series of temperature and the mean profiles of temperature, salinity, and sound speed at the SIO 2 mooring (See Fig. 4.1). The root mean square (RMS) variability of these parameters as a function of depth is also displayed to indicate the fluctuations over the yearlong cycle.

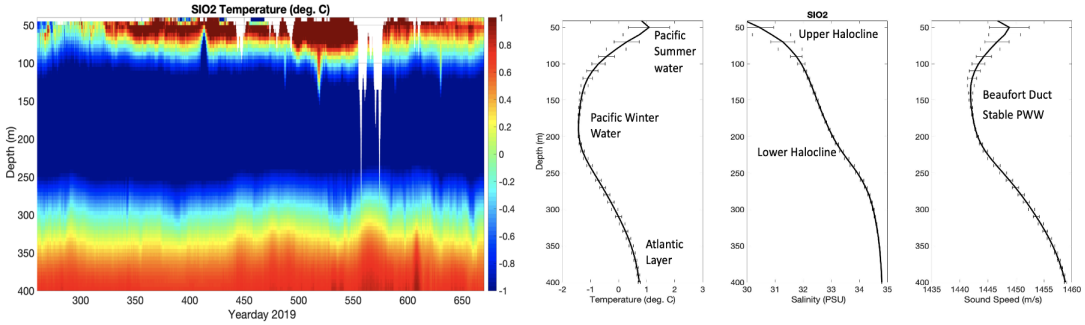

Figure 4.17: The left panel shows the depth-time series of the temperature in the upper 400 m at the SIO 2 mooring between 16 September 2019 (yearday 260) and 31 October 2020 (yearday 670). The right panel shows the SIO 2 annual average mean temperature, salinity, and sound speed profiles with RMS statistics shown as horizontal lines.

APPENDIX B: Oceanographic Instrumentation

The CAATEX SIO moorings included 1 SBE 37 SM at 50-m, 40 hydrophone modules (HMs) between 61 and 1232 m, and 20 moored CTDs (SBE 37-SMP, SBE3 9/PLUS, SBE 39-T/P and SBE 56) between 70 and 1010 m. The moored CTDs in the CAATEX experiment did not measure salinity below 150 m. Therefore, the salinity profiles were predicted using the T/S diagram of the CTD casts made near the SIO moorings. Temperature data was collected for the CANAPE experiment using 15 moored HMs between 50 and 173-m and 10 thermistors between 180 and 570-m in the T moorings. The distributed vertical line array (DVLA) included 28 Sea-Bird MicroCats (SBE 37-SMP/SM) between 50 and 425-m and 60 Hydrophone Modules nominally spanning 47–587 m. The average profile of shipboard CTD casts collected over the CANAPE was used to predict the salinity profile of T-moorings using the T/S diagram of the CTDs.

Chapter 5

Conclusion

Due to significant changes in currents, thermohaline structure, and sea ice extent, the Western Arctic Ocean has gotten a lot of attention in the last two decades. Ocean acoustic conditions that affect sound propagation on different period scales cannot be correctly predicted without a detailed understanding of the physical oceanographic processes. Similarly, understanding the changing ice cover as a function of time and space is essential for implementing these predictive efforts and may also aid in ice property monitoring. These objectives were addressed in this thesis by utilizing observations from CANAPE 2016–2017 and CAATEX 2019–2020.

In Chapter 2, measurements from the 2016–2017 CANAPE were studied throughout the yearly cycle to show how the current and thermohaline structures influence fluctuations in sound speed. The water masses of ASW, PSW, PWW, and AW and vertical displacements due to eddies, internal waves, and internal tides that caused sound speed fluctuations were quantified using temperature and salinity data. The most significant sound speed variations have been observed in the 50–100 m deep region, caused by spice. These changes affect the BD's upper axis and the surface duct's lower axis. Eddies showed large fluctuations, whereas the super-inertial or internal wave band showed smaller fluctuations in the upper layer. Building on chapter 2, I suggest further in-situ acoustic experiments to investigate the levels of significance and variability of the PSW, PWW and AW. Furthermore, I encourage the deployment of the ice-tethered profiler (ITP) to characterize the upper layer, particularly the surface layer beneath sea ice, more actively.

In Chapter 3, I discuss sea ice scattering statistics of 11–12.5 kHz acoustic transmissions in the Beaufort Sea region of the Arctic Ocean. The critical finding from this study was the discovery of five significant surface scattering

epochs. They were identified using the arrival angle, moment of reflected intensity, probability density function, scintillation index (SI) and pulse time spread. One unexpected result of this research is that the spread is lower under the IT than under the IF and IS. We hypothesize that reducing the isotropic correlation length and raising the square RMS phase to minimize contributions to the mean square pressure, or that increased roughness and ice keels contribute to out-of-plane scattering and high angle scattering, resulting in less energy being scattered in the receiver's direction. The next phase in this research was to quantify the ice properties and qualitatively explain the various mechanisms that regulate these fluctuations in the reflected intensity. This leads us to conclude that the fluctuations are caused by a mix of mechanisms at the ice/water interface involving ice composition, thickness, roughness, and ice keels. In light of Chapter 3, I propose that the experimental setup be adjusted to avoid intertransponder interference. In addition, proper receivers equipped to record mid-to high-frequency signals are required to measure the signals' vertical statistics. Following these adjustments, the data will offer more information on the changing ice properties over the Arctic Ocean, as well as the computation of the reflection coefficient.

Chapter 4 introduced the non-dimensional mode interaction parameter Γ_{mn}, and the single scattering Dyson series approach [Colosi, 2008] was shown to be successful in explaining the acoustic propagation stability over perturbations caused by various forms of eddies in the BD. Variability is high when the MIP between two ducted modes surpasses 1, but mode-mode interference patterns grow more complicated. Calculating the energy transfer between modes and developing an acoustical model to predict acoustic observables are important. A future study will focus on analyzing the acoustic transmission data from the CANAPE and subsequently develop acoustic propagation models to predict mean Transmission

Loss (TL) and TL fluctuations. Here it will be important to distinguish between the energy that is primarily trapped in the BD and that which is interacting with the ice. Acoustic phase and intensity fluctuation, as well as vertical coherence, intensity covariance, acoustic arrival pattern, peak pulse intensity, PDFs, and pulse time spread will be investigated. I will focus on three distinct timefront regions: 1) early ray-like arrivals that are well resolved in time, have interaction with the ice cover and are not influenced strongly by the BD, 2) late arriving ducted mode-like arrivals that have a complex interference pattern and are trapped by the BD, and 3) transition arrivals that are a mixture of ducted and non-ducted energy that interact with the ice cover and surface waves. I intend to improve my analysis and outcomes and work on an acoustic propagation model that can predict acoustic observables, including transmission loss, scintillation and fade-out rates, and coherence. The MIP will be used to explore the coupling between BD modes and other modes, and the results will be analyzed together with changes in observables.

Bibliography

[Abramowitz and Stegun, 1972] Abramowitz, M. and Stegun, I. A. (1972). *Handbook of Mathematical Functions*. Dover, Mineola, NY.

[Alexander et al., 2012] Alexander, P., Duncan, A., and Bose, N. (2012). Modelling sound propagation under ice using the ocean acoustics library's acoustic toolbox. *Proceedings of the Acoustical Society of Australia*.

[Alexander et al., 2013] Alexander, P., Duncan, A., Bose, N., and Smith, D. (2013). Modelling acoustic transmission loss due to sea ice cover. *Acoustics Australia*, 41(1).

[Ballard, 2019] Ballard, M. S. (2019). Three-dimensional acoustic propagation effects induced by the sea ice canopy. *The Journal of the Acoustical Society of America*, 146(4):EL364–EL368.

[Ballard et al., 2020] Ballard, M. S., Badiey, M., Sagers, J. D., Colosi, J. A., Turgut, A., Pecknold, S., Lin, Y.-T., Proshutinsky, A., Krishfield, R., Worcester, P. F., et al. (2020). Temporal and spatial dependence of a yearlong record of sound propagation from the canada basin to the chukchi shelf. *The Journal of the Acoustical Society of America*, 148(3):1663–1680.

[Bassett et al., 2020] Bassett, C., Lavery, A. C., Lyons, A. P., Wilkinson, J. P., and Maksym, T. (2020). Direct inference of first-year sea ice thickness using broadband acoustic backscattering. *The Journal of the Acoustical Society of America*, 147(2):824–838.

[Becker et al., 2009] Becker, J., Sandwell, D., Smith, W., Braud, J., Binder, B., Depner, J., Fabre, D., Factor, J., Ingalls, S., Kim, S., et al. (2009). Global bathymetry and elevation data at 30 arc seconds resolution: SRTM30_PLUS. *Marine Geodesy*, 32(4):355–371.

[Bell Jr, 1975] Bell Jr, T. (1975). Topographically generated internal waves in the open ocean. *Journal of Geophysical Research*, 80(3):320–327.

[Bird et al., 2008] Bird, K. J., Charpentier, R. R., Gautier, D. L., Houseknecht, D. W., Klett, T. R., Pitman, J. K., Moore, T. E., Schenk, C. J., Tennyson,

M. E., and Wandrey, C. R. (2008). Circum-arctic resource appraisal: Estimates of undiscovered oil and gas north of the arctic circle. Technical report, US Geological Survey.

[Bishop, 1989] Bishop, G. C. (1989). A bistatic, high-frequency, under-ice, acoustic scattering model. i: Theory. *The Journal of the Acoustical Society of America*, 85(5):1903–1911.

[Brannigan et al., 2017] Brannigan, L., Johnson, H., Lique, C., Nycander, J., and Nilsson, J. (2017). Generation of Subsurface Anticyclones at Arctic Surface Fronts due to a Surface Stress. *Journal of Physical Oceanography*, 47(11):2653–2671.

[Brekhovskikh, 1960] Brekhovskikh, L. (1960). *Waves in layered media*, volume 16. Elsevier.

[Carpenter and Timmermans, 2012] Carpenter, J. and Timmermans, M.-L. (2012). Deep mesoscale eddies in the Canada basin, Arctic ocean. *Geophysical Research Letters*, 39(20).

[Clay and Medwin, 1977] Clay, C. S. and Medwin, H. (1977). *Acoustical Oceanography: PRinciples and Applications*. Wiley-Interscience.

[Colosi, 2008] Colosi, J. A. (2008). Acoustic mode coupling induced by shallow water nonlinear internal waves: Sensitivity to environmental conditions and space-time scales of internal waves. *The journal of the acoustical society of America*, 124(3):1452–1464.

[Colosi, 2016] Colosi, J. A. (2016). *Sound propagation through the stochastic ocean*. Cambridge University Press.

[Colosi and Baggeroer, 2004] Colosi, J. A. and Baggeroer, A. B. (2004). On the kinematics of broadband multipath scintillation and the approach to saturation. *The Journal of the Acoustical Society of America*, 116(6):3515–3522.

[Colosi et al., 2012] Colosi, J. A., Duda, T. F., Lin, Y.-T., Lynch, J. F., Newhall, A. E., and Cornuelle, B. D. (2012). Observations of sound-speed fluctuations on the New Jersey continental shelf in the summer of 2006. *The Journal of the Acoustical Society of America*, 131(2):1733–1748.

[Colosi et al., 2018] Colosi, J. A., Kucukosmanoglu, M., Worcester, P. F., Dzieciuch, M., Proshutinsky, A. Y., Krishfield, R. A., and Nash, J. D. (2018). An overview of beaufort sea eddies, internal waves, and spice from several recent field efforts and implications for acoustic propagation. *The Journal of the Acoustical Society of America*, 144(3):1665–1665.

[Colosi et al., 2001] Colosi, J. A., Tappert, F., and Dzieciuch, M. (2001). Further analysis of intensity fluctuations from a 3252-km acoustic propagation experiment in the eastern north pacific ocean. *The Journal of the Acoustical Society of America*, 110(1):163–169.

[Colosi et al., 2013] Colosi, J. A., Van Uffelen, L. J., Cornuelle, B. D., Dzieciuch, M. A., Worcester, P. F., Dushaw, B. D., and Ramp, S. R. (2013). Observations of sound-speed fluctuations in the western Philippine Sea in the spring of 2009. *The Journal of the Acoustical Society of America*, 134(4):3185–3200.

[Colosi and Zinicola-Lapin, 2021] Colosi, J. A. and Zinicola-Lapin, W. (2021). Sensitivity of mixed layer duct propagation to deterministic ocean features. *The Journal of the Acoustical Society of America*, 149(3):1969–1978.

[D'Asaro, 1985] D'Asaro, E. A. (1985). The energy flux from the wind to near-inertial motions in the surface mixed layer. *Journal of Physical Oceanography*, 15(8):1043–1059.

[DiMaggio et al., 2018] DiMaggio, D., Colosi, J. A., Joseph, J., Pearson, A., Worcester, P. F., and Dzieciuch, M. A. (2018). Observations of thermohaline sound-speed structure induced by internal waves and spice in the summer 2015 Canada Basin marginal ice zone. *Elem Sci Anth*, 6(1).

[Dosser and Rainville, 2016] Dosser, H. V. and Rainville, L. (2016). Dynamics of the changing near-inertial internal wave field in the Arctic Ocean. *Journal of Physical Oceanography*, 46(2):395–415.

[Dosser et al., 2014] Dosser, H. V., Rainville, L., and Toole, J. M. (2014). Near-inertial internal wave field in the Canada Basin from ice-tethered profilers. *Journal of physical oceanography*, 44(2):413–426.

[Dozier and Tappert, 1978] Dozier, L. and Tappert, F. (1978). Statistics of normal mode amplitudes in a random ocean. ii. computations. *The Journal of the Acoustical Society of America*, 64(2):533–547.

[Duckworth et al., 2001] Duckworth, G., LePage, K., and Farrell, T. (2001). Low-frequency long-range propagation and reverberation in the central arctic: Analysis of experimental results. *The Journal of the Acoustical Society of America*, 110(2):747–760.

[Duda et al., 2012] Duda, T. F., Collis, J. M., Lin, Y.-T., Newhall, A. E., Lynch, J. F., and DeFerrari, H. A. (2012). Horizontal coherence of low-frequency fixed-path sound in a continental shelf region with internal-wave activity. *The Journal of the Acoustical Society of America*, 131(2):1782–1797.

[Duda et al., 2021] Duda, T. F., Zhang, W. G., and Lin, Y.-T. (2021). Effects of pacific summer water layer variations and ice cover on beaufort sea underwater sound ducting. *The Journal of the Acoustical Society of America*, 149(4):2117–2136.

[Dyson, 1949] Dyson, F. J. (1949). The radiation theories of tomonaga, schwinger, and feynman. *Physical Review*, 75(3):486.

[Dzieciuch et al., 2004] Dzieciuch, M., Munk, W., and Rudnick, D. L. (2004). Propagation of sound through a spicy ocean, the SOFAR overture. *The Journal of the Acoustical Society of America*, 116(3):1447–1462.

[Dzieciuch, 2014] Dzieciuch, M. A. (2014). Signal processing and tracking of arrivals in ocean acoustic tomography. *The Journal of the Acoustical Society of America*, 136(5):2512–2522.

[Fine et al., 2018] Fine, E. C., MacKinnon, J. A., Alford, M. H., and Mickett, J. B. (2018). Microstructure observations of turbulent heat fluxes in a warm-core Canada Basin eddy. *Journal of Physical Oceanography*, 48(10):2397–2418.

[Flatté et al., 1979] Flatté, S., Dashen, R., Munk, W., Watson, K., and Zachariasen, F. (1979). Sound transmission through a Fluctuating Ocean.

[Freitag et al., 2017] Freitag, L., Koski, P., Singh, S., Maksym, T., and Singh, H. (2017). Acoustic communications under shallow shore-fast arctic ice. In *OCEANS 2017-Anchorage*, pages 1–5. IEEE.

[Frey et al., 2015] Frey, K. E., Moore, G., Cooper, L. W., and Grebmeier, J. M. (2015). Divergent patterns of recent sea ice cover across the bering, chukchi, and beaufort seas of the pacific arctic region. *Progress in Oceanography*, 136:32–49.

[Fricke, 1991] Fricke, J. R. (1991). Acoustic scattering from elastic ice: A finite difference solution. Technical report, WOODS HOLE OCEANOGRAPHIC INSTITUTION MA.

[Gaillard et al., 2006] Gaillard, F., Terre, T., and Guillot, A. (2006). Monitoring moored instrument motion by optimal estimation. *Ocean engineering*, 33(1):1–22.

[Garrett and Kunze, 2007] Garrett, C. and Kunze, E. (2007). Internal tide generation in the deep ocean. *Annu. Rev. Fluid Mech.*, 39:57–87.

[Garrison et al., 1991] Garrison, G., Francois, R., and Wen, T. (1991). Acoustic reflections from arctic ice at 15–300 khz. *The Journal of the Acoustical Society of America*, 90(2):973–984.

[Gavrilov and Mikhalevsky, 2006a] Gavrilov, A. N. and Mikhalevsky, P. N. (2006a). Low-frequency acoustic propagation loss in the arctic ocean: Results of the arctic climate observations using underwater sound experiment. *The Journal of the Acoustical Society of America*, 119(6):3694–3706.

[Gavrilov and Mikhalevsky, 2006b] Gavrilov, A. N. and Mikhalevsky, P. N. (2006b). Low-frequency acoustic propagation loss in the arctic ocean: Results of the arctic climate observations using underwater sound experiment. *The Journal of the Acoustical Society of America*, 119(6):3694–3706.

[Haine et al., 2015] Haine, T. W., Curry, B., Gerdes, R., Hansen, E., Karcher, M., Lee, C., Rudels, B., Spreen, G., de Steur, L., Stewart, K. D., et al. (2015). Arctic freshwater export: Status, mechanisms, and prospects. *Global and Planetary Change*, 125:13–35.

[Halle and Pinkel, 2003] Halle, C. and Pinkel, R. (2003). Internal wave variability in the Beaufort Sea during the winter of 1993/1994. *Journal of Geophysical Research: Oceans*, 108(C7).

[Hebert and Moum, 1994] Hebert, D. and Moum, J. (1994). Decay of a near-inertial wave. *Journal of physical oceanography*, 24(11):2334–2351.

[Hobæk and Sagen, 2016] Hobæk, H. and Sagen, H. (2016). On underwater sound reflection from layered ice sheets. *arXiv preprint arXiv:1604.02247*.

[Hope et al., 2017] Hope, G., Sagen, H., Storheim, E., Hobæk, H., and Freitag, L. (2017). Measured and modeled acoustic propagation underneath the rough arctic sea-ice. *The Journal of the Acoustical Society of America*, 142(3):1619–1633.

[Hudson et al., 2013] Hudson, S. R., Granskog, M. A., Sundfjord, A., Randelhoff, A., Renner, A. H., and Divine, D. V. (2013). Energy budget of first-year arctic sea ice in advanced stages of melt. *Geophysical Research Letters*, 40(11):2679–2683.

[Jackett and Mcdougall, 1995] Jackett, D. R. and Mcdougall, T. J. (1995). Minimal adjustment of hydrographic profiles to achieve static stability. *Journal of Atmospheric and Oceanic Technology*, 12(2):381–389.

[Jackson, 1994] Jackson, D. (1994). Apl-uw high-frequency ocean environmental acoustic models handbook. *Applied Physics Laboratory, University of Washington, Technical Report*, 9407(102):1499–1510.

[Jackson and Richardson, 2007a] Jackson, D. R. and Richardson, M. D. (2007a). *High-Frequency Seafloor Acoustics*. Springer, New York, NY.

[Jackson and Richardson, 2007b] Jackson, D. R. and Richardson, M. D. (2007b). Physical properties. pages 75–122.

[Jensen et al., 1995] Jensen, F. B., Kuperman, W. A., Porter, M. B., Schmidt, H., and McKay, S. (1995). Computational ocean acoustics. *Computers in Physics*, 9(1):55–56.

[Jensen et al., 2011] Jensen, F. B., Kuperman, W. A., Porter, M. B., Schmidt, H., and Tolstoy, A. (2011). *Computational ocean acoustics*, volume 794. Springer.

[Jezek et al., 1990] Jezek, K., Stanton, T., Gow, A., and Lange, M. (1990). Influence of environmental conditions on acoustical properties of sea ice. *The Journal of the Acoustical Society of America*, 88(4):1903–1912.

[Jin et al., 1994] Jin, G., Lynch, J. F., Pawlowicz, R., and Worcester, P. (1994). Acoustic scattering losses in the greenland sea marginal ice zone during the 1988–89 tomography experiment. *The Journal of the Acoustical Society of America*, 96(5):3045–3053.

[Kovacs, 1996] Kovacs, A. (1996). Sea ice. part 1, bulk salinity versus ice floe thickness.

[Krishfield et al., 2014] Krishfield, R. A., Proshutinsky, A., Tateyama, K., Williams, W. J., Carmack, E. C., McLaughlin, F. A., and Timmermans, M.-L. (2014). Deterioration of perennial sea ice in the beaufort gyre from 2003 to 2012 and its impact on the oceanic freshwater cycle. *Journal of Geophysical Research: Oceans*, 119(2):1271–1305.

[Kucukosmanoglu et al., 2022] Kucukosmanoglu, M., Colosi, J. A., Worcester, P. F., Dzieciuch, M. A., Olson, D. R., Richards, E. L., and Miller, C. W. (2022). Beaufort sea observations of 11 to 12.5 khz surface pulse reflections near 50 degree grazing angle from summer 2016 to summer 2017. *The Journal of the Acoustical Society of America*, 151(1):106–125.

[Kucukosmanoglu et al., 2021] Kucukosmanoglu, M., Colosi, J. A., Worcester, P. F., Dzieciuch, M. A., and Torres, D. J. (2021). Observations of sound-speed fluctuations in the beaufort sea from summer 2016 to summer 2017. *The Journal of the Acoustical Society of America*, 149(3):1536–1548.

[Kuperman and Schmidt, 1986] Kuperman, W. and Schmidt, H. (1986). Rough surface elastic wave scattering in a horizontally stratified ocean. *The Journal of the Acoustical Society of America*, 79(6):1767–1777.

[Kwok, 2018] Kwok, R. (2018). Arctic sea ice thickness, volume, and multiyear ice coverage: losses and coupled variability (1958–2018). *Environmental Research Letters*, 13(10):105005.

[Laible and Rajan, 1996] Laible, H. A. and Rajan, S. D. (1996). Temporal evolution of under ice reflectivity. *The Journal of the Acoustical Society of America*, 99(2):851–865.

[LePage and Schmidt, 1994] LePage, K. and Schmidt, H. (1994). Modeling of low-frequency transmission loss in the central arctic. *The Journal of the Acoustical Society of America*, 96(3):1783–1795.

[LePage and Schmidt, 1996] LePage, K. and Schmidt, H. (1996). Analysis of spatial reverberation statistics in the central arctic. *The Journal of the Acoustical Society of America*, 99(4):2033–2047.

[Levine et al., 1987] Levine, M. D., Paulson, C. A., and Morison, J. H. (1987). Observations of internal gravity waves under the Arctic pack ice. *Journal of Geophysical Research: Oceans*, 92(C1):779–782.

[Losch et al., 2010] Losch, M., Menemenlis, D., Campin, J.-M., Heimbach, P., and Hill, C. (2010). On the formulation of sea-ice models. part 1: Effects of different solver implementations and parameterizations. *Ocean Modelling*, 33(1-2):129–144.

[Lyard, 1997] Lyard, F. H. (1997). The tides in the Arctic Ocean from a finite element model. *Journal of Geophysical Research: Oceans*, 102(C7):15611–15638.

[Lynch et al., 2018] Lynch, J. F., Gawarkiewicz, G. G., Lin, Y.-T., Duda, T. F., and Newhall, A. E. (2018). Impacts of ocean warming on acoustic propagation over continental shelf and slope regions. *Oceanography*, 31(2):174–181.

[Marshall et al., 1997] Marshall, J., Hill, C., Perelman, L., and Adcroft, A. (1997). Hydrostatic, quasi-hydrostatic, and nonhydrostatic ocean modeling. *Journal of Geophysical Research: Oceans*, 102(C3):5733–5752.

[Martini et al., 2014] Martini, K. I., Simmons, H. L., Stoudt, C. A., and Hutchings, J. K. (2014). Near-inertial internal waves and sea ice in the Beaufort Sea. *Journal of physical oceanography*, 44(8):2212–2234.

[Maslanik et al., 2007] Maslanik, J., Fowler, C., Stroeve, J., Drobot, S., Zwally, J., Yi, D., and Emery, W. (2007). A younger, thinner arctic ice cover: Increased potential for rapid, extensive sea-ice loss. *Geophysical Research Letters*, 34(24).

[Maslanik et al., 2011] Maslanik, J., Stroeve, J., Fowler, C., and Emery, W. (2011). Distribution and trends in arctic sea ice age through spring 2011. *Geophysical Research Letters*, 38(13).

[McCammon and McDaniel, 1985] McCammon, D. F. and McDaniel, S. T. (1985). The influence of the physical properties of ice on reflectivity. *The Journal of the Acoustical Society of America*, 77(2):499–507.

[McPhee, 2008] McPhee, M. (2008). *Air-ice-ocean interaction: Turbulent ocean boundary layer exchange processes*. Springer Science & Business Media.

[Mesinger et al., 2006] Mesinger, F., DiMego, G., Kalnay, E., Mitchell, K., Shafran, P. C., Ebisuzaki, W., Jović, D., Woollen, J., Rogers, E., Berbery, E. H., et al. (2006). North american regional reanalysis. *Bulletin of the American Meteorological Society*, 87(3):343–360.

[Mikhalevsky et al., 2015] Mikhalevsky, P. N., Sagen, H., Worcester, P. F., Baggeroer, A. B., Orcutt, J., Moore, S. E., Lee, C. M., Vigness-Raposa, K. J., Freitag, L., Arrott, M., et al. (2015). Multipurpose acoustic networks in the integrated arctic ocean observing system. *Arctic*, pages 11–27.

[Morison et al., 1985] Morison, J. H., Long, C. E., and Levine, M. D. (1985). Internal wave dissipation under sea ice. *Journal of Geophysical Research: Oceans*, 90(C6):11959–11966.

[Morozov and Colosi, 2017] Morozov, A. K. and Colosi, J. A. (2017). Equations for normal-mode statistics of sound scattering by a rough elastic boundary in an underwater waveguide, including backscattering. *The Journal of the Acoustical Society of America*, 142(3):EL292–EL298.

[Morozov and Paka, 2010] Morozov, E. and Paka, V. (2010). Internal waves in a high-latitude region. *Oceanology*, 50(5):668–674.

[Munk, 1981] Munk, W. (1981). Internal waves and small-scale processes. *Evolution of Physical Oceanography*, pages 264–291.

[Munk and Wunsch, 1998] Munk, W. and Wunsch, C. (1998). Abyssal recipes ii: Energetics of tidal and wind mixing. *Deep Sea Research Part I: Oceanographic Research Papers*, 45(12):1977–2010.

[Nguyen et al., 2017] Nguyen, A. T., Ocaña, V., Garg, V., Heimbach, P., Toole, J. M., Krishfield, R. A., Lee, C. M., and Rainville, L. (2017). On the benefit of current and future alps data for improving arctic coupled ocean-sea ice state estimation. *Oceanography*, 30(2):69–73.

[Ostashev and Wilson, 2015] Ostashev, V. E. and Wilson, D. K. (2015). *Acoustics in moving inhomogeneous media*. CRC Press.

[Overland, 2009] Overland, J. E. (2009). Meteorology of the Beaufort sea. *Journal of Geophysical Research: Oceans*, 114(C1).

[Perovich et al., 2021] Perovich, D., Smith, M., Light, B., and Webster, M. (2021). Meltwater sources and sinks for multiyear arctic sea ice in summer. *The Cryosphere*, 15(9):4517–4525.

[Pollard and Millard Jr, 1970] Pollard, R. T. and Millard Jr, R. (1970). Comparison between observed and simulated wind-generated inertial oscillations. In *Deep Sea Research and Oceanographic Abstracts*, volume 17, pages 813–821. Elsevier.

[Preisig and Duda, 1997] Preisig, J. C. and Duda, T. F. (1997). Coupled acoustic mode propagation through continental-shelf internal solitary waves. *IEEE journal of oceanic engineering*, 22(2):256–269.

[Rainville et al., 2011] Rainville, L., Lee, C. M., and Woodgate, R. A. (2011). Impact of wind-driven mixing in the Arctic Ocean. *Oceanography*, 24(3):136–145.

[Rainville and Woodgate, 2009] Rainville, L. and Woodgate, R. A. (2009). Observations of internal wave generation in the seasonally ice-free Arctic. *Geophysical Research Letters*, 36(23).

[Rigby, 1976] Rigby, F. A. (1976). *Pressure ridge generated internal wave wakes at the base of the mixed layer in the Arctic Ocean*. PhD thesis, University of Washington.

[Sagen et al., 2020] Sagen, H., Storheim, E., Geyer, F., Worcester, P. F., Beszczynska-Möller, A., Sandven, S., Kjøl, A., and Hughes, N. (2020). Caatex expedition to the north pole. In *Ocean Sciences Meeting 2020*. Agu.

[Sakurai and Commins, 1995] Sakurai, J. J. and Commins, E. D. (1995). Modern quantum mechanics, revised edition.

[Serreze and Meier, 2019] Serreze, M. C. and Meier, W. N. (2019). The arctic's sea ice cover: trends, variability, predictability, and comparisons to the antarctic. *Annals of the New York Academy of Sciences*, 1436(1):36–53.

[Simon et al., 2018] Simon, B., Isakson, M., and Ballard, M. (2018). Modeling acoustic wave propagation and reverberation in an ice covered environment using finite element analysis. In *Proceedings of Meetings on Acoustics 175ASA*, volume 33, page 070002. Acoustical Society of America.

[Smith and Sandwell, 1997] Smith, W. H. and Sandwell, D. T. (1997). Global sea floor topography from satellite altimetry and ship depth soundings. *Science*, 277(5334):1956–1962.

[Smith and Sandwell, 2019] Smith, W. H. and Sandwell, D. T. (2014 (accessed December 7, 2019)). Global Topography. `https://topex.ucsd.edu/WWW_html/mar_topo.html`.

[Spall et al., 2018] Spall, M. A., Pickart, R. S., Li, M., Itoh, M., Lin, P., Kikuchi, T., and Qi, Y. (2018). Transport of pacific water into the canada basin and the formation of the chukchi slope current. *Journal of Geophysical Research: Oceans*, 123(10):7453–7471.

[Stanton et al., 1986] Stanton, T., Jezek, K., and Gow, A. (1986). Acoustical reflection and scattering from the underside of laboratory grown sea ice: Measurements and predictions. *The Journal of the Acoustical Society of America*, 80(5):1486–1494.

[Stephenson et al., 2018] Stephenson, S. R., Wang, W., Zender, C. S., Wang, H., Davis, S. J., and Rasch, P. J. (2018). Climatic responses to future trans-arctic shipping. *Geophysical research letters*, 45(18):9898–9908.

[Stroeve et al., 2014] Stroeve, J., Markus, T., Boisvert, L., Miller, J., and Barrett, A. (2014). Changes in Arctic melt season and implications for sea ice loss. *Geophysical Research Letters*, 41(4):1216–1225.

[Stroeve and Notz, 2018] Stroeve, J. and Notz, D. (2018). Changing state of arctic sea ice across all seasons. *Environmental Research Letters*, 13(10):103001.

[Stroeve et al., 2012] Stroeve, J. C., Kattsov, V., Barrett, A., Serreze, M., Pavlova, T., Holland, M., and Meier, W. N. (2012). Trends in Arctic sea ice extent from CMIP5, CMIP3 and observations. *Geophysical Research Letters*, 39(16).

[Strub-Klein and Sudom, 2012] Strub-Klein, L. and Sudom, D. (2012). A comprehensive analysis of the morphology of first-year sea ice ridges. *Cold Regions Science and Technology*, 82:94–109.

[Talley, 2011] Talley, L. D. (2011). *Descriptive physical oceanography: an introduction*. Academic press.

[Thorsos, 1984a] Thorsos, E. I. (1984a). Surface forward scattering and reflection. Technical report, WASHINGTON UNIV SEATTLE APPLIED PHYSICS LAB.

[Thorsos, 1984b] Thorsos, E. I. (1984b). Surface forward scattering and reflection. Technical report, Applied Physics Laboratory, University of Washington.

[Thorsos, 1988] Thorsos, E. I. (1988). The validity of the kirchhoff approximation for rough surface scattering using a gaussian roughness spectrum. *The Journal of the Acoustical Society of America*, 83(1):78–92.

[Thorsos, 1990a] Thorsos, E. I. (1990a). Acoustic scattering from a "Pierson-Moskowitz" sea surface. *J. Acoust. Soc. Am.*, 88(1):335–349.

[Thorsos, 1990b] Thorsos, E. I. (1990b). Acoustic scattering from a "pierson–moskowitz"sea surface. *The journal of the acoustical society of America*, 88(1):335–349.

[Timmermans and Jayne, 2016] Timmermans, M.-L. and Jayne, S. R. (2016). The arctic ocean spices up. *Journal of Physical Oceanography*, 46(4):1277–1284.

[Timmermans et al., 2017] Timmermans, M.-L., Marshall, J., Proshutinsky, A., and Scott, J. (2017). Seasonally derived components of the canada basin halocline. *Geophysical Research Letters*, 44(10):5008–5015.

[Timmermans et al., 2014] Timmermans, M.-L., Proshutinsky, A., Golubeva, E., Jackson, J., Krishfield, R., McCall, M., Platov, G., Toole, J., Williams, W., Kikuchi, T., et al. (2014). Mechanisms of pacific summer water variability in the arctic's central canada basin. *Journal of Geophysical Research: Oceans*, 119(11):7523–7548.

[Timmermans et al., 2018] Timmermans, M.-L., Toole, J., and Krishfield, R. (2018). Warming of the interior arctic ocean linked to sea ice losses at the basin margins. *Science advances*, 4(8):eaat6773.

[Wadhams, 2012] Wadhams, P. (2012). Arctic ice cover, ice thickness and tipping points. *Ambio*, 41(1):23–33.

[Wadhams and Doble, 2008] Wadhams, P. and Doble, M. (2008). Digital terrain mapping of the underside of sea ice from a small auv. *Geophysical Research Letters*, 35(1).

[Wen et al., 1991] Wen, T., Garrison, G., Francois, R., Stein, R., and Felton, W. (1991). Sound speed, reflectivity, and absorption measurements in arctic ice in 1988. Technical report, WASHINGTON UNIV SEATTLE APPLIED PHYSICS LAB.

[Williams et al., 1992] Williams, K., Garrison, G., and Mourad, P. (1992). Experimental examination of growing and newly submerged sea ice including acoustic probing of the skeletal layer. *The Journal of the Acoustical Society of America*, 92(4):2075–2092.

[Worcester et al., 1999] Worcester, P. F., Cornuelle, B. D., Dzieciuch, M. A., Munk, W. H., Howe, B. M., Mercer, J. A., Spindel, R. C., Colosi, J. A., Metzger, K., Birdsall, T. G., et al. (1999). A test of basin-scale acoustic thermometry using a large-aperture vertical array at 3250-km range in the eastern North Pacific Ocean. *The Journal of the Acoustical Society of America*, 105(6):3185–3201.

[Worcester et al., 2018] Worcester, P. F., Dzieciuch, M. A., Colosi, J. A., Proshutinsky, A. Y., Krishfield, R. A., Nash, J. D., and Kemp, J. N. (2018). The 2016–2017 deep-water canada basin acoustic propagation experiment (canape): An overview. *The Journal of the Acoustical Society of America*, 144(3):1665–1665.

[Worcester et al., 2020] Worcester, P. F., Dzieciuch, M. A., and Sagen, H. (2020). Ocean acoustics in the rapidly changing arctic. *Acoust. Today*, 16(1):55–64.

[Yang and McDaniel, 1991] Yang, C. and McDaniel, S. (1991). Fourth moments of acoustic waves forward scattered by a rough ocean surface. *Waves in random media*, 1(4):419–439.

[Yang et al., 1992] Yang, C. C., Fennemore, G. C., and McDaniel, S. T. (1992). Scintillation index of the acoustic field forward scattered by a rough surface for two- and three-dimensional scattering geometries. *The Journal of the Acoustical Society of America*, 91(4):1960–1966.

[Yang and McDaniel, 1991] Yang, C. C. and McDaniel, S. T. (1991). Fourth moments of acoustic waves forward scattered by a rough ocean surface. *Waves in Random Media*, 1(4):419–439.

[Yang, 2014] Yang, T. (2014). Acoustic mode coupling induced by nonlinear internal waves: Evaluation of the mode coupling matrices and applications. *The journal of the acoustical society of America*, 135(2):610–625.

[Yang and Giellis, 1994] Yang, T. and Giellis, G. (1994). Experimental characterization of elastic waves in a floating ice sheet. *The Journal of the Acoustical Society of America*, 96(5):2993–3009.

[Yew and Weng, 1987] Yew, C. H. and Weng, X. (1987). A study of reflection and refraction of waves at the interface of water and porous sea ice. *The Journal of the Acoustical Society of America*, 82(1):342–353.

[Zhao et al., 2014] Zhao, M., Timmermans, M.-L., Cole, S., Krishfield, R., Proshutinsky, A., and Toole, J. (2014). Characterizing the eddy field in the Arctic Ocean halocline. *Journal of Geophysical Research: Oceans*, 119(12):8800–8817.

[Zinicola-Lapin, 2020] Zinicola-Lapin, W. N. (2020). *A deterministic approach to understanding the sensitivity of surface duct propagation to sound speed features in the upper ocean*. PhD thesis, Monterey, CA; Naval Postgraduate School.